The Dissertation Committee for Mary Grimes Van Baalen Certifies that this is the approved version of the following dissertation:

Simulating Space Radiation for Testing Shielding Material Effectiveness

Committee:

Sheryl L Bishop, Ph.D. Supervisor

Marco Durante, Ph.D.

Honglu Wu, Ph.D.

Michael Cornforth, Ph.D.

Steve Morrill, Ph.D.

Dean, Graduate School

Simulating Space Radiation for Testing Shielding Material Effectiveness

by

Mary Grimes Van Baalen, B.S., M.S.

Dissertation

Presented to the Faculty of the Graduate School of

The University of Texas Medical Branch

in Partial Fulfillment

of the Requirements

for the Degree of

Doctor of Philosophy

The University of Texas Medical Branch

August, 2014

Dedication

To my husband, Aaron Van Baalen, who believed I would finish even when I did not.

Acknowledgements

Throughout the process of this portion of my graduate career, I have often said that I have been on the century plan; that at some time this century I would get the degree. This dissertation represents the culmination of many years of graduate work and much patience by many who have supported me. First, I owe a great deal of gratitude to my Committee members Dr. Sheryl Bishop, Dr. Marco Durante, Dr. Honglu Wu, Dr. Michael Cornforth, and Dr. Stephen Morrill for serving on my committee for these many years. I am extremely grateful to Marco Durante for his help and guidance with this research effort. He included me in an interesting research project, afforded me the opportunity to take accelerator measurements data at the NASA Space Radiation Research Laboratory at Brookhaven National Laboratory, and provided guidance throughout this work.

I owe my parents, Richard and Deanna Grimes, immensely for raising me in an environment where education and continued learning were the norm. My siblings and I were very fortunate to have been regularly challenged with new ideas, knowledge, and experiences. My mother describes me as a busy child who always had much to do. A trait I still have today.

I have no doubt that a large part of my success is a direct result of several teachers recognizing my potential and need to be academically challenged. My fourth grade teacher, Mrs. Norman, regularly gave me extra work and reading material to keep me interested. Sister Leticia, my freshman year math teacher at St. Agnes Academy High School, encouraged me to join the accelerated math program encouraging me to pursue math. The calculus class I took my senior year in high school was so advanced that it was not until my third engineering calculus class at Texas A&M when I learned new material. Finally at Texas A&M, Dr. Gerald Schlapper and Dr. John Poston provided me the opportunity in my Master's program to use early radiation transport codes initiating the computational portion of my career.

I am grateful to several other radiation experts that I have interacted with over the course of this work. Many of the parameters necessary for PHITS input fields are difficult to select. Dr. Tatsuhiko Sato, Dr. Lembit Sihver, Dr. Stephen Guetersloh, and Dr. Amir Bahadori answered numerous questions on PHITS which helped me develop appropriate input files. Mr. Mark Langford, the administrator of the NASA Space Radiation Analysis Group Cluster, was always available to answer questions and provided invaluable help when the cluster went down and my files were lost. I also thank Dr. Adam Rusk and Dr. Michael Sivertz at Brookhaven National Laboratory for their help in taking the measurements and answering many questions over the years.

Finally, I especially thank my husband and daughters for their support during this long process. They put up with me spending time away from them in order to work on this degree. They believed that I would finish this, even when I did not.

Simulating Space Radiation for Testing Shielding Material Effectiveness

Publication No.______________

Mary Grimes Van Baalen, Ph.D.
The University of Texas Medical Branch, 2014

Supervisor: Sheryl L. Bishop

Abstract: The space radiation environment poses health risks to astronauts. There are three sources of space radiation: trapped radiation, Solar Particle Events, and Galactic Cosmic Rays (GCR) and these sources consist primarily of protons and heavier (HZE) ions. NASA has developed a radiation protection strategy to limit risks that includes the use of countermeasures such as shielding. A correct risk assessment relies on an accurate evaluation of the shielding effects of spacecraft structures on the incoming space radiation environment. Since the complicated shielding geometry plays an important role, existing transport codes must be improved to predict dose deposition inside the vehicle. Computer simulations of spacecraft are often used to show the reduction in equivalent dose provided by spacecraft structures. However, published research has shown that increasing shielding does not always result in a reduction in equivalent dose. When interacting with spacecraft structure and shielding materials, high energy protons and HZE ions can produce secondary particles that can cause greater biological damage than the incident particle. Shielding optimization, therefore, requires an understanding of the contribution of the physical interactions to the dose and dose equivalent.

Through the use of accelerator measurements and Monte Carlo simulations, the shielding properties were investigated for current and proposed spacecraft hull materials irradiated with protons and ^{56}Fe ions at 1 GeV/n. Small differences were seen between materials; however, these differences could be important when performing the design trades necessary for long duration space mission planning. This improved understanding can be incorporated into the radiation protection in future spacecraft designs.

TABLE OF CONTENTS

List of Tables

List of Figures

List of Abbreviations

2D	Two dimension
3D	Three dimension
A	Ion mass number
ALARA	As Low As Reasonably Achievable
BEAM	Bigelow Expandable Activity Module
BNC	Bayonet Neill–Concelman
BNL	Brookhaven National Laboratory
BFO	Blood Forming Organ
BRYNTRN	BaRYoN TRaNsport code
CNS	Central Nervous System
CPD	Crew Personal Dosimeter
CRÈME-96	Cosmic Ray Effects on Micro-Electronics code
CRRES/SPACERAD	Combined Release Radiation Effects Satellite/Space Radiation Effects
CHIME	CRRES/SPACERAD Heavy Ion Model of the Environment
D_T	Organ absorbed dose
ENDF	Evaluated Nuclear Data File
ESA	European Space Agency
ERR	Excess Relative Risk
FLUKA	FLUctuating KAskades
CG	Combinatorial Geometry

GCR	Galactic Cosmic Rays
GERMCode	GCR Event-based Risk Model
GG	Generalized Geometry
HETC-HEDS	High Energy Transport Code for Human Exploration and Development in Space
H_T	Organ dose equivalent
HZE	High charge and energy
HZETRN HZE	HZE TRaNsport code
IAEA	International Atomic Energy Agency
ICRP	International Committee on Radiological Protection
ICRU	International Commission on Radiation Units and Measurements
ISS	International Space Station
ISECG	International Space Exploration Coordination Group
JAERI	Japan Atomic Energy Research Institute
JAM	Jet AA Microscopic transport model
JSC	Johnson Space Center
JENDL	Japanese Evaluated Nuclear Data Libraries
JQMD	JAERI Quantum Molecular Dynamics model
KEK	High Energy Accelerator Research Organization
LBL	Lawrence Berkley Laboratory
LANL	Los Alamos National Laboratory
LEO	Low-Earth Orbit

LET	Linear Energy Transfer
LNT	Linear No Threshold
MCNP	Monte Carlo N-Particle
MCNPX	Monte Carlo N-Particle eXtended
MCNPX_HI	Monte Carlo N-Particle eXtended Heavy Ion
MHV	Miniature High Voltage
MLI	Multilayer Insulation
NAS	National Academy of Sciences
NASA	National Aeronautics and Space Administration
NCRP	National Council on Radiation Protection
NRC	National Research Council
NSRL	NASA's Space Research Laboratory
NUCFRG2	NUClear FRaGmentation model version 2
OSHA	Occupational Safety and Health Administration
PEANUT	Pre-Equilibrium Approach to Nuclear Thermalization
PHITS	Particle and Heavy Ion Transport code System
PMMA	Polymethyl methacrylate
Q	Quality factor
QMSFRG	Quantum Multiple Scattering Fragmentation Model
RBE	Relative Biological Effectiveness
RD	Relative Difference
REIC	Risk of Exposure Induced Cancer

REID	Risk of Exposure Induced Death
REMSIM	Radiation Exposure and Mission Strategies for Interplanetary Manned Missions
RIDM	Risk Informed Decision Making
RIST	Research Organization for Information Science and Technology
RHO	Radiation Health Officer
RSICC	Radiation Safety Information Computational Center
SAA	South Atlantic Anomaly
SPE	Solar Particle Event
SRAG	Space Radiation Analysis Group
STS	Space Transportation System
TEPC	Tissue-Equivalent Proportional Counter
TLD	Thermoluminescent dosimeter
TP	Technical Paper
UNSCEAR	United Nations Scientific Committee on the Effects of Atomic Radiation
US	United States
UTMB	University of Texas Medical Branch at Galveston
Z	Atomic number, also ion charge number

Chapter 1: Introduction

Space travel is a risky endeavor. This was clearly evident in the three major US spacecraft accidents; the Apollo 1 fire on the launch pad during a test, the disintegration of the Space Shuttle Challenger during launch, and the breakup of the Space Shuttle Columbia upon re-entering the Earth's atmosphere. Risks in human spaceflight are not limited to vehicle accidents, but include risks to the human participants that manifest in health consequences during and after a mission (Barratt & Pool 2008; Cucinotta et al. 2013; Cucinotta et al. 2011). These human health risks include loss of bone density and impaired bone remodeling leading to structural weakness (Orwoll et al. 2013; LeBlanc et al. 2000) cardiovascular changes such as fluid shifts, changes in total blood volume, heartbeat and heart rhythm irregularities, diminished aerobic capacity, (Meck 2001; Perhonen 2001) altered immune function (Barratt & Pool, 2008; Crucian et al. 2008; Crucian et al. 2013;), and vision degradation with evidence of increased intracranial pressure (Kramer et al. 2012; Mader et al. 2011). A space vehicle is also a closed-loop living environment providing the opportunity for microbiological and toxicological exposures from air, surface and water contaminants (Barratt & Pool 2008; Law et al. 2014). While the risk of visual impairment and intracranial pressure is an emerging risk, many other recognized human risks are reasonably well understood and there are generally countermeasures available or identified for future implementation.

Some of the least understood risks are those resulting from exposure to the space radiation environment. This is due to the fundamental differences in biological effects from the space radiation environment, and the difficulty in characterizing the consequences of space radiation exposures through direct observation of the exposed individual(Cucinotta et al. 2013). The radiation environment in space is complex; it includes unique high energy and high- linear energy transfer (LET) components that are distinct from the low energy and low-LET radiation environments generally encountered in terrestrial environments. Briefly, the space radiation environment consists of high-energy protons and high-charge (Z) and -energy (E) nuclei (HZE). A more detailed description of the space radiation environment is contained in Chapter 2. Due to the complexity of the space radiation field, both acute and late effects are possible in exposed astronauts. Acute radiation sickness, particularly the prodromal syndrome (i.e. nausea, vomiting, anorexia, and fatigue), could result from an intense solar particle event (SPE) during times when astronauts are not protected by adequate shielding. Late effects such as cancer and degenerative diseases, often thought to be related to aging, are being associated with the chronic exposure to space radiation.

EVOLUTION OF SPACEFLIGHT EXPOSURE STANDARDS

Through its authorization stated in the National Aeronautics and Space Act, NASA is responsible for developing its own standards to protect astronaut health. The Agency has relied on recommendations from external scientific review panels as its radiation protection philosophy has evolved. In 1967, the National Academy of Sciences-National Research Council (NAS-NRC) noted that radiation protection in human spaceflight is distinct from that in terrestrial workers because of the high-risk nature of spaceflight. Initially the evaluation of the radiation hazards from spaceflight focused on deterministic effects and malignant diseases were considered as "secondary" in importance (NRC 1967). In 1970 the NAS-NRC recommended dose limits for the Apollo astronauts as a guideline on the dose equivalent to the blood forming organ (BFO), thought to result in a doubling of mortality due to cancer for a white male between ages 35 and 55. The guideline was presented in terms of a "primary reference risk" and was designed "to limit the exposure to that which corresponds to an added probability of radiation-induced cancer over a period of about 20 years that is equal to the natural probability for the specific population at risk" instead of a defined limit. They estimated this exposure to be 400 rem and believed it corresponded to about a 2-3 percent risk of developing cancer. It is important to note that the risk of cancer resulting from space radiation was not to preclude the successful completion a particular mission and they noted that acceptance of a higher risk for planetary missions than for space station missions "would seem both realistic and practical" (Cucinotta 2007; NRC 1970).

In addition to recommending short-term limits to minimize acute effects, the National Council on Radiation Protection and Measurements (NCRP) in its Report 98, Guidance on Radiation Received in Space Activities (NCRP 1989) noted that cancer was the principal risk, and career limits were set to limit the risk of fatal cancer. The report limited the risk to 3 percent excess lifetime cancer mortality, based on comparison with other hazardous occupations. The report was also the first instance where NASA's radiation limits would take age and gender into account. In NCRP Report 132, Radiation Protection Guidance for Activities in Low-Earth Orbit (NCRP 2000), the NCRP questioned the use of mortality data from hazardous occupations as the basis for space-related radiation limits as there had been large reductions in workplace mortality in the intervening years since the publication of NCRP Report 98. In order to remain consistent with the guidelines for terrestrial radiation workers, the NCRP continued to endorse the 3 percent lifetime risk of cancer death. The report also briefly addressed the challenge of uncertainties in quantifying radiation limits: "It is well known that risk estimation is a difficult field in which there are many sources of potential error and therefore uncertainty. Given the magnitude of these uncertainties and the problems of dose specification estimates or risk on which dose limits for astronauts are based should be recognized as very conservative and possibly subject to modified values when more precise information becomes available" (NCRP 2000).

The knowledge of space radiation risks has matured since the 1960s; the data from the Japanese atomic bomb survivor cohort has evolved and new exposed cohorts, like the Mayak workers in Russia, have emerged. It is well known that within the human system radiation is a carcinogen, can cause degenerative diseases like cataracts, and, in large enough doses, can ablate cell populations. In addition, many animal and cell experiments have been performed using particle types and energies relevant to the space radiation environment providing strong evidence that the biological effects from HZE particles are fundamentally different from low LET radiations common in terrestrial radiation protection (Ritter & Durante 2010). Further, there are also strong indications that radiation exposure also has deleterious effects on the central nervous system (CNS) and the cardiovascular system (Huff & Cucinotta 2009a; Huff & Cucinotta 2009b; NCRP 2006). A robust radiation protection program has evolved at NASA to address the growth in knowledge of the biological effects of radiation, the increase in number of individuals who have flown in space, the inclusion of females in the astronaut population, the continued human presence in low earth orbit (LEO) through the International Space Station (ISS), and the extension of mission durations to as long as a year. To control the amount of risk resulting from radiation incurred by the larger more diverse astronaut population, radiation limits have evolved to a Space Permissible Exposure Limit for Space Flight Radiation that limits planned career exposure to 3% risk of exposure induced-death (REID) for fatal cancer (NASA 2007). The basis for the limit is the solid cancer mortality analysis from the Life Span Study (LSS) Report 13 (of the Japanese atomic bomb survivors). This analysis forms the basis for calculating age and gender specific effective doses to reach a probability of a 3% REID. In addition, NASA has been utilizing an administrative limit for managing the risk to an individual astronaut throughout his/her career. This administrative limit is set to to ensure that the astronaut does not exceed 3% REID at the upper 95% confidence level using a statistical assessment of the uncertainties in the risk projection calculations to limit the cumulative effective dose (in units of Sievert) received by an astronaut throughout his or her career.

For LEO exposures, the NASA administrative limit is approximately equal to a 1% REID point estimate (Cucinotta 2007; NASA 2007).

ALARA AND RADIATION DOSE LIMITATION

Approaches to protection against ionizing radiation are remarkably consistent throughout the world. This is due largely to the existence of a well-established and internationally recognized radiation protection framework. Central to this framework is the International Commission on Radiological Protection (ICRP). There are three primary requirements in the general system of radiological protection recommended by the ICRP (IAEA 2004; ICRP 1977; ICRP 2007):

1) Justification,

2) Optimization, and

3) Dose limitation.

Justification means that any proposed activity involving exposure to individuals should not be adopted unless it yields a sufficient benefit to the exposed individuals or to society in order to justify the risks incurred by the radiation exposure. The principle was introduced because of the need to find some way of balancing costs and benefits of the introduction of a source involving ionizing radiation. It is based on the hypothesis that any radiation exposure, no matter how small, carries with it a certain level of risk and that risk is proportional to the level of exposure. This hypothesis is known as the linear, non-threshold hypothesis (LNT). The second feature is optimization, which is technically the practice of the as low as reasonably achievable (ALARA) principle. ALARA requires that "all radiation should be kept as low as reasonably achievable, economic and social factors taken into account" (ICRP 1977; ICRP 1990; ICRP 2007). ALARA is a management tool to implement safety factors to keep exposures below regulatory dose limits using a cost benefit analysis approach. For NASA this means ALARA must be considered when designing vehicles, developing dose limits and planning missions. ALARA, is based on the LNT hypothesis and is also required by all international regulatory agencies and scientific bodies and as such becomes a legal requirement for NASA. The third element is dose limitation. This involves setting upper limits on the dose that may be received by any exposed individual (including members of the public) from all sources of radiation other than medical. These limits are then imposed by regulatory agencies.

In addition, ICRP recommends that each source of exposure, such as a hospital or reactor site, be constrained to a fraction of the dose limit. As a simple example, with the dose limit of 100 mrem/yr for members of the public, then the constraint might be set at 30 mrem/yr. This may be viewed as that site's share of the allotted exposure of 100 mrem/yr to any member of the public. The ICRP recognizes that some individuals may receive radiation doses from several facilities independently. Each site will then optimize the doses received to be as far below 30 mrem/yr as possible, in order to ensure that the doses are ALARA. In this system of dose limitation, optimization plays the central role, and dose limits play a very secondary role, mainly as guidance for setting action levels and other operating parameters, and also as a guide for allocating dose to various sources, that is, as a guide in setting constraints (ICRP 1977; ICRP 1990).

The major factors that assist in limiting the exposure (and thus risk) from a single 6-month ISS mission are the geomagnetic shielding provided by the Earth and the length of the mission. The radiation risk from a single 6-month ISS mission does not exceed 1% REID, regardless of age and gender, therefore, altering the length of an ISS mission is not necessary to maintain exposures ALARA. Instead, crew assignments to ISS Expeditions are used to manage the REID over the career of an astronaut. There will be continued challenges in meeting this limit as mission lengths extend beyond one year. To further keep exposures ALARA, NASA incorporates radiation protection into its design of space vehicles and management of missions. Two of the basic tenets of terrestrial radiation protection, time and shielding, are used to limit radiation exposure in space. Practical actions taken by NASA include performing design analyses of the radiation protection properties of new spacecraft (Simon, et al. 2013; Wilson et al. 2001), lining the crew quarters of the ISS with polyethylene to reduce primary and secondary proton and neutron exposures (NASA 2006; Shavers et al. 2004), and timing the extravehicular activities spacewalks to avoid high latitude passes and the South Atlantic Anomaly (NCRP 2002; NCRP 2000). However, the costs of incorporating time and shielding must be commensurate with other mission risks (e.g. launch hazards, failures of life support systems, human error, etc.), technical risks (e.g. launch mass restrictions), as well as cost and schedule risks. Meeting the exploration technical and safety goals while meeting programmatic constraints related to cost and schedule involves making complex decisions. Within its Risk Informed Decision Making (RIDM) process, NASA has developed an iterative framework for evaluating engineering design options (Dezfuli et al. 2010). The iterative design process shown in Figure 1.1 is a multidisciplinary activity that requires robust computational procedures for evaluating astronaut REID for a given design reference mission while performing the appropriate trades studies. The process must evaluate construction methods for the vehicle design in terms of mission objectives and costs as part of the approval of the design. The process will then determine whether the design is ALARA. The need to understand and manage the risk of radiation exposure within this decision making framework has led NASA to develop a large research effort to decrease the uncertainties associated with evaluating and projecting risks from space radiation.

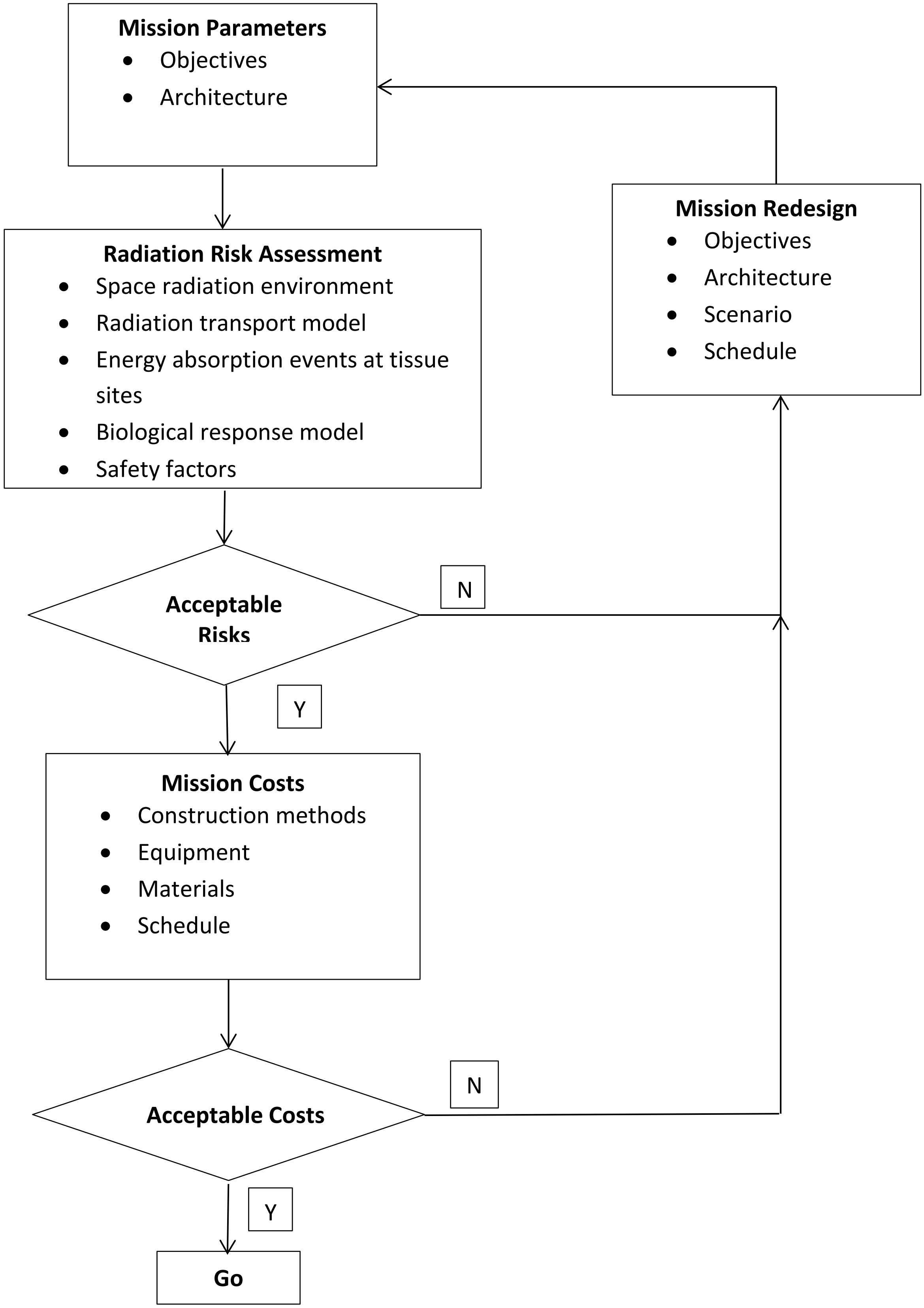

Figure 1.1: Iterative radiation design process. Adapted from Wilson et. al 1997.

The characterization and reduction of uncertainty in space radiation risk estimates is necessary for improving the precision of these estimates and reducing the relatively large confidence intervals dominated by the uncertainties in biological response to space radiations. Much of the research focus has been on reducing the uncertainty of human biological response from high charge and energy (HZE) radiation through ground-based experimentation (Cucinotta et al. 2002; Durante & Cucinotta 2011; Cucinotta et al. 2012). Unfortunately, the biological research necessary to reduce the uncertainties will require many years to complete. With design and planning for exploration missions already underway (ISECG 2013; NASA 2014), decisions on reference missions and vehicle design will be required without the benefit of the full scientific understanding of the biological uncertainties. Improvements in the methods and understanding in the areas of the radiation protection qualities of spacecraft materials is warranted to provide a sound basis for the design trades that are necessary in space vehicle design and mission planning. The need to inform NASA decisions on spacecraft materials, mass constraints, and mission lengths within the currently available scientific knowledge was the motivation behind this work.

A correct risk assessment relies on an accurate evaluation of the effect of vehicle structures on the incoming space radiation environment. Since a complicated shielding geometry plays an important role, existing transport codes must be improved to predict dose deposition inside the vehicle. Experimental work is therefore indispensable in the validation of these codes. These determinations can be used in making shielding optimization recommendations and inform mission planning. Previous accelerator experiments to evaluate the effectiveness of spacecraft materials at reducing dose have focused on single materials and not layered mock-ups more closely representing a spacecraft wall (Gutersloh et al. 2006; Miller et al. 2003; Zeitlin et al. 2006; Zeitlin et al. 2008). Within this research project, the following four materials combinations were further investigated to improve the understanding of the interactions of ^{56}Fe ion and protons (Lobascio et al. 2008; Silvestri et al. 2011). The Particle Heavy Ion Transport (PHITS) code, a relatively new Monte Carlo transport tool, was utilized in the investigations.

1. The Columbus Science Module launched in February 2008. Its design and structure is similar to the other ISS modules and Orion Service Module which is being built by the European Space Agency. Understanding its radiation protection properties will be valuable for NASA and this knowledge can be translated to the development of new space vehicles. This dissertation focusses on the dose reduction capability of a more realistic mock-up of the vehicle structures when compared to single materials, aluminum or polyethylene of equivalent areal density.

2. An improved understanding of the radiation protection properties of inflatable spacecraft structures is important as space agencies look for low mass vehicle materials for interplanetary missions. Therefore, computer simulations of 1 GeV proton and 1 GeV/n ^{56}Fe beams interacting with one proposed inflatable structure, REMSIM, was compared with standard spacecraft materials, aluminum and polyethylene of similar areal density.

3. This dissertation will investigate the differences in equivalent dose caused by changing the order of materials used in shielding design. The current effort investigates the differences in the production of secondary particles from 1 GeV/n ^{56}Fe and 1 GeV proton beams incident on aluminum followed by polyethylene and polyethylene followed by aluminum.

4. Previous experiments concentrated on measurements along the beam axis (Bertucci et al. 2007; Mancusi et al. 2007; Lobascio et al. 2008; Silvestri et al. 2011). This current effort focusses on the measurement of the angular distribution of protons produced by high energy protons irradiating 20 g/cm^2 thick aluminum shielding.

Chapter 2: Background and Literature Review

Quantities Used in Radiation Protection

The risks associated with exposure to radiation cannot be measured directly; they are calculated from measured radiation exposure, radiation properties, and combined with computer model predictions of risk. The system of dose quantities has been defined by ICRP and International Commission on Radiation Units and Measurements (ICRU) for terrestrial external radiation protection provides the basis of space radiation protection (ICRP 2007; ICRU 1993; NCRP 1991).

Radiation exposures are described in terms of the absorbed dose, D, which is the energy absorbed per unit mass of a material. Formally, absorbed dose at a point is defined by the ICRU as:

$$D = \frac{\Delta E}{\Delta m} \qquad \text{Eqn 2.1}$$

Where ΔE is the mean energy absorbed from the radiation to a mass, Δm. The SI unit of absorbed dose is J kg^{-1} and its special unit is known as the gray (Gy). Absorbed dose takes into account of the radiation field internal and external to the specified volume of mass and therefore, all charged particles that were produced in or enter that volume. In radiation protection the interest is in the absorbed dose averaged over a tissue or organ volume. The mean absorbed dose, $D_{T,R}$, in and organ or tissue T due to radiation of type R is the basic quantity for the definition of the protection quantities equivalent dose and effective dose. In mixed radiation fields the mean absorbed dose, D_T in and organ or tissue T is given by (Attix 1986):

$$D_T = \sum_R D_{T,R} \qquad \text{Eqn. 2.2}$$

It is common to describe the number of particles incident on a cross-sectional area, or incident on a sphere of a given cross-sectional area, called the fluence, F, with units cm^{-1}. As particles pass through matter, they lose energy at a rate dependent on their kinetic energy, E and charge number, Z, and approximately the average ratio of charge to mass (Z_T/A_T) of the materials through which they travel. This rate of energy loss is called the Linear Energy Transfer (LET), which, for unit density materials such as tissue, has units of keV/μm. Dose and fluence are related by D = ρ F LET, where ρ is the density of the material (for water or tissue = 1 g/cm^3).

Most biological effects of radiation can be related to the absorbed dose. However, radiation protection is generally concerned with controlling exposures so that the detriment to the individual is limited. When experiments have been performed on biological systems using different radiation types, it has been shown that different absorbed doses are sometimes needed to obtain the same biological effect. This is particularly true for high LET radiation. The quantity that has been defined to account for these differences is the relative biological effectiveness (RBE), which is defined as the ratio of the absorbed dose of a standard radiation, such as X rays or gamma rays, to the absorbed dose of a radiation in question, that both produce the same level of a given biological effect. In the regulatory framework defined by the ICRP and the NCRP, an equivalent dose is obtained when the absorbed dose is weighted by a modifying factor that reflects the damaging ability of the particular type of radiation, or the 'effectiveness' of the radiation. These modifying factors are proscribed by recommendation bodies such as the ICRP or NCRP as a measure of cancer risk associated with different types of radiation exposure to individual organs (ICRP 60; ICRP 103; NCRP 1993). For individual tissues or organs, the modifying factor is known as a radiation weighting factor, W_r, and varies depending upon the particle type and energy as shown in Table 1.1. The radiation weighting factor was previously known as the quality factor (ICRP 1977). The product of dose and the radiation weighting factor (D x W_r) is known as the Equivalent Dose (H) and is given in Sieverts (Sv) (1 rem = 0.01 Sv). In a similar fashion, the equivalent dose to a specific organ or tissue (t) due to a radiation (r) is the organ dose equivalent ($H_{t,r}$) and likewise carries units of Sv. However, for the complex mixtures of high- and low-LET radiations in space, the practice in the space radiation protection community is to average the point quantity $H_{t,r}$ over the organ or tissue of interest by means of computational models to obtain the organ dose equivalent.

Type and Energy Range	**Weighting Factor, w_r**
Photons, all energies	1.0
Electrons, positrons, and muons, all energies	1.0
Neutrons <10 keV	5.0
10 to 100 keV	10.0
>100 keV to 2 MeV	20.0
>2 MeV to 20 MeV	10.0
>20 MeV	5.0
Protons, other than recoil protons, energy >2MeV	2.0
Alpha particles, fission fragments, non-relativistic heavy ions	20.0

Table-2.1: Radiation Weighting Factors (adapted from ICRP 1991).

Radiation weighting factors are not used in space radiation protection since the spectrum in different organs is a complicated mixture of primary and secondary particles. The approach recommended by the NCRP is to use the organ dose equivalent H_T defined by the ICRU (ICRU 1993):

$$H_T = \frac{1}{m}\int_m dm \int Q(L)F_T(L)Ldl \qquad \text{Eqn. 2.3}$$

where *L* is the LET, *m* is the organ mass averaged over a tissue, F_T is the fluence of particles through the tissue *T*, and *Q* is the quality factor which is dimensionless. *Q* is a continuous function of LET and the ICRP recommendations are illustrated in Figure 2.1. The radiation quality is defined as a function of the LET of a heavy charged particle. Any particle having an LET below 10 keV/µm is given a quality of 1.0, the curve rises steeply thereafter to a maximum quality of 30 for particles with an LET of 100 keV/µm. The curve decreases for particles having an LET greater than 100 keV/µm based on measured RBE's and the theory that the excess energy deposited is not more effective at cell killing. (ICRP 1991) It is important to note that there is experimental evidence that biological effect of charged particles depends both on track structure and LET. However, the *Q(L)* relationship represents a reasonable first approximation of the changes in RBE in a mixed radiation field such as that in space and NASA continues to use *Q(L)* rather than ICRP radiation weighting factors based on NCRP recommendations (NCRP 2000).

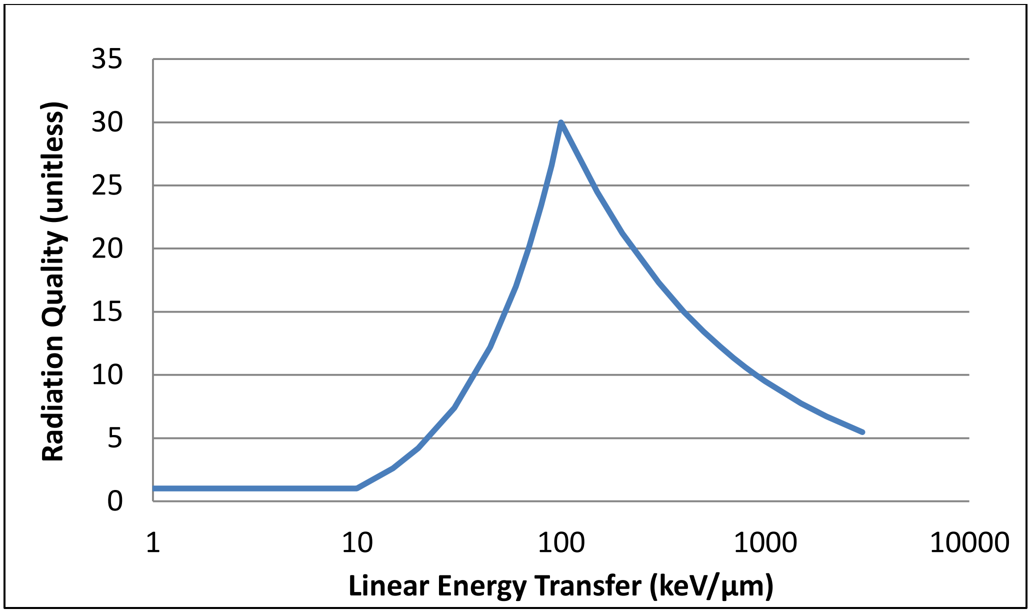

Figure 2.1 : Quality as a function of LET. Adapted from ICRP 1977.

Long term dose monitoring on board the Space Shuttle and International Space Station (ISS) with the Tissue Equivalent Proportional Counters have shown that total quality factors measured per mission vary from 2.0 to 3.1 with the Galactic Cosmic Rays (GCR) having quality factors ranging from 11-22 inside the vehicle (Beaujean et al. 1999; Zhou et al. 2009; Zhou et al. 2010) Recent measurements made by the Radiation Assessment Detector on the Mars Science Laboratory have shown the average quality factor for GCRs to be 3.82 ± 0.25 in free space while on the surface of Mars, the average quality factor was lower at 3.05 ± 0.26 (Hassler et al. 2014; Zeitlin et al. 2013)

Exposure of different organs or tissues can result in different risks to the individual. The quantity Effective Dose (E) reflects the same probability of the occurrence of effects regardless of whether the irradiation is a uniform or partial body irradiation. It also accounts for the varying sensitivities of the organs to radiation.

Effective dose is the sum of the weighted dose equivalent (H_T) for all exposed tissues or organs. The tissue weighting factor reflects the relative radiation detriment to each organ and tissue including the different mortality and morbidity risks from cancer, the risk of severe hereditary effects, and the years of life lost due to these effects (NCRP 2000).

$$E = \sum_T w_T H_T \qquad \text{Eqn: 2.4}$$

SPACE RADIATION ENVIRONMENT

The ionizing radiation environment in space is comprised of charged particles, uncharged particles, and high-energy photons with a broad range of energies. The particles vary in size from electrons and protons to heavy nuclei. In the near-Earth space environment, there are three naturally occurring sources of space radiation, solar particle events (SPE), galactic cosmic rays (GCR), and trapped radiation. For radiation protection purposes, GCRs are the most challenging to mitigate. In addition, the interaction of the cosmic rays with the spacecraft walls creates secondary particles, both electrically charged and neutrally charged. Radiation levels from each of these sources vary in intensity, temporally, and spatially. The temporal and spatial fluctuations must be taken into account in the planning of space missions to minimize the hazardous effects of radiation exposures.

Solar Particle Events (SPE)

Solar radiation can be divided into two groups: a steady stream of solar material called the solar wind, and Solar Particle Events (SPE) which are associated with solar flares and coronal mass ejections. Most solar radiations are of lower energy than the GCR, but coronal mass ejections release a very high fluence rate, on average 10^{12} particles per cm^2. The solar wind is composed of approximately 95% protons, 4% alpha particles, and about 1% other nuclei consisting primarily of carbon, nitrogen, oxygen, neon, magnesium, silicon and iron. These particles contain high (~800 km/s) and low (~400 km/s) speed components. In general, the low speed winds contain a factor of 3 higher numbers of heavier nuclei (Reames 1999). The solar wind particles, even when enhanced due to higher solar activities, do not contribute to the dose to astronauts due to the relative low energy of the particles and hence the absorption in even thin shielding thicknesses .(Cucinotta 2007; Durante & Cucinotta 2011).

The Sun's activity is characterized by an 11-year cycle that can be divided into four inactive years (solar minimum) and seven active years (solar maximum). Changes in electromagnetic radiation, particles, and magnetic fields arriving from the Sun have a significant influence on the space surrounding the Earth. SPEs occur when energetic charged particles are ejected from the sun into interplanetary space. The most energetic particles arrive at Earth within tens of minutes of the event on the Sun, while the lower-energy particles arrive over the course of a day. Without radiation protection, SPEs can result in significant doses to astronaut crews. Large SPEs occurred in November 1960, August 1972, and October 1989. Fortunately, these events did not occur when astronauts were on the surface of the moon. However, future events of these magnitudes could result in clinical detriment to astronaut crews.

Solar flares and Coronal Mass Ejections (CME) are eruptions from the sun's surface and are associated with sunspots. These events are much more likely to occur in the time of maximum solar activity, but occur with a much lower frequency than sunspots. SPEs associated with solar flares develop rapidly and can last for days. They produce intense electro-magnetic radiations as well as protons, electrons, and plasmas of helium to iron, of which approximately 97.8% is composed of protons and 2.1% is Helium (Hathaway 2012). SPEs are highly unpredictable in occurrence, intensity, and duration. This is due to the physics behind both the formation and transport of the particles. As a consequence, an intense SPE can arrive at earth and be complete within hours, or the SPE can last for more than a week, during which there are bursts of radiation lasting a few hours. A large number of the particles from an SPE are protons with energies less than 10 MeV/nucleon which can be relatively easily shielded by spacecraft hulls. There is a rapid fall off in intensity with increasing energies common to all CMEs. The very high density of protons with energies greater than 10 MeV can still be a particular source of concern for external operation, while protons of more than 30 MeV can be of concern to thinly shielded habitats.

Accurate prediction of the time and intensity of individual SPEs is not currently possible. Modern data on SPEs have only has been collected since 1956, which corresponds to the beginning of cycle 19. This data indicates that about 30 to 50 major SPE events occur per cycle, most during the middle 5 years corresponding to solar maximum. Of particular note are the occasional very large CMEs, which have the potential for effects on crew health. One such SPE, commonly known as the August

1972 event, is among the largest recorded events. Although this event is often used in radiation protection planning for possible future SPEs, it may not be the worst case scenario. Through the examination of nitrates in ice core samples, it has been determined that solar events of up to ten times the intensity of the 1972 event have occurred in the past 500 years. Another important consideration is that although the occurrence of SPEs is can be frequent during solar maximum, the occurrence of these intense SPEs is rare. There are several statistical models of SPE occurrences available for mission planning. These are: the King model (King 1974), the Jet Propulsion Laboratory (JPL) model (Feynman, et al. 1993), the Emission of Solar Protons (ESP) model (Xapsos et al. 1999), and the NASA SPE Propensity Model (Kim et al. 2009). SPEs that occur during a mission can be disruptive to accomplishing mission objectives; i.e. astronauts may need to relocate to a more heavily shielded area of the spacecraft, EVAs can be rescheduled, etc. (NASA 2014). Having the ability to accurately forecast the occurrence and severity of SPEs would minimize radiation hazard from radiation.

Galactic Cosmic Rays

Galactic Cosmic Radiation (GCR) originates outside our solar system but generally within the Milky Way Galaxy and is treated as isotropic or uniform in intensity and direction. This radiation consists of atomic nuclei of hydrogen to uranium which have been ionized and accelerated to very high energies. The highest-intensity GCR is found between a few tenths and a few tens of GeV per nucleon, where the particles can penetrate tens to hundreds of centimeters of shielding. GCR is 85 percent protons, 14 percent helium, and the remaining 1-2% heavier nuclei with charges ranging from 3 (lithium) to about 28 (nickel) (Simpson 1983). Ions heavier than nickel are also present, but they are rare. These subtle compositional differences were a key factor in understanding the origin of GCR and provided the original impetus for the development of heavy-ion transport codes and heavy-ion cross-section libraries that are used today. The remaining 1% of the GCR is composed of electrons and positrons.

These particles are termed HZE particles because they are composed of high-energy (high-E) nuclei of heavier (high atomic number Z) elements. The fluence levels of these particles are very low. However, since they travel very close to the speed of light, and because some of them are composed of very heavy elements such as iron, they produce intense ionization as they pass through matter. Consequently, although the number of HZE particles is relatively small, they can have a significant biological impact. Figure 2.2 shows the relative contribution of fluence of charged particles to the dose and dose equivalent. This graph was created using the NASA developed radiation transport code, HZETRN, and the Badhwar O'Neil GCR model (Cucinotta et al. 2003; Durante & Cucinotta 2011; Group 2012). The electrons and positrons present in GCR are a minor biological hazard as compared to the bulk of GCR since they are easily shielded.

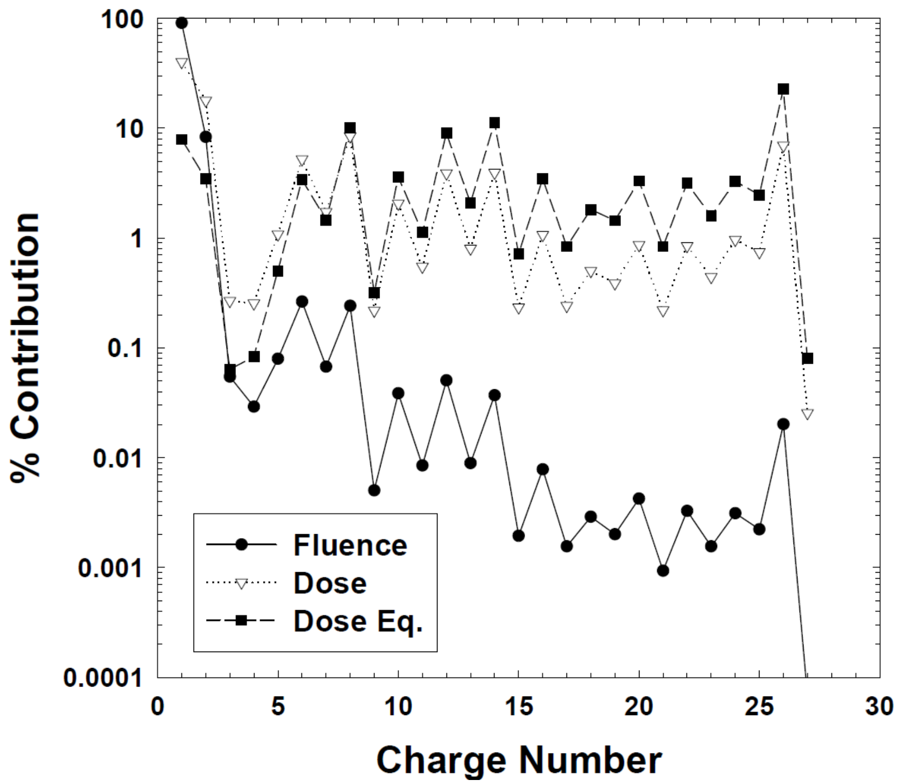

Figure 2.2: Percent contributions from individual GCR elements for the particle flux, dose, and dose equivalent at solar minimum. Reprinted from Cucinotta et al. 2003.

The galactic cosmic radiation also varies as a function of the level of solar activity which has follows the 11 year solar cycle. The number of solar particles is directly related to the number of observed solar events. When the solar wind increases there are more particles and higher interplanetary magnetic field to interact with the influx of GCR. This interaction removes some of the lower energy GCR particles. The result is that in time of solar maximum the GCR environment in the inner solar system has a higher energy but lower fluence than during solar minimum. Equivalent doses (H) from the GCR in interplanetary space are estimated to range from 0.3 Sv/year during solar maximum to about 1 Sv/year during solar minimum.

Interactions of the GCR with the solar wind, combined with the cyclic changes in magnetic fields of the sun, have the effect of modulating the GCR spectrum and this modulation is described by several different models. Examples used in the US are the Nymmick model (Nymmik 1996), the Combined Release Radiation Effects Satellite/Space Radiation Effects (CRRES/SPACERAD) heavy ion model (Chen et al. 1994), and the Badhwar-O'Neill model (Badhwar & O'Neill 1994; O'Neill 2010). Each of these models has its strengths and weaknesses and their use by the scientific and operational communities seeks to capitalize on its strengths. The Nymmick model is used in the 1997 version of Cosmic Ray Effects on Micro-Electronics code (CRÈME-96) developed by the Naval Research Laboratory and widely used for predicting single event effects for micro-electronics in aircraft and spacecraft (Tylka et al. 1997). The CRRES/SPACERAD Heavy Ion Model of the Environment (CHIME) was developed in collaboration with the US Air Force and also used for predicting effects on microelectronics in satellites in Air Force applications (Chenette et al. 1994). NASA uses the Badhwar-O'Neill model for human spaceflight mission planning and also on the prediction of single event effects on microelectronics in its spacecraft (Badhwar & O'Neill 1994; O'Neill 2010).

Trapped Radiation

Trapped radiation results when charged particles are trapped in the magnetic field surrounding the Earth. The rotation of the earth's molten iron core creates electric currents that produce a magnetic field which extends thousands of kilometers into space. As charged particles interact with this magnetic field, their original direction is altered according to their energy, charge, and mass along the magnetic field lines of the earth. These particles are contained in one of two doughnut-shaped magnetic rings surrounding the Earth called the Van Allen radiation belts. The inner belt contains a fairly stable population of protons with energies exceeding 10 MeV. While the outer belt contains mainly electrons with energies up to 10 MeV for which spacecraft hull and structures provide sufficient shielding. Protons with energies greater than 30 MeV have sufficient energy to penetrate spacecraft structures. Additionally, the trapped electrons have an insignificant contribution at altitudes lower than 700 km and do not pose a threat for astronauts. Other ions such as, helium, carbon and oxygen nuclei, have been detected in these trapped regions, but they are of much less concern than the protons due to their scarcity.

Charged particles trapped in the Earth's magnetic field have a helical motion around the geomagnetic field lines that consists of a sliding motion along the field lines and a bouncing motion along a line between the trapped particle's mirror points (Hess 1968). In addition to the helical motion, there is also a longitudinal drift around the Earth, with electrons drifting East and protons drifting West. The South Atlantic Anomaly (SAA) region, where the spiraling protons get closer to Earth than usual, is an important source of radiation exposure for crewmembers in a spacecraft traveling at low orbit inclination and low altitude (NCRP 1998; NASA 2012). During periods of solar minimum, for ISS and MIR usual orbital inclination of 51.6° and altitude of approximately 400 km, almost half of the ionizing radiation came from SAA trapped protons, while the other half came from GCR (Badhwar 1997).

Experience with Earth orbital missions to date indicates that nearly all of the accumulated radiation exposure can be attributable to passages through the SAA (Kim et al. 2007). In addition to altitude and orbital inclination, the integrated dose is a function of solar cycle. Increases in solar activity expand the atmosphere and increase the loss of trapped protons. Therefore, trapped radiation doses in LEO are known to decrease during solar maximum and increase during solar minimum. Although high inclination flights pass through the SAA maximum intensity regions, less time is spent in the SAA than low inclination flights. Crews in high inclination flights receive less net exposure to trapped radiation than in low inclination flights for a given altitude. Low inclination flights will not transit the SAA lower than 28.5 degrees south latitude and avoids the peak of the SAA.

For most of NASA's space programs, astronauts have not traveled through the Van Allen Belts; however, missions to deep space require traversing them (Kim et al. 2007). Thus, for a spacecraft in LEO, the main contribution from the trapped radiation to dose rate comes from the trapped protons. The trapped proton flux is influenced by both the solar activity and by altitude. At a fixed altitude the proton fluxes decrease as the solar activity increases, whereas at constant solar activity the trapped fluxes increase almost exponentially with altitude (Badhwar 1997). During travel to the Moon or Mars, a spacecraft will be accelerated in LEO and pass through the inner and outer radiation belts as it achieves escape velocity. Fortunately, during the manned Apollo missions, the craft transit in these regions was rapid enough that overall dose due to trapped protons was minimized. The average skin dose for those missions was 4.1 mGy, most of which was attributable to the radiation belts (Bailey 1976).

Nuclear Propulsion and Power

While the bulk of the discussion of the radiation environment has focused on the natural environment in space, manmade sources of radiation are used in spaceflight. Nuclear propulsion could reduce radiation exposure during long duration missions both by shortening transit times (Durante & Bruno 2010). NASA has historically funded programs to study the efficacy of using nuclear technology for propulsion and planetary surface based power systems (Aftergood 1989; DOE 1987). While a direct comparison of a nuclear system to chemical one is difficult, nuclear systems could provide a more efficient means of transport. The benefit of using nuclear technology for propulsion systems is in the ability to provide a greater specific impulse and more thrust per unit mass compared with conventional chemical propellant systems. Higher specific impulse is directly correlated with shorter transit times, currently estimated at 30% less compared to chemical propulsion. Nuclear propulsion would require less mass as chemical propellants would not be needed and the mass savings could be replaced with an augmentation in shielding. Whether time is shortened or shielding is added, radiation exposures would be reduced during transit.

The use of nuclear energy could dramatically change the capabilities of interplanetary missions. As radiation exposures are already of concern, limiting additional exposures from man-made sources will be critical to a nuclear program.

Exposures from man-made sources are not considered in this present study, however, future considerations in mission planning should also focus on shielding materials and designs, as well as, optimizing distance from the reactor.

PHYSICS OF ENERGY LOSS AND FRAGMENTATION OF HEAVY IONS

When high energy ions pass through matter they interact with constituent atoms, molecules and nuclei. There two basic types of interactions processes that occur: 1) ionization and excitation of the atoms and molecules of the material and 2) nuclear interactions with the nuclei of the atoms of the material (Attix 1986). Mathematically particle transport can be described by the time-independent Boltzmann equation using the continuous slowing down approximation (Wilson et.al. 1991; Wilson et.al. 2001):

$$\vec{\Omega} \cdot \vec{\nabla}\varphi_j(\vec{x},\vec{\Omega},E) - \frac{\partial}{\partial E}\left[S_j(E)\varphi_j(\vec{x},\vec{\Omega},E)\right] + \sigma_j(E)\varphi_j(\vec{x},\vec{\Omega},E) =$$

$$\int \sum_k \sigma_{jk}(\vec{\Omega},\vec{\Omega}',E,E')\varphi_k(\vec{x},\vec{\Omega}',E')d\vec{\Omega}',dE' \qquad \text{Eqn. 2.4}$$

where $\varphi_j(\vec{x},\vec{\Omega},E)$ is the flux of particle type *j* at the position $\vec{x}$ heading in the direction $\vec{\Omega}$ with energy *E*, $S_j(E)$ is the stopping power of particle type *j* with energy *E,* $\sigma_j(E)$ is the total cross section of particle type *j*, with energy *E,* and $\sigma_{jk}(\vec{\Omega},\vec{\Omega}',E,E')$ is the cross section for particles of type *k* with energy *E'* and direction $\vec{\Omega}'$ creating particles of type *j* with energy *E* and direction $\vec{\Omega}'$. There are different types of interactions that may occur as a result of each interaction and are described by the total probability of interaction or cross section $\sigma_j(E)$ which can be expanded to:

$$\sigma_j(E) = \sigma_j^{at}(E) + \sigma_j^{el}(E) + \sigma_j^{n}(E) \qquad \text{Eqn. 2.5}$$

where the first term refers to collision with atomic electrons, the second term is for elastic nuclear scattering, and the third term describes nuclear reactions. The approximate values for the cross sections and average energy transfer are as follows (NCRP 2006):

$$\sigma_j^{at}(E) \sim 10^{-16} cm^2\ for\ \delta E_{at} \sim 10^2 eV$$

$$\sigma_j^{el}(E) \sim 10^{-19} cm^2\ for\ \delta E_{el} \sim 10^6 eV$$

$$\sigma_j^{r}(E) \sim 10^{-24} cm^2\ for\ \delta E_{at} \sim 10^8 eV$$

From the cross section information above, the primary interactions of charged particles with matter are atomic interactions, through ionization and excitation. Many atomic collisions (~10^6) occur in an cm of matter, whereas approximately 10^3 nuclear Coulomb elastic collisions occur per cm. In contrast, nuclear reactions are separated by a fraction to many cm depending energy and particle type.

As a charged particle travels through matter it loses kinetic energy by either exciting bound electrons of the atoms making up the matter, or by ionization the stripping of the electron entirely from the atom. Typically the amount of energy required to excite electrons in an atom is very small compared to the energy required to ionize an atom; therefore most of the energy loss that occurs is from ionization and the energy loss from excitation can be neglected. The ionization process can be thought of as the charged particle traversing the matter, and imparting some of its energy to an electron, and this process is repeated many times as the charged particle encounters additional electrons. The mean rate of energy loss in a target can be represented by the Bethe-Bloch equation (Attix 1986; Durante & Cucinotta 2011):

$$S = \frac{4\pi Z_p^2 \rho Z_T N_A e^4}{A_T m \beta^2 c^2}\left[\left\{\ln\left(\frac{2mc^2\beta^2\gamma^2}{I}\right) - \beta^2 - \frac{C(\beta)}{Z_T} + Z_P L_1(\beta) + Z_p^2 L_2(\beta) + L_3(\beta)\right\}\right]$$

Eqn 2.6

where S is the stopping power with units of LET, e is the electronic charge, N_A is Avogadro's number, ρ is the target density, *m* is the electron mass, c is the speed of light, Z_p is the atomic number of the incident particle, Z_t is the atomic number of the target, *I* is the mean excitation energy, and β is the particle velocity divided by the speed of light, γ = $(1-\beta^2)^{-2}$. The correction terms employed are the shell correction $C(\beta)$, the Barkas correction $L_1(\beta)$, the Bloch term $L_2(\beta)$, and the Mott and density corrections $L_3(\beta)$.

In order for a nuclear interaction to occur, the nucleons in the incident particle, or projectile, must interact with the nucleons in the target. The energy must be sufficient to overcome the natural electromagnetic repulsion between the protons, called the Coulomb barrier. If the energy of the particle is below the barrier, the nuclei will "bounce off" one another. When a collision occurs between the incident particle and a target nucleus, either the beam particle scatters elastically leaving the target nucleus in its ground state or the target nucleus is internally excited and subsequently decays by emitting radiation or nucleons. When a particle, such as a neutron or a proton, interacts with a target nucleus, it can "scatter," changing its direction of travel and its kinetic energy. The scattering can be "elastic" or "inelastic". In elastic scattering, the target nucleus remains in its ground state, but in inelastic scattering, it can absorb energy from the incident particle and the absorbed energy usually is re-emitted as gamma rays. Both of these events are "two-body" collisions, much like billiard-ball collisions, and the products fly off at different angles. By mathematical analysis, the energies of the scattered particle and the recoil nucleus can be completely determined by the angle of emission of the scattered particle. The angular distributions of many interactions have previously been measured or calculated (Attix 1986; LANL 2010). The probability of nuclear reactions can be approximated by the Bradt-Peters equation:

$$\sigma = \pi r_0^2 c_1(E)(A_p^{\frac{1}{3}} + A_T^{\frac{1}{3}} - c_2\,(\mathrm{E}))^2 \qquad \text{Eqn. 2.7}$$

where σ is the fragmentation cross-section, A_p and A_T are the atomic weight of the projectile and target, respectively, and r_0 is the nucleon radius. In this case, the energy dependent corrections to the geometrical cross-section are provided by the semi-empirical terms c_1 and c_2.

If we evaluate the stopping power described in Equation 2.6 per unit mass, we show that the mass stopping power or energy lost per gram of target material is the following proportion:

$$\frac{S}{\rho} \propto \frac{Z_T}{A_T} \qquad \text{Eqn. 2.8}$$

The number of nuclear interactions per unit mass is also proportional to fragmentation cross section per unit mass. To a first approximation, σ is proportional to $A^{2/3}$. Consequently, the nuclear transmission is proportional to $1/A^{1/3}$ so the following proportion holds:

$$\frac{\sigma}{A_T} \propto A_T^{-\frac{1}{3}} \qquad \text{Eqn. 2.9}$$

Therefore, the electromagnetic and nuclear energy deposition per unit target mass decreases with increasing atomic weight of the shielding, $A_{T,}$ leading to the conclusion that light materials are more effective for shielding in space. The dependence of energy loss on the Z_T/A_T ratio implies that hydrogen is the optimal material for slowing particles since its ratio is one. (Wilson et al. 1997; Wilson et al. 1991).

SPACE RADIATION TRANSPORT - TRANSPORT CODES

To calculate the radiation environment at a particular location inside the spacecraft, to a particular tissue site, at a given time; shielding models for both the astronaut and the spacecraft are required. A space radiation transport code to calculate the transport of the particles from the external environment through the shielding material provided by the spacecraft and the astronaut's body is also required. There are two types of radiation transport codes, Monte-Carlo and deterministic codes. Monte-Carlo codes such as PHITS (Sato et al. 2013), High Energy Transport Code - Human Exploration and Development in Space (HETC-HEDS) (Townsend et al. 2005), FLUctuating KAskades (FLUKA) (Battistoni et al. 2007; Ferrari et al. 2005) and Geant4 (Agostinelli et al. 2003) use statistical methods for determination of particle trajectories. Deterministic codes such as HZE TRaNsport code (HZETRN) (Wilson et al. 1995) utilize approximate solutions to the Boltzmann transport equation given in Eqn. 2. 4.

Monte Carlo Codes

PHITS is a general purpose Monte Carlo particle transport code written in Fortran 77. PHITS can calculate the transport of all particles (nucleons, nuclei, mesons, photons, and electrons) over wide energy ranges, using several nuclear reaction models and nuclear data libraries. Geometrical configuration of the simulation can be set with or Combinatorial Geometry (CG) or General Geometry (GG) systems. Various quantities such as heat deposition, track length and production yields can be deduced from the simulation, using implemented estimator functions called "tallies". Using the graphics code provided, ANGEL, PHITS also has a function to draw 2D and 3D figures of the calculated results as well as the simulation geometries. PHITS can be executed on almost all computers (Sato et al. 2013). Since PHITS was chosen for this work, a more detailed description of PHITS, the physics models implemented, and the reasons for selecting is contained in Chapter 3 of this dissertation.

HETC-HEDS is a NASA developed extension of the HETC originally developed at Oakridge National Laboratory to provide a method for three dimensional transport of heavy ions in space. It is capable of carrying out three-dimensional transport of the heavy ions in the space environment. HETC-HEDS simulates particle cascades by using Monte Carlo methods to compute the trajectories of the primary particle and all the secondary particles produced in nuclear collisions. The particles considered by HETC-HEDS (protons, neutrons, pions, muons, light ions and heavy ions) can be distributed in angle, energy, and space. Each particle in the cascade is followed until it disappears by escaping from the boundaries of the system, undergoes a nuclear collision or absorption, comes to rest due to energy losses from ionization and excitation of atomic electrons in the target medium, or decays in the case of pions and muons. Neutrons produced below the specified cutoff of 20 MeV and photons produced in the cascade from pion decays or from de-excitation are not transported. However, information regarding the neutrons and photons is stored for transport by other codes such as

MORSE, MCNP, and EGS. HETC-HEDS provides a complete history tape of all cascades so that analyses of specific problems can be performed. For a more in depth review of the physics models incorporated in HETC-HEDS, the reader is referred to the code's reference publication (Townsend et al. 2005).

FLUKA is a general purpose tool for calculations of particle transport and interactions with matter, covering an extended range of applications spanning proton and electron accelerator shielding, target design, calorimetry, activation, dosimetry, detector design, accelerator driven systems, cosmic rays, neutrino physics, and radiotherapy. FLUKA can simulate with high accuracy, the interaction and propagation in matter of about 60 different particles, including photons and electrons from 1 keV to thousands of TeV; neutrinos and muons of any energy; hadrons of energies up to 20 TeV with up to 10 PeV possible by linking FLUKA with the Dual Parton Model (DPMJET) code; neutrons down to thermal energies; heavy ions; and all the corresponding antiparticles. The program can also transport polarized photons (e.g., synchrotron radiation) and optical photons. Time evolution and tracking of emitted radiation from unstable residual nuclei can be performed online. FLUKA can handle even very complex geometries, using its improved version of the well-known Combinatorial Geometry (CG) package. The FLUKA CG has been designed to track correctly also charged particles (even in the presence of magnetic or electric fields). Various visualization and debugging tools are also available. For most applications, no programming is required from the user. However, a number of user interface routines written in Fortran 77 are available for users with special requirements (Ferrari et al. 2005). For a complete description of the physics models used in FLUKA, the reader is referred to the code's user manual (Fasso et al. 2011).

GEANT4 is a toolkit for simulating the passage of particles through matter. It includes a complete range of functionality including particle tracking, geometry, physics models and hits (a snapshot of the physical interaction of a track in a detector). It has been used in applications in particle physics, nuclear physics, accelerator design, space engineering, and medical physics. The physics processes provided cover a comprehensive range, including electromagnetic, hadronic and optical processes, a large set of long-lived particles, materials and elements; all over a wide energy range starting, in some cases, from 250 eV and extending in others to the TeV energy range. It has been designed and constructed to expose the physics models utilized, to handle complex geometries, and to enable easy adaptation for optimal use in different types of applications. The toolkit is the result of a worldwide collaboration of physicists and software engineers. Geant4 is unique as it has been created exploiting software engineering and object-oriented technology and implemented in the C++ programming language (Agostinelli et al. 2003).

Deterministic Codes

NASA has developed a suite of transport codes, HZETRN, to solve the HZE portion (A > 4) of equation 2.4 with the continuous slowing down and straight ahead approximations (Wilson et al. 1991). Solutions obtained with HZETRN can be coupled with solutions obtained from a BRNTRN, which is a light ion code used to obtain the transport of the full GCR spectrum (Wilson et al. 1988). NASA has developed two different nuclear fragmentation models, the Quantum Multiple Scattering Fragmentation Model (QMSFRG) and the Nuclear Fragmentation Model (NUCFRG) and both have been used in work with HZETRN. NUCFRG2 is a semi-empirical abrasion-ablation model and QMSFRG is a non-relativistic quantum multiple scattering model of nuclear fragmentation based on the Glauber formalism (Cucinotta et al. 2013).

Comparison of Transport Codes

Each of the computer codes described previously is a well proven application and has gone through extensive validation for spaceflight and accelerator applications. In general there are three ways to assess the uncertainties in transport code results (Durante & Cucinotta 2011):

- Comparison of the code results to ground based measurements for both thick and thin targets for different materials compositions and amounts.
- Inter-comparison of the codes for matched geometries and environments.
- Comparison of the code results to spaceflight measurements.

A comprehensive literature review of the comparison of each of these codes to experimental measurements was undertaken. During the development of the heavy ion transport models within each software package, code have undergone significant benchmarking with accelerator measurements of ions and energies relevant to the space environment. The publications are too numerous for thorough discussion here, so representative publications for each code are discussed. In an early publication on the PHITS code (Iwase et al. 2002), the authors began confirming the accuracy of the heavy ion transport calculations, particularly for production of secondary particles and neutrons. The code was also shown to provide good results on the angular distribution of secondary neutron energy spectra produced from the irradiation of thick carbon, aluminum, copper and lead targets by 100 MeV/n carbon, 400 MeV/n carbon, and 400 MeV/n iron ions. Following the addition of an event generator for low energy neutron transport in 2007 (Iwamoto et al. 2007) and through the comparison to published secondary neutron spectra, PHITS was able to reproduce the secondary neutron spectra in a wide neutron-energy regime (Satoh et al. 2007). Sato et al. (2005) and Zeitlin et al. (2008), used PHITS to simulate the fragmentation distributions determined by Zeitlin et al. (2004) and was shown to have overall good agreement with the experimental data. However, an under prediction was seen. Comparison of the HETC-HEDS code predictions and measured energy loss data for 1.063 GeV/n iron ions irradiating carbon and aluminum targets, 600 MeV/n irradiating a polyethylene target and 800 MeV/n irradiating a tin target was performed in Charara et al. (2008). The authors found that HETC-HEDS reproduced the energy loss spectra well for the iron ions on aluminum but over predicted the spectra in the other ion and target combinations. A limitation in these results is that neutron and photon production are not benchmarked. FLUKA's history can be traced to early development work in 1964 and the code distribution and management has become a large international collaboration. Therefore, there are numerous publications that benchmark FLUKA to experimental measurements. In the last 15 years, the code has evolved from a high energy physics code to being able to transport particles of a wider energy range, from roughly 100 MeV/n to cosmic ray energies. Fasso et al. (2003) found good agreement with the expanded physics models and experimental data from various sources. The work was performed in collaboration with the University of Houston under a grant from NASA in an effort to incorporate spacecraft geometries in three dimensional Monte Carlo calculations. Geant4 is used by the European Space Agency and work has been performed to improve its hadron interaction models to include the ions present in the space radiation environment. In Ivanchenko et al. (2012) the authors concluded that Geant4 should be able to describe the nuclear interactions in a space radiation environment. Good results were found for hadron interactions with atomic nuclei in the energy interval 10 MeV–15 GeV for interactions of neutrons, protons, and pions and for ions in the energy interval 100 MeV/n–1.5 GeV/n. The comparisons do show some uncertainty with the production of light ions.

The broad energy beam boundary conditions in HZETRN neglect range or energy straggling. This approximation is appropriate for the use in spaceflight calculations; however, energy straggling become more important in ion beam calculations, so NASA has developed a related code GREENTRN with narrow energy beam (or monoenergetic) boundary conditions for use in accelerator measurements . The energy loss spectra calculated with NUCFRG fragmentation model was compared to experimental data from taken at Brookhaven National Laboratory Alternating Gradient Synchrotron (Walker et al. 2005) and then a computational inter-comparison of same energy loss spectra for NUCFRG and QMSFRG was performed. The authors concluded that the calculated spectra showed reasonable agreement in shape with the experimental results.

However, there were some discrepancies identified in the lower values of energy deposited indicating the need for further model refinement and comparison with experimental data. For light ion modelling, NASA has developed a Monte Carlo based transport code, the GCR Event-based Risk Model (GERMCode) for use in evaluating accelerator measurements at Brookhaven National Lab's NASA Space Radiation Laboratory (NRSL). The GERMCode uses the QMSFRG for a nuclear interaction data base and atomic energy loss subroutines from HZETRN. GERMCode has been benchmarked with many measurements by Zeitlin et al. (2008) and shows good agreement with these measurements (Cucinotta et al. 2011).

Individually these codes compare well with experimental measurements leading several research groups to perform inter-comparisons of the codes. Several of these comparisons are discussed. The results of comparisons of PHITS, FLUKA, and HZETRN and experimental data taken with silicon detectors and plastic nuclear track detectors were discussed in Durante & Kronenberg (2005). Whereas agreement between the experiments and all three codes was seen, HZETRN tended to overestimate the protons produced. This over estimation was expected due to HZETRN's use of the forward approximation that does not account for lateral scattering of the ions transported. The production neutrons and photons at angles of 7.5, 30, 60, and 150 degrees resulting from the irradiation of beryllium, carbon, aluminum and iron target materials with moderate energy protons was compared for FLUKA, MCNP, and PHITS in Oh et al. (2011). The results calculated using FLUKA and PHITS agree well with the experimental results; however, MCNPX showed an under prediction at every energy range except for an unusual over prediction at the highest energies. The authors found better results when the LA150 cross section library was used with MCNPX. In this publication the authors also evaluated results from the two intra-nuclear cascade models available in PHITS, Bertini and Jaeri Quantum Molecular Dynamics (JQMD) and found that JQMD was better at predicting the experimental results. As consequence of these results, JQMD was chosen for the PHITS simulations in the work described in the methods section of this paper. In Sihver et al. (2008), the authors used measured fragmentation cross sections previously obtained and published by the Lawrence Berkley Laboratory (LBL) group and described in Zeitlin et al. (2010), which they compared to predictions from PHITS, HETC-HEDS, MCNPX , FLUKA, and HZETRN's NUCFRG. Both HETC-HEDS and NUCFRG were shown to not reproduce the odd-even effect seen in the experimental data. However, all of the codes are shown to underestimate the fragmentation cross sections and a slight underestimation of the charge changing cross sections.

NCRP Report 153 provides a comprehensive review of many of the spaceflight measurements compared to predicted values from HZETRN (NCRP 2006). In addition, within the HZETRN suite, both fragmentation models have been well validated with space measurements (Cucinotta et al. 2008; Slaba et al. 2011). Since Monte Carlo calculations generally require long computational times, comparing Monte Carlo predictions to spaceflight measurements usually require that simplified geometries be used leading to uncertainties in the results. As an example, simulations of the MATROSHKA-R experiment on the ISS, the Russian Service Module was modelled as sphere of aluminum with varying areal densities from 3 - 5 g/cm^2 with the MATROSHKA-

R spherical phantom inside. In reality the geometry of the Russian Service Module is more complicated. The best overall agreement between averaged simulated absorbed doses and those measured by the detectors on the phantom surface was achieved when using a mass thickness of about 4 g/cm^2. The measured average absorbed dose was 172 µGy/day and the simulated average absorbed doses were 196 µGy/day and 153 µGy/day for 3 g/cm^2 and 5 g/cm^2 of aluminum shielding, respectively (Koliskova et al. 2012).

SHIELDING IN SPACE

In the early space missions, radiation doses from GCR were considered negligible as mission durations were short. For example, Apollo missions were 10 days or less and Shuttle missions were two weeks or less. The unpredictable nature of SPEs was of principle concern due the potential for high exposures leading to clinical detriment. The aluminum hull of the spacecraft was the only shielding provided. With the increasing duration of missions at the ISS, and planning for long duration exploratory missions, the inclusion of parasitic shielding has been investigated (Shavers et al. 2004; Kodaira et al. 2014). In this publication the authors note that operational constraints for retrofitted shield materials include launch mass and access to a launch vehicle. This publication was written following the Space Shuttle Columbia accident and the Shuttle was grounded. Access to the ISS was solely through Soyuz and Progress launches and launch mass was extremely constrained. Other habitability factors described include consideration of air ventilation and materials off-gassing, flammability, and noise. Perhaps the most challenging constraint for retrofitted shields is the reduction of inhabitable volume. Hydrogenous materials have been shown to be the most effective at reducing exposure to GCR. Therefore, NASA evaluated the effectiveness of including polyethylene bricks in the astronaut sleep quarters and found as much as a 20% reduction in total dose equivalent. The actual dose equivalent reduction is less due to the number of hours the astronaut spends in the sleep quarters. The authors also noted that shielding material readily available on a spacecraft usually include spacecraft structure and contents, including support hardware, payloads, storage of water, food, clothes, paper, debris shields, and even the crewmembers. Following the success reported in Shavers et al. (2004), NASA designed the sleep quarters for Node 2 of the US operating segment, to include incorporate prudent choices of construction materials including the incorporation of polyethylene panels to reduce dose equivalent. A reduction of about 5% in dose equivalent from GCR was predicted for a mission. This reduction estimated the number of hours an astronaut would spend in their sleep quarters (NASA 2006). The Russian starboard crew cabin is only shielded by a thin aluminum panel necessitating the need for the inclusion of additional shielding material. A “protective curtain” of packaged wet hygiene wipes and towels was constructed along the outer wall of the crew quarters, adding 6.3 g/cm^2 areal density of shielding. Using thermoluminescent detectors and nuclear track detectors, a dose reduction of 37% (total) was measured in the crew quarters (Kodaira et al. 2014).

Shielding Experiments at Accelerators

NASA in conjunction with the US Department of Energy funded the LBL group to conduct a series of experiments to obtain the percentage dose reduction per unit thickness for a variety of ions and materials. The experiments confirmed the predictions of Wilson, et al. (1991) that doses from light ions were the most effectively shielded and that hydrogen was the best suited for this task. Hydrogen is an impractical spacecraft construction material, but the experimental measurements showed that practical materials like polyethylene and polymethylmethacylate (PMMA) had similar dose reduction capabilities and were superior to aluminum (Guetersloh et al. 2006; Miller et al. 2003; Zeitlin et al. 2006; Zeitlin et al. 2008).

The European Space Agency (ESA) has also funded a series of experiments to evaluate the shielding effectiveness of spacecraft construction materials. Kevlar® and Nextel® are materials commonly used in space structures to protect against micrometeorites. Using Bragg curves, the authors in Lobascio et al. 2008 estimated the shielding effectiveness of the materials using accelerator measurements and found that while polyethylene provided the largest dose reduction, Kevlar® provided between 80-90% of the reduction in dose obtained from polyethylene when irradiated with 1GeV/n ^{56}Fe ions. Both Kevlar® and Nextel® provide more attenuation than the same mass of aluminum. These results provided evidence to use more realistic layered spacecraft structure materials in this dissertation work. Accelerator measurements have also been taken for 1 GeV proton beams with aluminum and PMMA (Bertucci et al. 2007; Mancusi et al. 2007). In this work the authors found that the dose increased by 40% and 60% when shielded by 20 g/cm^2 of PMMA and aluminum respectively. The dose rate decreased with increasing distance from the shield; however, it remained elevated for up to 20 cm. The authors used PHITS to determine the increase in dose was due to secondary particles created from nuclear interactions in the shielding material.

The testing of the composite materials used in the construction of the walls of the Columbus module on the ISS and an inflatable habitat was reported in Silvestri et al. (2011). The composite wall materials tested included layers of Kevlar® and Nextel® in thicknesses consistent with spacecraft design. The authors reported that the composite materials provided more dose reduction than an equivalent areal density of aluminum and this improvement in shielding effectiveness is attributed to the addition of Kevlar® and Nextel®. The composite materials were shown to reduce the dose more than an equivalent areal density of aluminum. Simulations of the fragmentation distributions using GEANT4 were also reported. The simulations reproduced the odd-even effect and when the areal density is increased the amount of fragmentation is increased. Similar tests for the composite materials from the Columbus module and an inflatable habitat irradiated with protons were reported in Destefanis et al. (2008). GEANT4 was used to simulate the experiment and the results indicate a good agreement between experimental data and simulations.

Finally, ESA is currently sponsoring a set of measurements at GSI Helmholtz Centre for Heavy Ion Research in Germany, to test in situ planetary materials, Mars and Lunar regolith, and novelmaterials with very high hydrogen content and excellent structural properties (Durante 2014).

Chapter 3: Methods

Physical Measurements

Accelerator Beam and Dosimetry

As described earlier, highly energetic GCR can penetrate many g/cm^2 of matter, while protons are easier to shield. To assess the space radiation protection capabilities provided by several materials used in space vehicle construction, ground tests were performed at NASA's Space Research Laboratory (NSRL) at Brookhaven National Laboratory (BNL). In order to compare results to the GCR appropriately, a 1 GeV/n ^{56}Fe beam was chosen as it is the roughly the median energy of the primary GCR fluence and has been shown to be representative of the heavy-ion component of the GCR (Zeitlin et al. 2008). Additionally, solar particle events are composed largely of energetic protons with an energy range up to 10 GeV and GCR is 98% protons with a median energy of 1 GeV. Therefore, 1 GeV protons were accelerated. (NCRP 2006)

^{56}Fe ion Beam Dosimetry

A ^{56}Fe beam of 964.9 MeV/n was used with a range of 12.6 cm or 34 g/ cm^2 of aluminum. The LET in water is stated as 151 keV/µm. The size of the beam was about 20 cm x 20 cm, with a stated disuniformity below 5%. Three parallel plate ionization chambers were used as the beam monitors, and the absorbed dose was measured by the Far West Technology, Inc. model IC-17A ionization chamber, also called the Egg Chamber The Egg Chamber is a three terminal 1cm^3 spherical ionization chamber with a 0.05 mm thick tissue equivalent plastic wall. The spherical detector is mounted on the end of a stem with the signal connections made through a terminal block. The block contains a Bayonet Neill–Concelman (BNC) signal connector and a miniature high voltage (MHV) high voltage connector. The stem effects are less than 1×10^{-12}A for a 1×10^4 R/h exposure with Co-60. The effect may be minimized by using a positive and negative collecting voltage on the detector and averaging the readings. The Egg Chamber is calibrated annually using a Cs-137 gamma ray source. The calibration is based on the standard defined in ICRU Report 59 (1998) (Far West Technologies 2001; BNL 2011). All samples were placed normal to the beam and absorbed dose was measured following the shield for the seven different configurations listed in Table 3.1. Dose was measured for each configuration twice in order to ensure consistency in the measurement and reduce uncertainty.

Configurations for ^{56}Fe Runs	**Dimensions (cm^2)**
Columbus shield	9 x 8
Columbus with internal structure model	10 x 10
Inflatable habitat material, REMSIM	9 x 8
Inflatable habitat material, REMSIM with water	9 x 8
Aluminum	20 x 20
Polyethylene	20 x 20
Aluminum and Polyethylene with changing mutual position	20 x 20

Table 3.1: Dimensions for shielding configurations tested for ^{56}Fe beams.

Proton Beam Dosimetry

A proton beam of 1 GeV was accelerated. The LET in water is stated at 0.22 keV/µm. The size of the beam was about 20 cm x 20 cm, and its stated disuniformity at the accelerator window was reported below 5%. For some of the measurements taken, the proton beam size was reduced to 10 cm x 10 cm to reduce data acquisition time. As described in the ^{56}Fe dosimetry section, three parallel plate ionization chambers were used as beam monitors, and the absorbed dose was measured by the Egg Chamber. All samples were again placed normal to the beam and dose was measured in the five different configurations listed in Table 3-2. Again, dose measurements were taken twice for most of the measurements to ensure consistency. However, on the day of the proton beam experiments, the Relativistic Heavy Ion Collider was running leading to lengthy data acquisition times. Consequently, only one dose measurement was taken due to time limitations.

Configurations for Proton Runs	**Dimensions (cm^2)**
Columbus with internal structure model	10 x 10
Inflatable habitat material, REMSIM with water	9 x 8
Aluminum	20 x 20
Polyethylene	20 x 20
Aluminum and Polyethylene with changing mutual position	20 x 20

Table 3-2: Dimensions for shielding configurations tested for proton beams.

Bragg Peak Measurements

At the beginning of each day, the kinetic energy of the NSRL Beam is determined by measuring the Bragg Peak. The relative LET is measured using the secondary ion chambers as increasing thicknesses of high density polyethylene are sequentially inserted using the range shifter into the path of the beam. When a critical thickness is reached, the beam particles will slow down enough in the polyethylene to stop in the ion chamber, giving a peak in the observed LET. From the location of the stopping peak, the NRSL staff derived the kinetic energy of the beam, and the LET that a beam of that kinetic energy would deposit in water. The experimental plot of the Bragg Peak for the ^{56}Fe beam on the day of the experiments is shown in Figure 3.1 as the LET measured in the ion chamber as a function of the thickness of polyethylene. The range of 1 GeV protons in polyethylene is 318 cm which is much larger than the irradiation chamber at BNL and therefore a Bragg Peak was not measured.

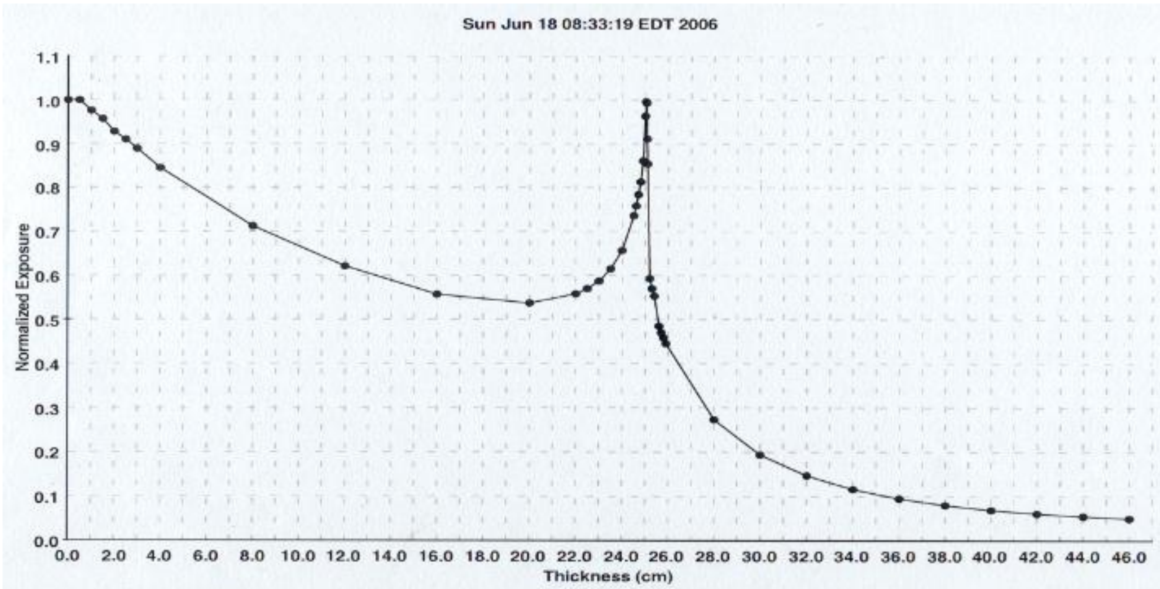

Figure 3.1: BNL Measured Bragg curve vs. residual range for ^{56}Fe ions inside polyethylene (density 0.97 g/cm^3).

OVERVIEW OF THE MAJOR EXPERIMENTAL CONFIGURATIONS

Space vehicle development largely uses available materials and technologies so the knowledge of the behavior of existing structures in extreme environments is a key point. The materials of interest in this study are typical space vehicle construction materials such as aluminum, Kevlar® and polyethylene because there is a lot of previous experimental and computational work to study shielding performance of these materials. It is important to note that air gaps that would be present in the actual spacecraft construction are not included in the mock-ups used in this work, as they have negligible effect on the results.

Description of the Columbus without Internal Structures Model

The Columbus module is typical of the construction of the other modules in the United States Operating Segment of the International Space Station. These modules are comprised of three cylindrical sections and two end-cones. Each end-cone contains a hatch opening through which the astronauts will enter and exit from module to the next module. The exterior of a module is made of aluminum and has a "waffle" pattern that strengthens the hull. It is covered with a multilayer insulation (MLI) blanket to protect the module from the temperature extremes of space. An intermediate debris shield made of Kevlar protects the module against space debris and micrometeoroids. Another insulation layer made of Nextel is next followed by an aluminum debris shield for added micrometeoroid protection and to reflect the intense sunlight reducing the heat load on the module. Figure 3.2 is a good illustration of the components of the Columbus module.

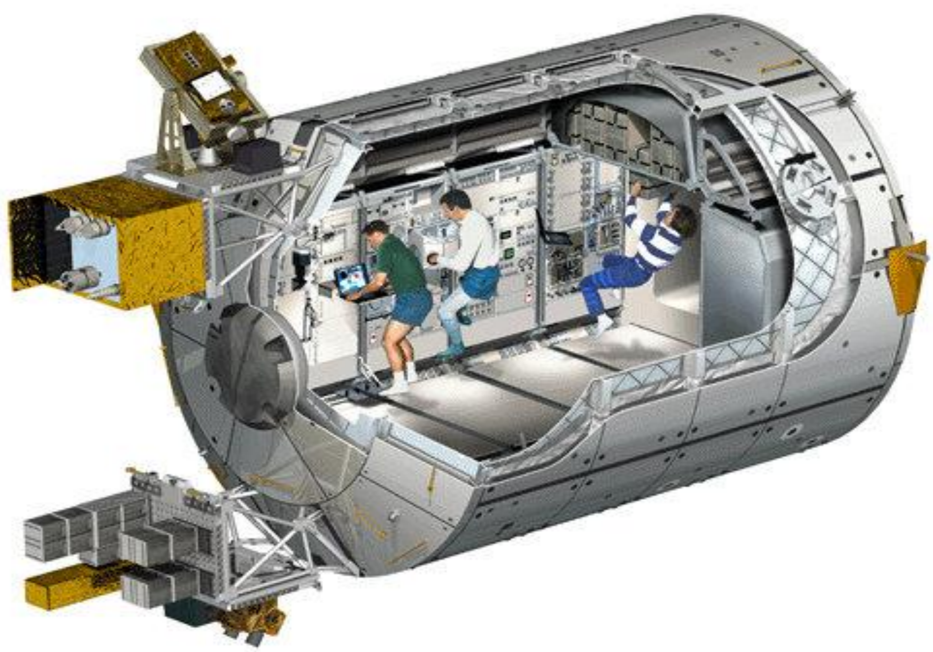

Figure 3.2: Cutaway view of the Columbus Laboratory.

For the experiments, the mock-up of the Columbus module shown in Figure 3.3 is representative of the actual configuration of the external shell utilized for the Columbus model. This configuration is composed, as shown in Table 3.3, of aluminum at the first bumper, Nextel®, Kevlar® epoxy and MLI at the second bumper, and finally the aluminum pressurized shell or wall bumper (Destefanis et al. 2008; Silvestri et al. 2011). Mylar is used in the experimental configuration to contain the layers and has a negligible effect on the results.

Material	**Areal Density [g/cm^2]**	**Thickness [cm]**
Al2219	0.7	0.25
Nextel®	0.4	0.55
Kevlar®	0.9	0.8
MLI	0.2	0.13
Al2219	1.3	0.48
Areal Density [g/cm^2]	**Total Thickness [cm]**	
3.5	2.2	

Table 3.3: Materials for the multilayer Columbus mock-up.

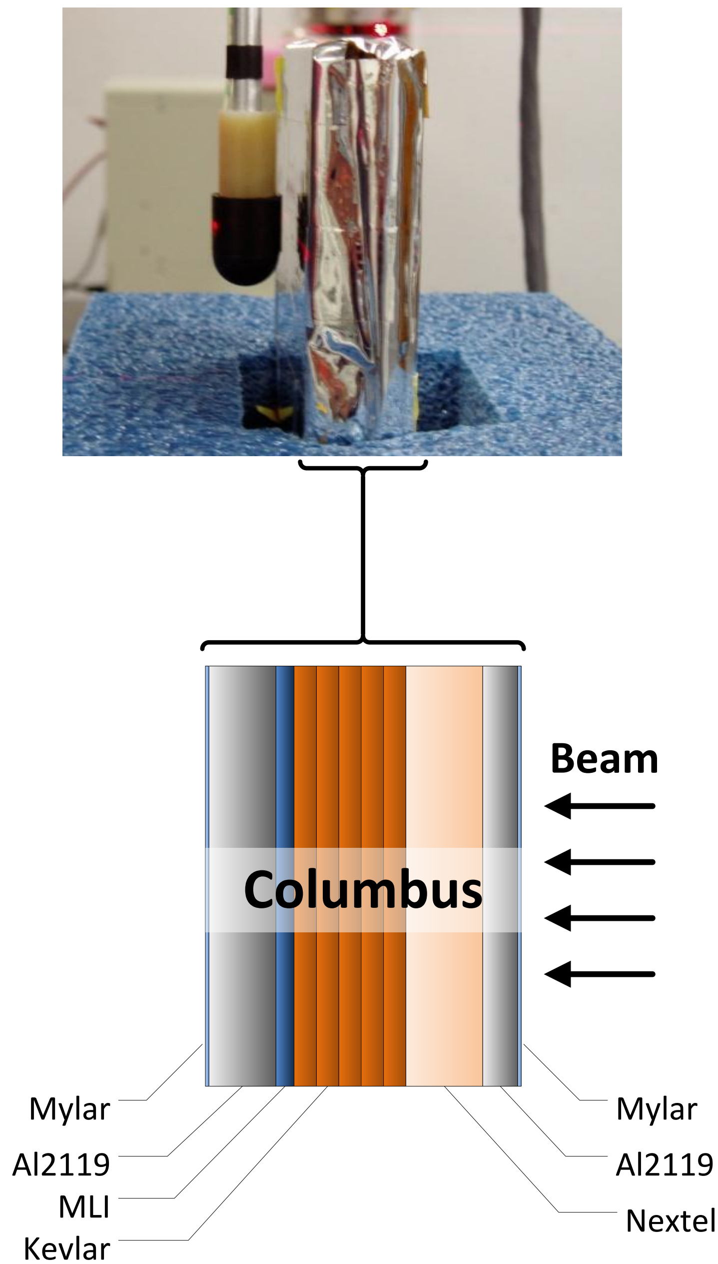

Figure 3.3: Multi-layer Columbus without internal structure mock-up. Details of layers provided in relative scale.

Rigid Multi-layer Columbus with Internal Structures

As shown in Figure 3.2, the habitable volume where astronauts work and live is surrounded by a large number of devices and structures. Aluminum interior structures provide space for power lines, data management systems, vacuum systems, air conditioning ducts, water lines and more, all supporting the space station's rack system. There are 10 aluminum racks inside the laboratory, six on each side. Each rack is 73 inches (1.9 meters) tall and 42 inches (1.1 meters) wide, basically, the size of the average household closet. Made with a graphite composite shell, racks inside the International Space Station lab are largely aluminum and weigh around 1,200 pounds (544 kilograms) each (ESA, 1012). Figure 3.2 provides an illustration of the rack system present on an ISS module. The racks are composed for the most part of aluminum and composite material that are positioned between the module walls and the astronauts' livable volume, therefore, providing further protection against the effects of a radiation exposure. In order to test the potential protection afforded by these materials, it was important to determine the equivalent density of the material constituting the internal "out-fittings" in order to explore their role in the interaction with radiation. A simple row estimation of these materials was performed. Two different configurations were considered: the configuration of the module at launch and the on-orbit configuration. The difference is a matter of the total weight and number of racks present during the launch phase. This includes only the indispensable hardware and devices that are present in order to accomplish all the operations were needed to attach it to the ISS. After the commissioning procedures a maximum of 10 racks (998 kg each) can be accommodated inside the module and 4 outside (370 kg each). During the launch phase the total internal mass could be 6000 kg. We assumed that this mass could be thought as uniformly distributed along the walls of the module. Aluminum represents about the 60% of the total mass inside the module. The remaining mass is attributed to liquid from propellant and water tanks and then plastic and composite materials contained in the modules electronics. In order to leverage previous work done to characterize the radiation protection properties of Nextel® and Kevlar®, the remaining materials were approximated as Kevlar® (Destefanis et al. 2008; Lobascio et al. 2008; Silvestri et al. 2011).

Material	Areal Density [g/cm^2]	Total Thickness [cm]
Al	0.7	0.25
Nextel®	0.4	0.55
Kevlar®	0.9	0.6
MLI	0.2	0.13
Al	1.3	0.48
Al	7.4	3
Kevlar®	3.8	2.9
Areal Density [g/cm^2]	**Total Thickness [cm]**	
15	8	

Table 3.4: Materials for multilayer Columbus type with internal structure mock up.

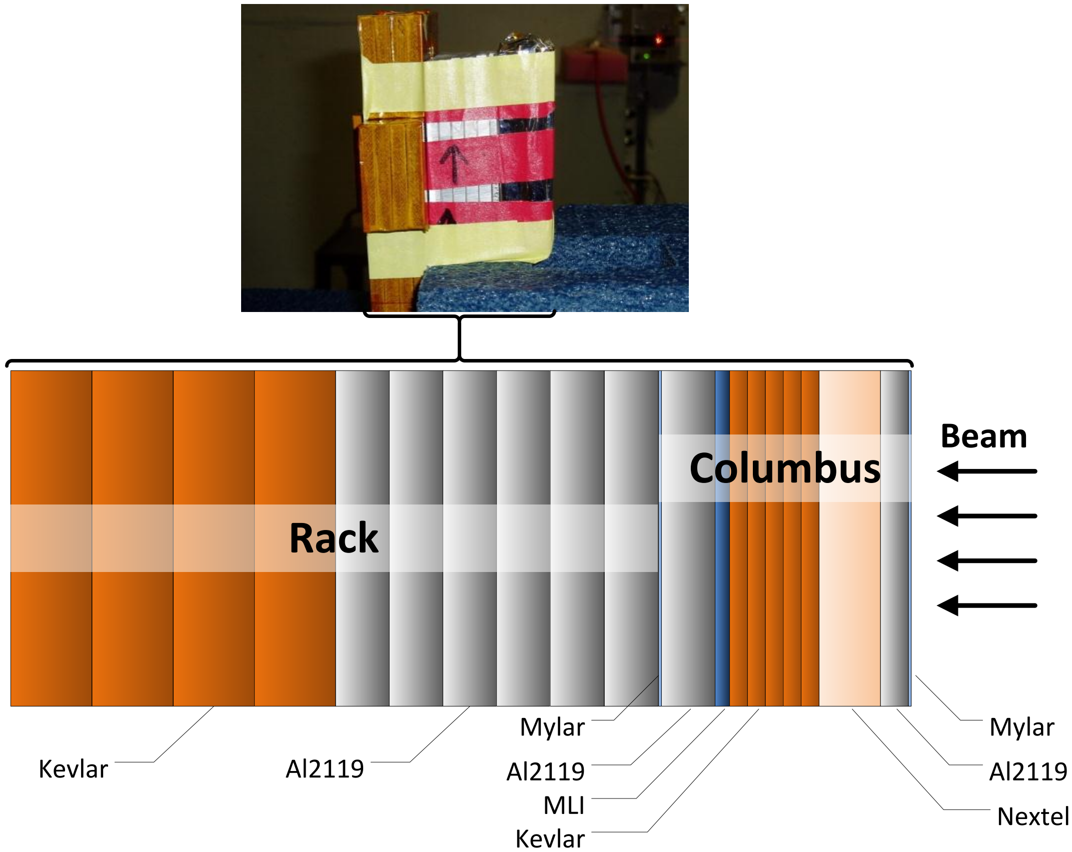

Figure 3.4: Columbus and internal vehicle structure mock up from experiment. Detail of layers provided in relative scale.

Description of the Flexible Multi-layer Inflatable Habitat Mock-up.

Mass and volume constraints inherent in spaceflight have led to the design and development of alternatives to the traditional aluminum shell. Inflatable habitats are not a new concept and have been considered because the vehicle construction materials provide a greater volume of living space for a given mass, and are not constrained by the diameter of the launch vehicle.

Although never flown, the first serious design and manufacture of an inflatable space habitat was in 1961 with a space station design produced by Goodyear (NASA 2013). A proposal released in 1989 by NASA's Johnson Space Center's (JSC) in the Man

Systems Division outlined a 16 meter (52 ft.) diameter spherical habitat lunar outpost partially buried in the lunar surface. (Roberts 1992) Another inflatable module called TransHab was proposed at JSC in the 1990s for the International Space Station, and later the private company Bigelow Aerospace revived the design for use in a number of potential civil and commercial applications. Currently, the Bigelow Expandable Activity Module (BEAM) space habitat will be tested on the International Space Station starting in 2015 for a two-year technology demonstration to test the module's structural integrity, leak rate, radiation dose rate, and temperature changes. Figure 3.5 shows and artist's rendition of the BEAM in space and docked to the ISS (Bigelow Aerospace 2013).

The actual construction of an inflatable space habitat would be determined by mission objectives and driven by the need for protection from the environmental conditions in space. Thermal protection would be provided by layers of MLI covered by an external layer to protect against oxidation from atomic oxygen and degradation due to ultra-violet radiation. The micrometeoroid and orbital debris shield consisting of shock absorbers and ballistic restraint layers would follow. These layers would likely have low density foam spacers in between for added attenuation of debris. Pressure containment would be provided by a structural restraint system and air containment would be provided by a bladder system. A final layer of a fire retardant material like Nomex would serve as the protection from fire and any potential damage resulting from crew activities within the spacecraft. An understanding of the radiation dose reduction properties of this vehicle type will be necessary for managing radiation dose and risk during the upcoming technology demonstration.

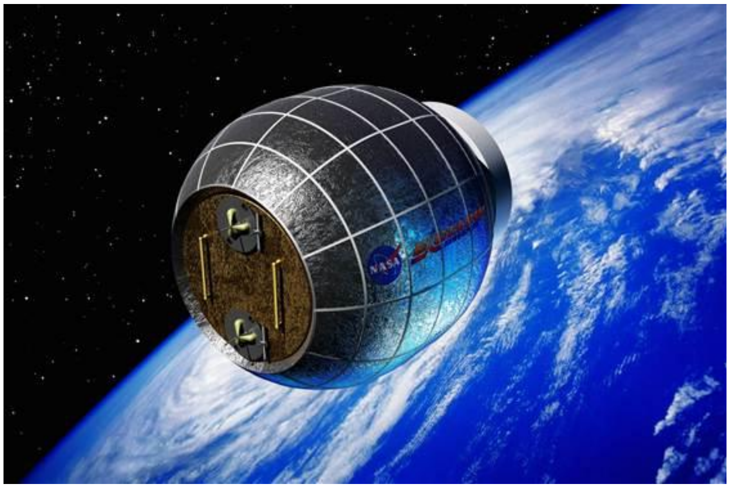

(a)

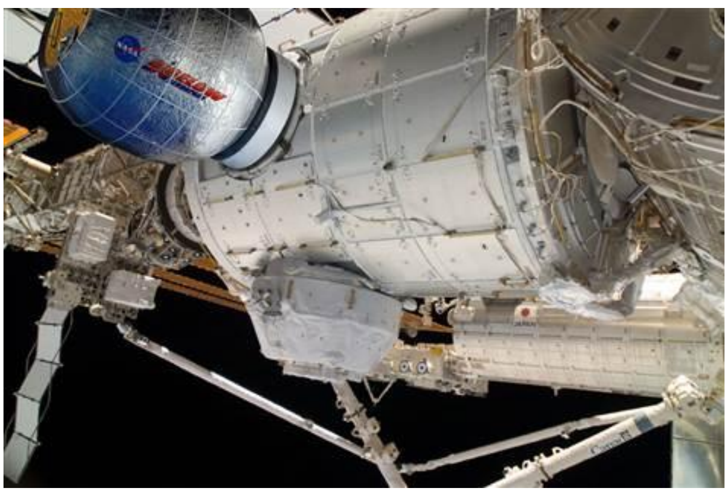

(b)

Figure 3.5: An artist's conception of the BEAM (a) in space and (b) docked to the ISS.

To obtain an understanding of the radiation protection afforded by inflatable habitats, the flexible multi-layer configuration adopted by the European Space Agency collaboration, Radiation Exposure and Mission Strategies for Interplanetary Manned Missions (REMSIM), was used (Cougnet 2005). The experimental configuration, shown as the Mylar coated package in Figure 3.6, consists of a thermal multi-layer insulation, MLI, four Nextel bumpers used to absorb shock from impacting micro-meteoroids, a ballistic restraint multi-layer of Kevlar® used to absorb the kinetic energy of the debris cloud, a structural restraint multi-layer of Kevlar® provides to support pressure loads incurred from inflating the module and to supply further protection. To contain air inside the module, a multi-layer composed by three layers of airtight material separated by two layers of Kevlar® to protect and supply stiffness to the air bladder. A final layer of Nomex provides protection against punctures and fire. In the flight configuration there would be some spacer elements composed of foam needed to guarantee correct spacing between consecutive bumper layers, however, these spacer elements were not used during the irradiations at Brookhaven.

Material	**# of Layers**	**Thickness [cm]**	**Areal Density [g/cm^2]**
MLI + Betacloth	21	0.15	0.08
Nextel®	4	0.55	0.41
Kevlar®	17	0.45	0.36
Bladder	3	0.04	0.05
Nomex	1	0.01	0.01
Water	2	7.4	7.6
Areal Density [g/cm^2]		**Total Thickness [cm]**	
≈ 8.5		8.5	

Table 3.5: Materials for Flexible multi-layer REMSIM type with water added.

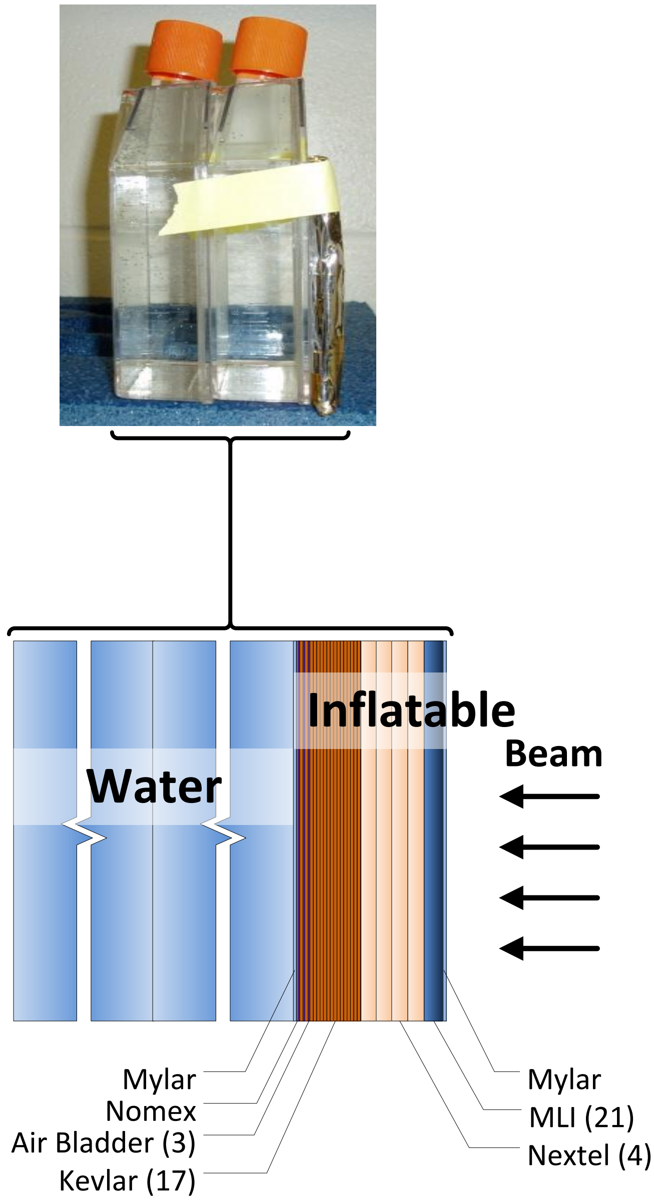

Figure 3.6: Flexible multi-layer REMSIM and water mock-up used in experiments. Detail of layers provided in relative scale.

The future design of inflatable/expandable space vehicles are unknown so accurately modelling the internal configuration like was done with the Columbus mock-up measurements was not possible. However, during the planning of these experiments it was it recognized that the concept of utilizing propellant and drinking water tanks as additional shielding was being considered in vehicle designs; therefore, water was included in the mockup. The REMSIM configuration was placed adjacent to two water filled T75 plastic flasks, 3.7 cm thick each providing an additional 7.6 g/cm^2 of a high hydrogen content material.

Aluminum and polyethylene with mutually changing positions

Many shielding studies have shown that the lighter the material the greater the reduction in dose when shielding space radiation (Wilson et al. 1995; Shavers et al. 2004; Zeitlin et al. 2006). The fragmentation cross section per unit target (T) mass decreases as $A_T^{-1/3}$, while the ionization power increases as Z_T/A_T. Theoretically hydrogen would be the best material for shielding against heavy ions; however, because of the difficulties of containment, no shield with liquid hydrogen has been constructed. To date the practical solution has been to utilize a hydrogen rich material like polyethylene. On the International Space Station, polyethylene shielding layers have been incorporated into the walls of the sleep quarters of the astronauts. The polyethylene sheets are placed interior to the ISS module aluminum hull, but within the rack structure so that the polyethylene is bound on either side with aluminum (Shavers et al. 2004; NRC 2008). In addition, Mancusi et al. (2007) showed that the absorbed dose-rate measured in the sample position increases between 25% and 40% when a proton beam was shielded with the blocks in polymethyl methacrylate (PMMA) and Al of the same areal density(20 g/cm^2). In those studies, aluminum was shown to be responsible for the greatest increase in dose. Space structures are largely made of aluminum, so studying the effects of combining it with polyethylene is a key point in understanding the radiation protection afforded through realistic shielding combinations. Figure 3.7 is a photograph of the 10 g/cm^2 Polyethylene+ 10 g/cm^2 Al configuration. The four configurations tested are as follows:

- 5 g/cm^2 Polyethylene+ 5 g/cm^2 Aluminum
- 5 g/cm^2 Aluminum + 5 g/cm^2 Polyethylene
- 10 g/cm^2 Polyethylene+ 10 g/cm^2 Aluminum
- 10 g/cm^2 Aluminum + 10 g/cm^2 Polyethylene

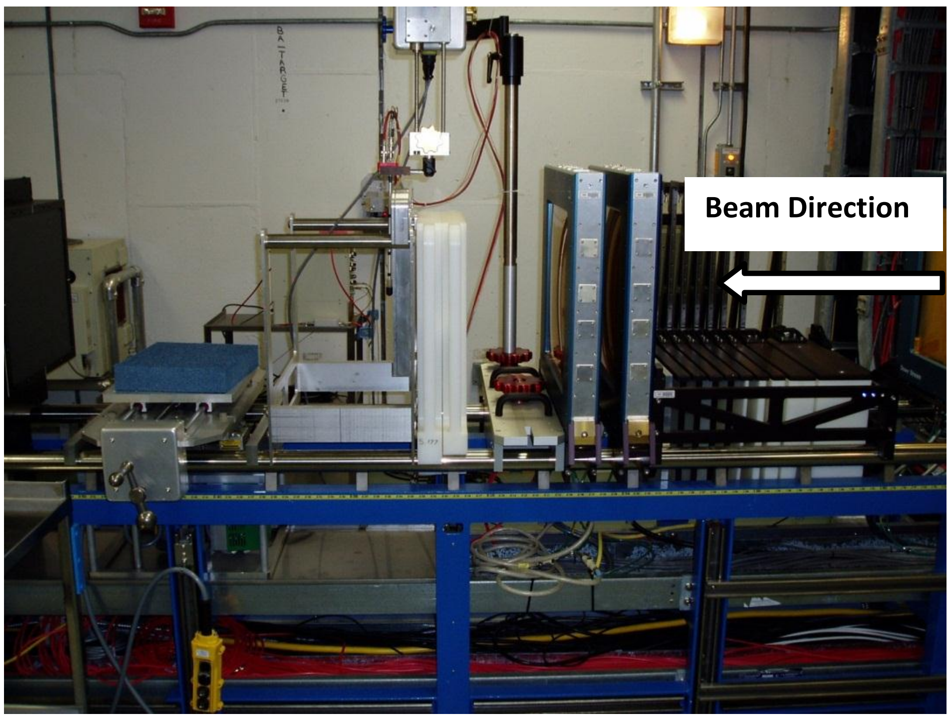

Figure 3.7: Aluminum-polyethylene shielding configuration example - 10 g/cm^2 of polyethylene followed by 10 g/cm^2 aluminum.

Off-axis Measurements of 1 GeV Shielded Proton Beam

In this aim, we extended our investigations to obtain off-axis measurements of a 1 GeV proton beam deposition after traversal of a relatively thin (3 cm) aluminum target. For these measurements a proton beam at 980 MeV was accelerated at BNL

NSRL. The LET in water is about 0.22 keV/μm and the relative energy spread at the accelerator window was reported below 5%. The cylindrical aluminum target, 3x3 cm in size and 2.71 g/cm^3 in density, was positioned with the axis parallel to the beam and supported by low-density polyethylene foam. Experience at Brookhaven has shown that the foam produces minimal scatter and fragmentation and therefore should not have impacted our results. The exit window of the accelerator was located several meters upstream of the three parallel-plate ionization chambers that were used as beam monitors. While one of the parallel plate ionization chambers is visible in Figure 3.8 the exit window is not visible. The location of the Egg chamber was moved along the x-axis from 0- 6 cm while the x and y axes were held constant. Dose was measured using the Egg chamber at these dimensions. The beam dose rate was adjusted in order to provide a sufficient number of particles to deliver 200 cGy to the Egg Chamber.

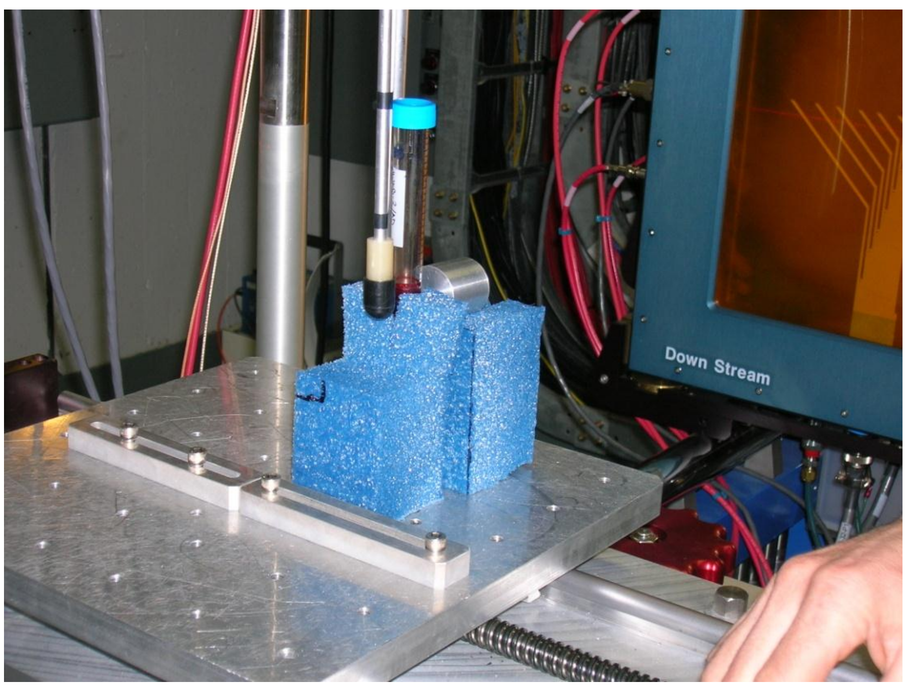

Figure 3.8: Experimental configuration for angular distribution of proton ions shielded by aluminum cylinder. Egg position located at (0cm, 0cm, +1cm).

PHITS SIMULATIONS

PHITS was developed through a collaboration between JAEA (Japan Atomic Energy Agency), RIST (Research Organization for Information Science and Technology), KEK (High Energy Accelerator Research Organization) and Chalmers University of Technology. PHITS is a general purpose Monte-Carlo transport code written in Fortran 77. It can transport all particles (nucleons, nuclei, mesons, photons, and electrons) over wide energy ranges (~100 GeV/n), using various nuclear reaction models and nuclear data libraries. Geometrical configuration of the simulation can be set with either CG or GG systems. Various quantities such as energy deposition, track length and production yields can be deduced from the simulation, using implemented estimator functions called "tallies". The code package also provides a graphics tool, ANGEL, which can be used to create 2D and 3D illustrations of the calculated results as well as the simulation geometries. PHITS can be executed are Windows, Mac, Linux, and Unix platforms (Sato et al. 2013).

PHITS has been used extensively for three-dimensional transport of cosmic ray particles and design of accelerator facilities. It addresses two categories of physical processes, transport process and collision process. It simulates ionization through transport processes under an external field and uses the mean-free path to determine instances of collision (Niita et al. 2006; Sihver et al. 2007). Ionization transport includes angular and energy straggling, showing good agreement for Bragg peaks and fragmentation tails (Niita et al. 2006). For low energy neutron interactions, PHITS employs Evaluated Nuclear Data Files (ENDF) and can be used with any of the internationally available cross section libraries. Most recently the Japanese Evaluated Nuclear Data Libraries (JENDL) are used for interactions up to 20 MeV, and the LA150 libraries for are used interactions up to 150 MeV. ENDF are also used for gamma and electron transport below 1 GeV in the same manner as the Monte Carlo N-Particle (MCNP) code (Sato et al. 2013). For high energy neutrons and other particles, two models, JAM (Jet AA Microscopic Transport Model) and JQMD (JAERI Quantum Molecular Dynamics) are incorporated to simulate the particle induced reactions up to 200 GeV/n and the nucleus-nucleus collisions, respectively (Niita et al. 2006; Sato et al. 2006; Sihver et al. 2007). JAM uses a hadronic cascade model, with hadron-hadron cross sections parameterized by resonance and string models by fitting available experimental data (Sihver et al. 2007; Sihver et al. 2008). The Breit-Wigner resonance model and the established data (Particle Data Group 2002) is used at center-of-mass energies less than around 4-5 GeV, at which point the resonances widen and the discrete levels get closer together, and soft processes with little transverse momentum transfer occur (Sihver et al. 2007). Only ionization processes are considered for nuclei transported below energies of 10 MeV/n; above this energy, JQMD is used to transport nuclei (Niita et al. 2006; Sato et al. 2006; Niita et al. 2011). JQMD considers the nucleus to be a self-binding system of nucleons, and can estimate the yields of light particles, fragments and excited residual nuclei (Niita et al. 2006; Sihver et al. 2007). Both JAM and JQMD are used for the dynamic portion of the nuclear reaction. Once the dynamics are finished, the general evaporation model is employed to statistically address nuclear de-excitation through particle emission to obtain the final state of the particle (Niita et al. 2006; Sihver et al. 2007; Sato et al. 2013).

Using the PHITS Code

At the time this work was proposed, the operational version of the NASA developed code HZETRN incorporated approximations that neglected angular dispersion and the effect on lateral beam spread and range straggling which limited its use for simulation of beam line experiments. As a result Monte Carlo transport codes were explored. I chose PHITS for this work primarily due to its reasonable learning curve and ultimately the ease of parallelization of PHITS input. The source code of PHITS is written in FORTRAN, and can be compiled and executed on various operating systems, such as Windows, Mac and Linux. For Windows and Mac, the executable file compiled by Intel Fortran is included in the PHITS package. Thus, the user can execute PHITS in Windows and Mac environments without compiling it. In general for operating in the Linux environment, the user must compile PHITS using the make command coupled with an appropriate Fortran compiler. Although this work was begun with PHITS version 2.13, an event generator for neutron transport was added in version 2.24 and this was used for the completion of this work. While minor changes were made to the code during the years of this work, the physics models in the code were still those of version 2.24 until PHITS was completely rewritten and version 2.52 was released (Sato et al. 2013). Parallelization and operating in the Linux environment became extremely important because the early simulations in the Microsoft Windows environment took from weeks to months to complete. Although PHITS has the capability to incorporate user defined subroutines, these were not required in this work.

PHITS - PARALLEL MODE

For this work PHITS was run on a Linux operating system in parallel mode in order to reduce the computational times to manageable levels. The simulations were performed on the NASA Space Radiation Analysis Group (SRAG) cluster known as Watson. Watson has twenty Advanced Micro Devices, Inc. (AMD) 6176 nodes with 24 processors per node and 32 GB of random access memory per node, and eight AMD 6276 nodes with 32 processors per node and 32 GB of random access memory per node (Langford 2011). The major difference in serial or parallel operation occurs in the compilation of the code, which requires references to different source files and a compiler capable of parallel operations. PHITS was received from Oakridge National Laboratory's Radiation Safety Information Computational Center (RSICC) as a compiled and executable code; however, some modifications to the source files were necessary for it to run properly. The test files provided with the code and other example files obtained through the code developers were run to confirm that installation on Watson was performed correctly.

Although running PHITS in parallel reduced simulation time for this work considerably, experience gained in other work has shown that it is not yet feasible to use PHITS in larger operational evaluations of astronaut dosimetry (Sihver et al. 2010; Bahadori 2013). Simulation of GCR ions in realistic spacecraft geometries or human phantoms can take up to a few days for more than 100 processors. The uncertainty requirements could be relaxed in order to reduce computation time, but for structures larger than the size simulated in the present study, the statistics for a given number of incident particles would be much worse due to a larger simulation volume. Also, it is difficult at present to incorporate complex structures in PHITS due to the relatively simple geometry definitions currently implemented in the code (Sihver et. al. 2010; Bahadori et. al. 2013).

FILE STRUCTURE

The general structure of a PHITS input file is independent of whether the code is run in serial or parallel mode. The user specifies a descriptive phrase for the problem in the "Title" section. Any number of title lines is allowed in the input file. The parameters that govern transport, such as particle energy cut-off and cross-section calculation approach, are selected in the "Parameters" section. The user defines the type, energy, and geometry of irradiation in the "Source" section. Material properties for the materials used in the problem are defined in the "Material" section. The user has the option to choose between the CG system and the GG system when describing the geometry of the calculation. If CG is chosen then the sections "Cell" and "Surface" must be used. However, the "Region" and "Body" sections are used if the CG system is chosen. Finally, values to be recorded in the problem are specified in Tallies, each of which has its own section. An example PHITS input file used to generate data for this chapter is included in Appendix C. Input files created for these studies included the following sections:

- Title,
- Parameters,
- Source,
- Material
- Cell,
- Surface, and
- Tallies.

PARAMETERS SECTION

The values in the "Parameters" section chosen for the present study that affected particle transport and tally recording are shown in the example input files in Appendix C. The "icntl" variable governs the type of PHITS run that is to be executed. Options for this variable include normal execution and geometry checking by voiding all materials and plotting the geometry. Misspecification of the geometry is a common mistake and checking the geometry is important during the development of the simulation input files. Although the default value is 0 for “icntl”, it was included in case input files needed to be debugged. The “maxcas” and “maxbch” variables represent the total number of particles per batch and number of batches, respectively. In parallel execution, the “maxbch” must be divisible by the total number of executable processors, otherwise the simulation will terminate when it reaches the number of batches divisible by the number of processors. The values chosen for these variables eventually balanced run times while achieving acceptable relative error values. Initially the “itall” variable was set to 1 for the simulations in order to record tally output after every batch so that the progress of a particular run could be monitored.

Prior to the use of the code in a parallel multi-processor mode, the ability to check the tally output after every batch was necessary since computational times were lengthy. Once accuracy of the results was determined, the setting was changed to itall=0. The default values for the “incut” and “igcut” variables were chosen to record information on the neutrons and gammas that pass below the minimum energies for transport. The “rseed” value determines the seed number for the pseudo-random number generator included in PHITS. Choosing a value of less than 0 causes the seed number to be chosen based on the computer system clock time, while a value of greater than 0 causes the seed number to be set to that value. The “file” variables indicate locations for input and output files used by PHITS. Here, “file(6)”, “file(7)”, “file(14)” and “file(19)”specify the summary output file, the cross-section library file, and the gamma decay file, and the giant dipole resonance file for photonuclear reactions, respectively.

PHITS was originally developed with the MCNP methodology incorporated for the transport of neutrons. PHITS distribution became restricted through US law in 2009. Receipt and use of the code outside of the US was prohibited. Versions of the code released to US researchers and students through RSICC continued to maintain the ENDF/B-VI cross section library files. Therefore, I used these cross section files in my work. In 2009, the JENDL cross section libraries were continuing to be base-lined against experimental data. This cross section development work has continued and newer releases of PHITS have incorporated JENDL 4.0 (Shibata 2011; Sato et al. 2013). The “emin” variables determine the minimum particle energy required for transport. The code default values are 1.0 MeV for protons, neutrons, pions, muons, and kaons; 2.0 MeV for “exotic” particles; and 10^9 MeV for electrons, positrons and gammas and 10^9 MeV/n for charged particles heavier than protons, which would effectively prevent transport for the particles of interest in this problem. The proton minimum energy was reduced to 1 keV, and the minimum energy for charged particles heavier than protons was reduced to 1 keV/n. The neutron minimum energy was reduced to 10^{-4} eV to include thermal neutrons. Electron and positrons were cut off at 1 MeV to avoid a bug present in PHITS version 2.24 that manifests when electrons and positrons are transported below 1 MeV. This bug was later corrected in the release of PHITS version 2.52 (Sato et al. 2013). Photons were considered to a minimum energy of 1 keV. The maximum energy for cross-section libraries for neutrons was set at 20 MeV, and 1 GeV was used as the maximum energy for cross-section libraries for electrons, positrons, and gammas. The simulations used the default value of 150 MeV for proton transport. For improved results, decay gammas were considered by setting “igamma” equal to 1, and giant dipole resonances were included by setting “ipngdr” equal to 1. The “eqmdnu” and “ejamnu” variables were set to 20 MeV which is the energy above which the JAM model is used to simulate nucleon-nucleus interactions. JAM was chosen as it is generally superior to Bertini in terms of reproducing experimental data (Sato et al. 2013). The “e-mode” variable determines whether the event generator is used during transport. The event generator (Iwamoto et al. 2007; Niita et al. 2011) allows PHITS to sample ions, which is particularly important if one is determining the quality factor for the products of low-energy neutron reactions. Thus, charged particles resulting from neutron interactions were statistically created and the contribution of neutrons to the flux was determined.

Source section

In the "Source" section of the input file, the "s-type" variable defines the type of source used in the PHITS simulation. This variable was set to 2, indicating that a rectangular solid source was predominantly used. For the off-axis proton simulations where a smaller Gaussian shaped beam was simulated, the s-type was set to 13. The available particles for PHITS simulations are listed in Appendix A. These particles can be specified by the symbol or the kf-code as specified by the Particle Data Group (Arguin et al. 2013). The decay-channels and life-times for the particles identified as type 11 are listed in Appendix B. For this work, the projectile chosen was either proton or ^{56}Fe as appropriate to match the experimental beams used. The x, y and z coordinates were chosen to match the dimensions used in the experimental configuration. In early simulations where a source size corresponding to the typical BNL biology beam, 20 cm by 20 cm, was used, however, the computational times for ^{56}Fe simulations were exceedingly long and the use of smaller beam sizes was explored and implemented to reduce the computational times and increase source statistics. The Columbus and REMSIM mock-ups were 6 cm x 6 cm which allowed for a reduction to a 10 cm x 10 cm source size. According to the BNL NSRL website, delivering a dose of 100 cGy to a tissue equivalent (water) samples requires 3.2 x 10^9 protons per square centimeter at a kinetic energy of 1 GeV. If the beam is ^{56}Fe, then 100 cGy is equivalent to 4.7 x 10^6 ^{56}Fe ions per cm^2 at 1000 MeV/n. Typically, 9.5 x 10^6 source particles were chosen for the simulations since this number was determined to be sufficient since the primary particles dominate the statistics and the relative errors reported for the fragments infrequently produced was limited to under 10%.

Materials and Geometry

The materials and geometry of the problem were collectively defined in the "Materials", "Cell", and "Surface" sections of the input file. The geometry described in the PHITS input file was designed to most nearly match the beam line configuration at BNL. The general geometry of the problem included the following components:

- The aluminum vacuum window,
- The local air environment present in the irradiation chamber
- The three parallel plate ionization chambers,
- The rectangular parallel structure representing the shielding material or a cylinder for the angular measurements, consistent with Figures 3.3, 3.4, 3.5, 3.6, and 3.8.
- The aluminum rail system
- The Egg chamber, and
- The particle graveyard, where particles are no longer transported.

In the "Materials" section, each material was given a unique identifier, the nucleus designation, and the percent by mass of each constituent element was defined. Here, the most abundant isotope with the exception of carbon was used to represent each element since data for the natural elements are generally not available in the ENDF VII library (Chadwick 2006). In the "Surface" section, the physical dimensions of the surfaces defining the geometry for each cell were given. In the "Cell" section, each cell is defined by the material number and its density. The universe boundary was defined as ±500 cm in the x dimension, ±500 cm in the y dimension and ±1000 cm in the z dimension enabling the inclusion of a “particle graveyard” to ‘kill” particles leaving these dimensions in order to limit computational times.

Tally sections

PHITS allows the user to specify quantities resulting from simulation to be recorded. These are called tallies, and provide a window into the transport processes of the simulation. Each tally is afforded its own section, in which parameters governing how the tally is executed are defined. PHITS provides two methods, “T-Heat” and “T-Deposit”, for determining the energy deposited. The values calculated by “T-Heat” include the estimated energy deposited using the Kerma approximation. On the other hand, the values calculated by “T-Deposit” include only the energy deposited from charged particles due to their ionization energy loss. “T-Deposit” turned out to be the most appropriate tally in that the absorbed dose values obtained from the Egg chamber measurements were from ionization events. However, “T-Heat” was used in each simulation as a second tally to verify the results. One hundred energy bins between 1 keV and 10 TeV were used, and specific particles of interest were specified. Although the user inputs the energy spectrum in energy per nucleon, PHITS tallies output in terms of absolute energy on a per-source-particle basis. Therefore, appropriate post-processing must be performed to calculate the absorbed dose. After the “T-Heat” tally, “T-Deposit” tallies were used to calculate energy absorbed in the Egg chamber and to determine the particles produced. A conversion was employed to convert to units of absorbed dose. The T-Deposit tally was utilized to determine dose equivalent. PHITs has the ability to determine dose equivalent based on LET in water, LET in a region material or using the Q(L) relationship described by the ICRP. The Q(L) relationship was used in this work.

PHITS Post-Processing

Although PHITS provides a relative error for each tallied result, this value represents the error associated with the mean of the tally for a single random number. To gain a true representation of the uncertainty in a tally, PHITS must be executed multiple times and the standard error of the mean should be calculated. PHITS was executed four times for each simulation to characterize the standard error of the mean for each tallied quantity. Since a large number of particles, (9.5×10^6) were transported for each simulation, the relative error for each total tallied quantity was on the order 0.1%. To obtain the uncertainty in a tally, the tally output files for the four runs in each simulation were post-processed using statistical functions available in Microsoft Excel.

Chapter 4: Physical Measurement Results

^{56}Fe Beam Results

Columbus and REMSIM Results

In order to compare the shielding effectiveness of the spacecraft mock-ups to standard spacecraft materials, absorbed dose measurements were also taken for aluminum and polyethylene with areal densities of 3.5 g/cm^2, 7 g/cm^2, and 15 g/cm^2 each. Since only a single dose measurement was taken for each of the shielding mock-up, a beam dose of 200 cGy was delivered to reduce uncertainty in the dose measurement. The results of the tests with the ^{56}Fe ions are graphed in Figure 4.1. In general the materials tested showed a decrease in dose reduction ability with decreasing areal density. In addition, data show that as expected, 15 g/cm^2 of polyethylene had the greatest reduction in absorbed dose. However, for the same 15 g/cm^2 areal density, the Columbus with internal structure model provided a greater reduction in dose than for aluminum alone. The dose reduction increased from 8.2% to 28.7% when the internal structures materials were added to the Columbus shell. The addition of Kevlar® as a composite material to represent the plastic and other composite materials contained throughout the modules is responsible for this reduction. Kevlar® and is superior to aluminum in reducing absorbed dose due to a shift along the LET curve to a lower value (Lobascio et al. 2008; Silvestri et al. 2011). Structural materials and equipment in the vehicle should be included in astronaut risk assessments to provide a more accurate assessment of the shielding provided. Although the REMSIM configuration with water had a lower areal density, it provided a comparable reduction in dose to the Columbus with internal structure model demonstrating the effectiveness of water in reducing dose. From these results, it appears that a prudent approach would be to develop design solutions for inflatable habitats that include water tanks placed behind the pressurized vehicle walls. The Columbus and REMSIM configurations alone did not provide the shielding effectiveness of the other configurations. Given the small areal densities of these mock-ups, this was suspected.

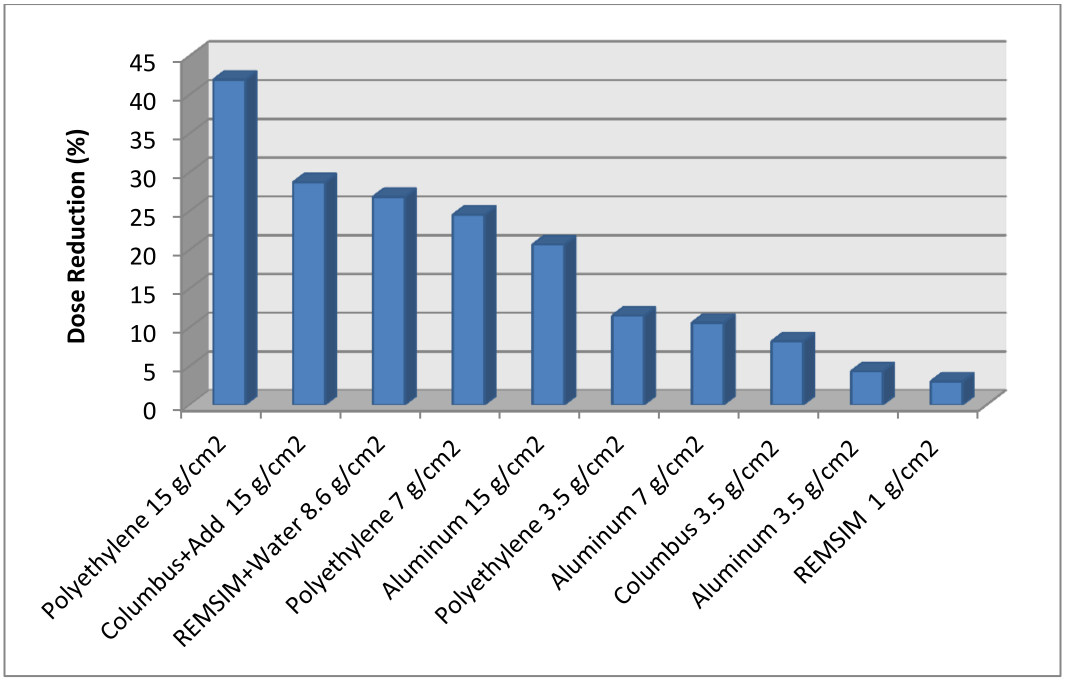

Figure 4.1: Absorbed dose reduction versus shielding configuration for 964.9 MeV/n ^{56}Fe beams when compared to a reference dose. Adapted from (Silvestri et al. 2011).

Aluminum and Polyethylene Order Results

As shown in Figure 4.2, the ^{56}Fe ion irradiation of the four configurations of polyethylene and aluminum with mutually changing positions, the general behavior appears to be the same for equivalent areal densities. The reduction in dose for configuration with 5 g/cm^2 polyethylene and 5 g/cm^2 aluminum is similar to the configuration in which the order changes. The same situation is replicated for the configurations where the areal density is increased to 10 g/cm^2 polyethylene and 10 g/cm^2 aluminum. In this case the configuration with polyethylene before aluminum presents a slightly larger reduction in absorbed dose with respect to the configuration with aluminum before polyethylene. However, this finding could be attributed to statistical fluctuations in the measurements since the reduction percentages were close in value. When comparing dose reduction capability of these multi-layer results to the materials tested in Figure 4.1, I find that 15 g/cm^2 of polyethylene was still more effective at reducing dose confirming the earlier findings (Wilson et al. 1995; Shavers et al. 2004; Guetersloh et al. 2006). When the polyethylene and aluminum combinations are compared to the results obtained for the other shielding configurations, the reduction in dose combination of materials provided reduction in dose more nearly matches those configurations with consistent areal densities.

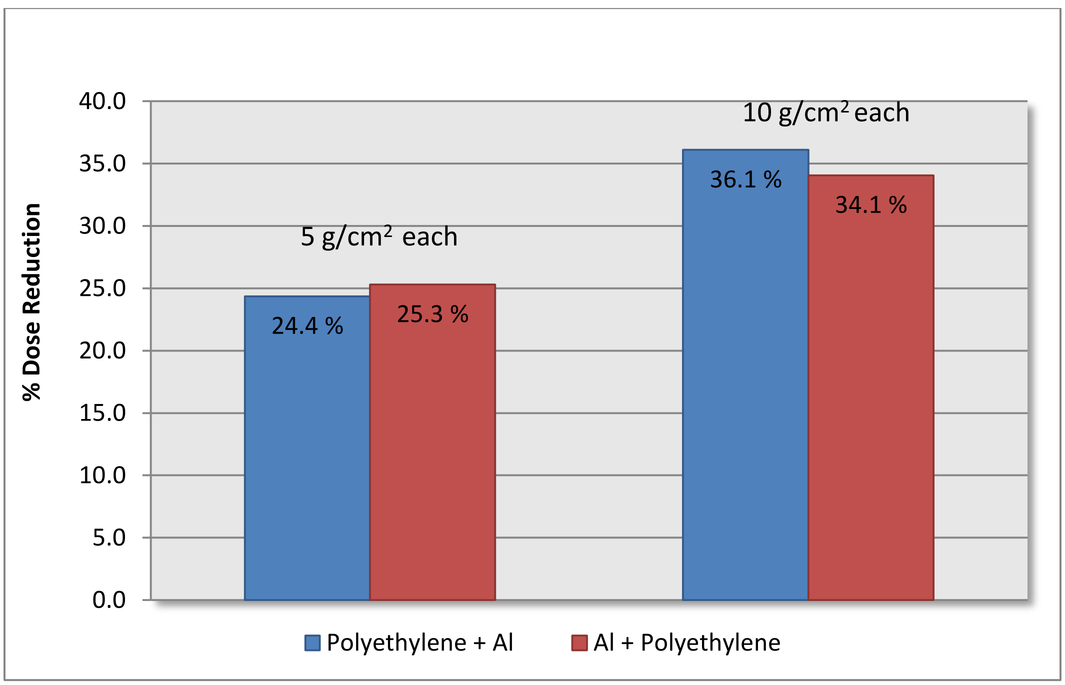

Figure 4.2: Reduction in absorbed dose for Al-Polyethylene and Polyethylene-Al with increasing thickness for 964.9 MeV/n ^{56}Fe beams when compared to a reference dose.

The dose reduction between experiments of different thick target depths can be compared by determining the fractional dose reduction divided by the areal density of the target using equation 4.1(Zeitlin et al. 2006).

$$\delta D_n = \frac{1}{\rho x}\left[\frac{D(x)-D_0}{D_O}\right] \qquad \text{Eqn. 4.1}$$

where ρ is the density of the target material, x is its depth, D(x) is the dose at the shielding depth and D_0 is the dose without the shielding (Gutersloh et al. 2006; Zeitlin et al. 2006). This simple method provides an approximation of shielding effectiveness but allows a more complete comparison of dose reduction across different materials and thicknesses.

The calculated dose reduction values for the materials in this study are relatively small as shown in Figure 4.3. The range in mass numbers for the shielding materials used here is small limiting the ability to drawn broader conclusions as in Zeitlin et al. (2006). For these materials it is not clear that shielding effectiveness decreases as the mass number of the material or combination of materials increases. Thin shields of polyethylene are still the most effective at reducing dose while all three thickness of aluminum are the least effective. However, both of the REMSIM mock-ups were nearly as effective as the thin targets of polyethylene and more effective than the 15 g/cm^2 one indicating that the radiation protection provided by inflatable structures should be further evaluated. When comparing layering of polyethylene and aluminum, the data suggest that dose reduction superior to either of the Columbus mock-ups and aluminum alone is present for the both of the 10 g/cm^2 layers. However, the effect is not present with the doubling of the thickness. This same decrease in dose reduction is present when the thickness is increased for the aluminum and polyethylene shields.

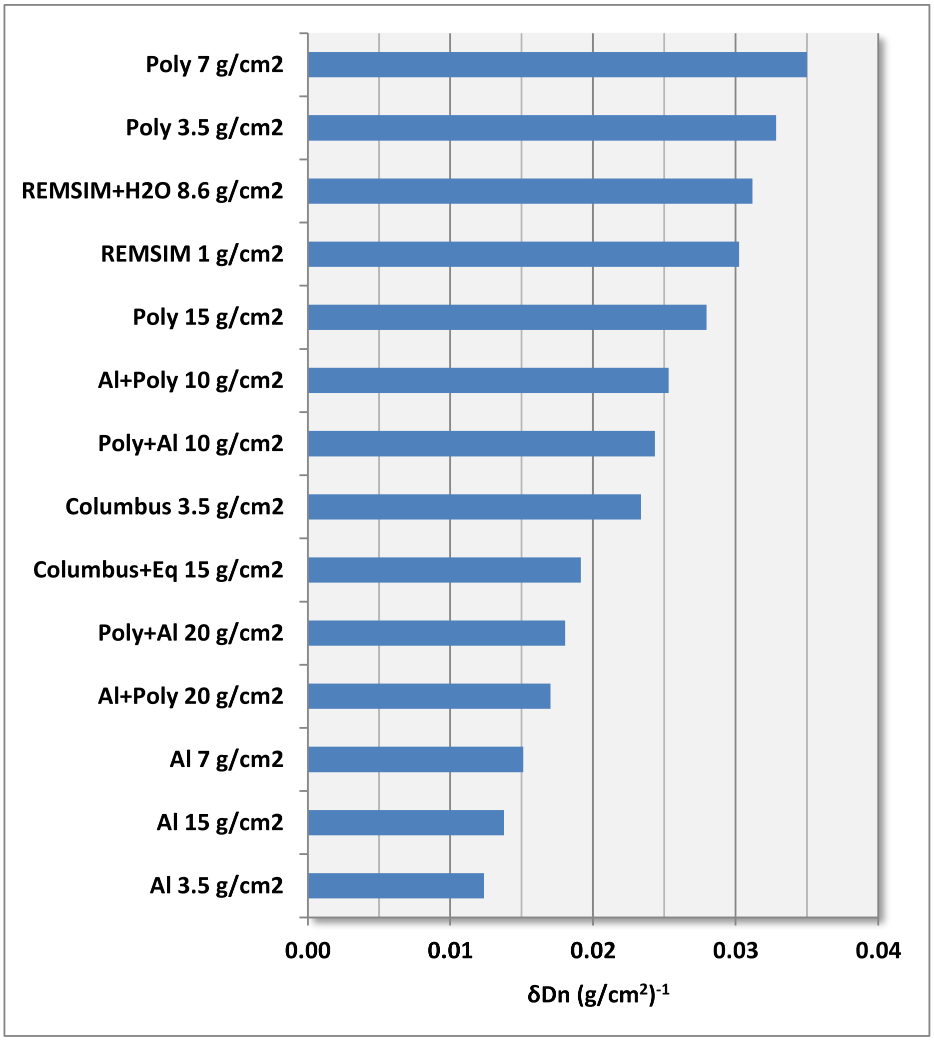

Figure 4.3: Dose reduction normalized to areal density ranked from highest to lowest for shielding materials irradiated with a 964.9 MeV/n ^{56}Fe beam.

Lower mass materials are known to be advantageous for shielding neutrons through the reduction in target-evaporation neutrons, which are predominately low energy (< 20 MeV) neutrons with high biological weighting factors (Cucinotta 1993). Finally, there is a narrow range in performance across all the materials used in this study leading me to conclude that a decision as to which configuration would be the optimal shielding design is not straightforward. Design engineers could select the vehicle construction materials based on properties important in human spaceflight.

Proton Beam Results

Columbus Results

Dose measurements were obtained with the Egg Chamber in 2 cm increments from 80 cm in front of the shielding mock-up to 80 cm behind the shielding mock-up along the 1 GeV proton beam axis. An additional measurement was taken at 1 cm to obtain greater detail on the absorbed dose behavior close to the shield. Data plotted in Figure 4.3, normalized to the dose delivered in the unshielded configuration, show the percent dose reduction as a function of the distance for the Columbus plus internal equipment mock-up. The absorbed dose at the first detector position, 0.254 cm, increased about 25% when the beam was shielded, remained elevated for the first 2 cm and then decreased to about 80% of the total absorbed dose at a distance of 80 cm from the shielding mock-up. This decrease is likely due to shielding of the light fragments produced, low energy protons, pions, muons, and electrons, by the intervening air thickness (Mancusi et al. 2007). Given that the depth in a typical rack on the ISS is 107 cm, one can reasonably assume the dose to the astronaut would be reduced at least this amount. The data appear to indicate that a further reduction in absorbed dose could be possible at 107 cm. Physical space limitations prevented obtaining dose measurements at the distances consistent with an ISS rack. Figure 4.4 also shows a 4% increase of the absorbed dose for the first centimeter before the shielding configuration. This result is due to the production of secondary particles in the Columbus mock-up materials and similar to that shown in similar experiments (Mancusi et al. 2007; Destefanis et al. 2008; Silvestri et al. 2011).

REMSIM Results

For the tests of the REMSIM configuration, dose measurements were obtained identically to those for Columbus. Figure 4.4 shows the amount of absorbed dose delivered as a function of the distance along the 1 GeV proton beam axis for the REMSIM shield. Similar to the Columbus measurements, the absorbed dose at the sample position increased 24% when the beam is shielded with the REMSIM shielding configuration, while it decreases to about 88% of the irradiated absorbed dose at a distance of 30 inches from the sample. Again, given that the depth in a typical rack is 107 cm and some sort of rack structure will be necessary in inflatable habitats, one can reasonably assume the dose to the astronaut would be reduced the same 12%. Figure 4.4 shows a similar increase in the absorbed dose immediately before the sample, up to 2 inches, due to the production of secondary particles. The shielding properties of REMSIM mock-up are very similar to that of the Columbus mock-up as Figure 4.3 shows. This is interesting in that the areal densities are quite different but illustrative of the improvement in dose reduction when water is incorporated into the shielding. As a reminder, REMSIM plus water mock-up has an areal density of 8.6 g/cm^2 while the Columbus plus internal structure mock-up has an areal density of 15 g/cm^2.

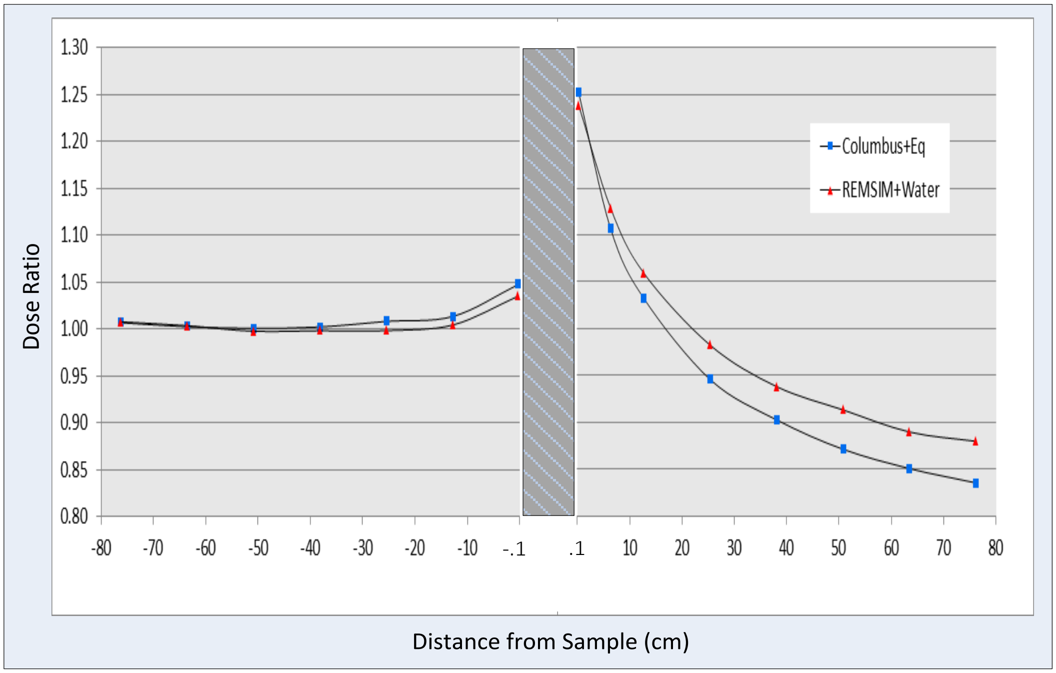

Figure 4.4: Absorbed dose measured at varying distances along the 1 GeV proton beam axis for the Columbus plus internal equipment equivalent mock-up (blue) and REMSIM plus water mock-up (red). Adapted from (Destefanis et al. 2008). Lines are used to connect the points.

Aluminum and Polyethylene Comparison Results

The evaluation of the degree of absorbed dose reduction produced by both the Columbus configuration and the REMSIM configuration when compared to measurements taken with aluminum and polyethylene with areal densities of 7 g/cm^2 and 15 g/cm^2 is illustrated in Figure 4.5. In this portion of the experiment, measurements at a distance of 0.254 cm behind the shielding material were obtained for aluminum and polyethylene consequently the results reflected in Figure 4.5 are for only this distance. The Columbus plus internal equipment mock-up provided a larger dose reduction than a pure aluminum thickness of the same areal density; however, the Columbus plus internal structures mock-up did not reduce the absorbed dose as much as 15 g/cm^2 polyethylene thickness. The reduction in dose obtained from the REMSIM plus water mock-up was measured to be the same as that for $7 g/cm^2$ of polyethylene. Similar to other results our team obtained, an increase in absorbed dose was seen for all four of the configurations tested and the increase was greatest for both areal densities of aluminum(Mancusi et al. 2007). The increase was nearly 43 % for the $7 g/cm^2$ areal density and 60% for the $15 g/cm^2$ areal density. The fact that the tested multilayer "Columbus" mock-up provided a larger dose reduction than a pure aluminum mock-up of the same areal density, lead our team to observe that, if mass savings were required while balancing radiation protection properties, selection of a lighter composite wall with the same dose reduction factor would be a prudent approach.

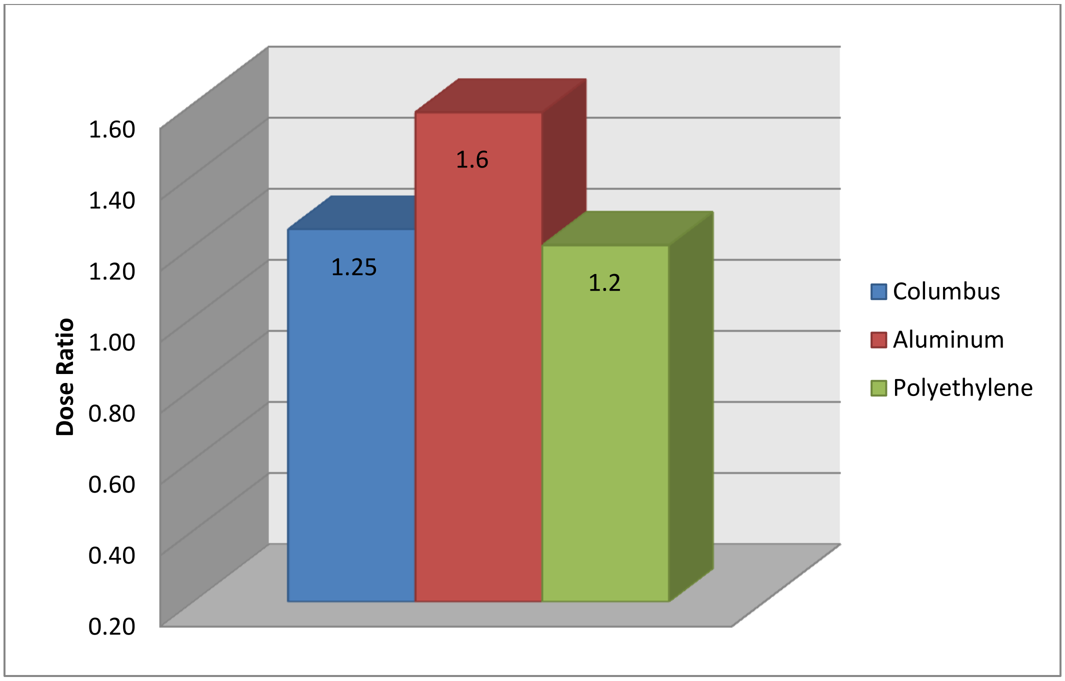

(a)

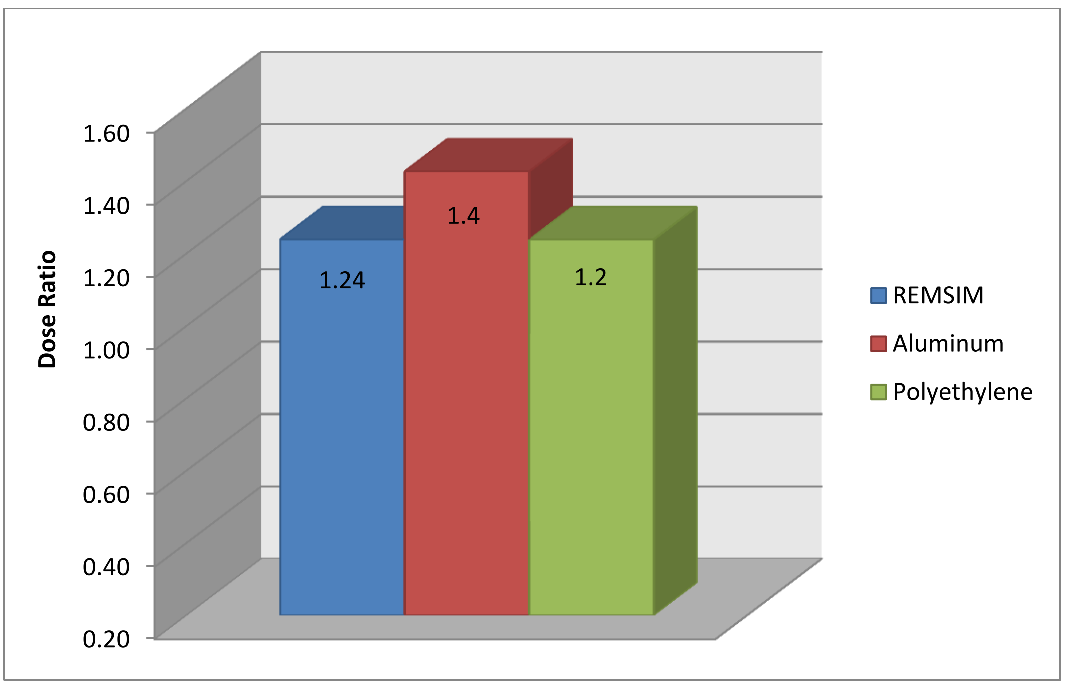

(b)

Figure 4.5: Dose ratio comparisons for (a) Columbus and (b) REMSIM mock-ups to aluminum and polyethylene blocks with similar areal densities for a 1 GeV proton beam.

Aluminum and Polyethylene Shielding Results

Aluminum and polyethylene shields obtained by changing their mutual position and increasing the areal density of the material are used to reduce the proton beam. These configurations more nearly match the inputs, semi-infinite slabs of aluminum and water, to the NASA operational astronaut radiation dose assessment process using HZETRN (Cucinotta et al. 2012; Semones 2012). The delivered absorbed dose was measured at increasing distance (0.254 cm to 5.08 cm) from the samples by means of the Egg Chamber. Figure 4.6 shows that all four configurations result in an increase in dose directly adjacent to the shielding configuration like in the previous measurements. The increase ranges from 25-63% and is greatest for the 10 g/cm^2 polyethylene followed by 10 g/cm^2 aluminum. Interestingly this same 60+% increase was seen it the measurements for the 7 g/cm^2 of aluminum. The absorbed dose decreases with increasing distance from the shielding material. When comparing to all experimental values obtained in Figure 4.7, the increase is greater than that measured previously for either of the Columbus or REMSIM mock-ups. Measurements were not taken to determine whether the decrease would coincide with realistic vehicle measurements but it seems reasonable that the light particles produced would be decrease in a manner similar to that seen in the Columbus and REMSIM experiments.

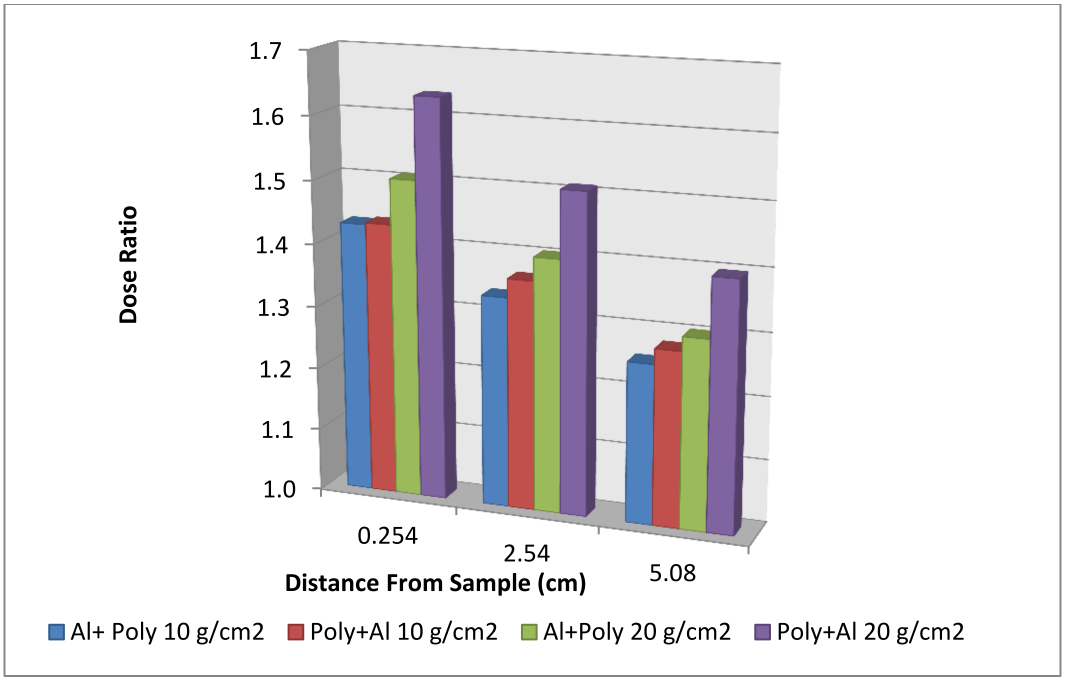

Figure 4.6: Absorbed dose ratio for a 1 GeV proton beam after different aluminum and polyethylene configurations when compared to a reference dose. Adapted from (Destefanis et al. 2008).

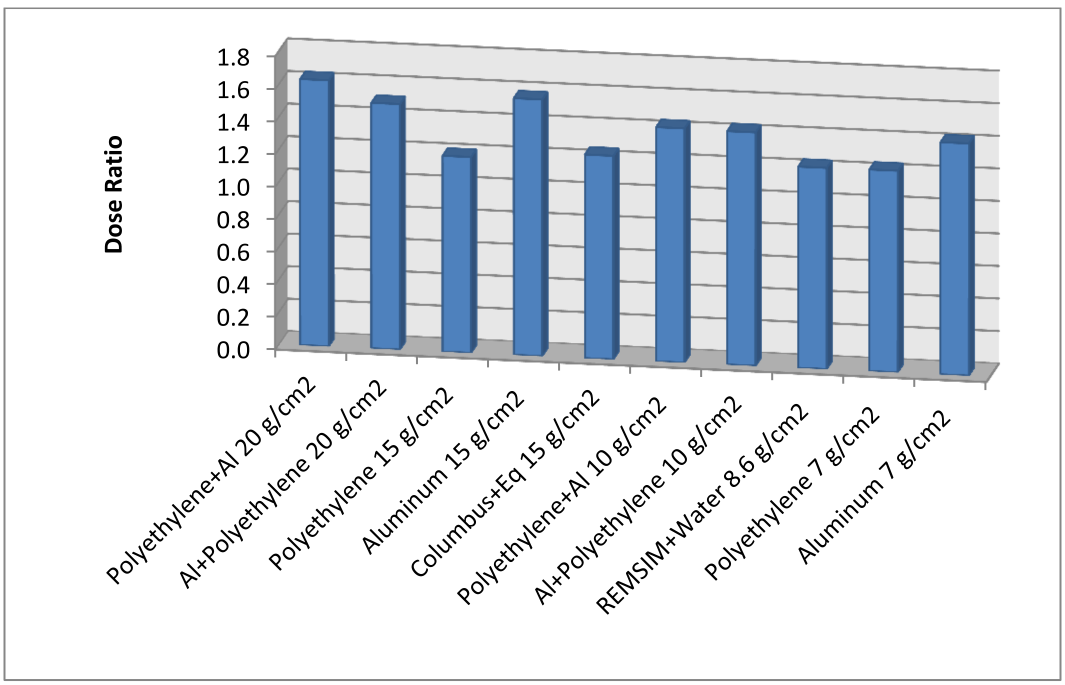

Figure 4.7: Absorbed dose ratio versus shielding configuration for 1 GeV proton beams when compared to a reference dose.

Angular Distribution of Protons

A limitation in the measurements and results described in the previous sections is that these measurements were obtained along the beam axis neglecting any contribution to lateral spreading. Expanding upon this work and that published in Bertucci et al. (2007) and Mancusi et al. (2007) the angular distribution of the secondary protons and other low LET particles produced by the high energy protons irradiating an aluminum cylinder of 2.71 g/cm^3 with dimensions 30x30 mm, positioned with the axis parallel to the beam were obtained. The location of the egg chamber was varied between 0 and 6 cm on the x dimension; the y dimension was 0 cm; and therefore a constant z dimension of 1 cm from the cylinder to evaluate the angular distribution of the secondary protons. Dose measurements are described in Table 4.1. The majority of the particles, primary and secondary are produced in the forward direction and lateral dose decreases rapidly with increasing angle from the z-axis.

Run #	Beam Dose (cGy)	Egg Dose (cGy)	Egg Dose /Beam Dose	Dose Rate (cGy/min)	Egg Position (cm)	Exposure Time (min)
1	200.14	187	0.934346	196.25	(0, 0, +1)	1.12 min
2	14.27	13.33	0.9341275	111.46	(0, 0, +1)	0.20 min
Total		200.33				
3	2500	32.9	0.01316	2569.32	(-2, 0,+1)	1.12 min
4	13125	173.02	0.0131825	4993.32	(-2, 0, +1)	2.91min
Total		205.92				
5	10000	48.04	0.004804	6060.52	(-4, 0, +1)	1.85 min
6	31600	152.05	0.0048117	7015.36	(-4, 0, +1)	4.96 min
Total		200.09				
7	40000	103.81	0.0025953	6996.07	(-6, 0, +1)	6.28 min
8	37000	101.84	0.0027524	7071.24	(-6, 0, +1)	5.75 min
Total		205.65				

Table 4.1: Angular dose measurements for a 1 GeV proton beam shielded with 8.13 g/cm^2 aluminum cylinder.

Beam Images

The NSRL beam profile can be tuned to a variety of shapes and sizes. Gathering data on the beam shape and size was necessary for informing the type of source input for the PHITS simulations. For all of the experiments except the off-axis measurements of protons, a square beam of either 10x10 cm^2 or 20x20 cm^2 was used. An image of a 10x10 cm^2 ^{56}Fe beam profile captured with the NSRL Digital Beam Imager is illustrated in Figure 4.8. The shielding material and the Egg Chamber are visible in the image and there is uniform beam intensity across the exposure area confirming the choice of a rectangular solid source for PHITS. For the off-axis measurements a small beam spot was required. The beam image for the 980 MeV proton beam shown in Figure 4.9 indicates that a Gaussian shaped beam was used. The beam size was estimated to be 1.79 cm through an examination of the photographic emulsion of the beam image.

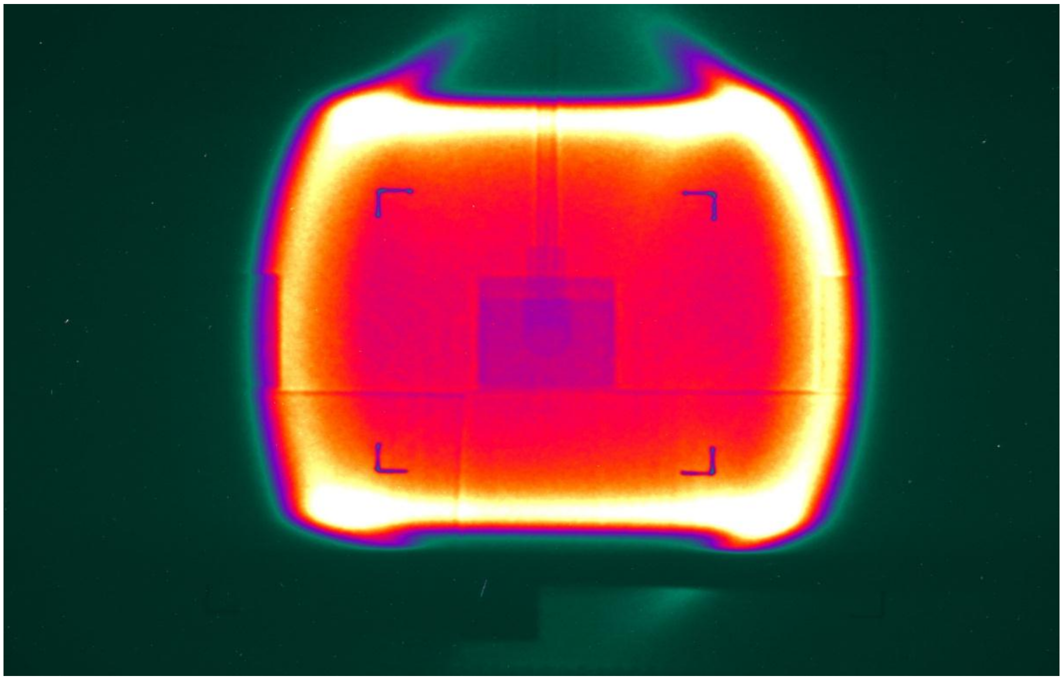

Figure 4.8: NSRL beam image of 10 x 10 cm^2 ^{56}Fe beam.

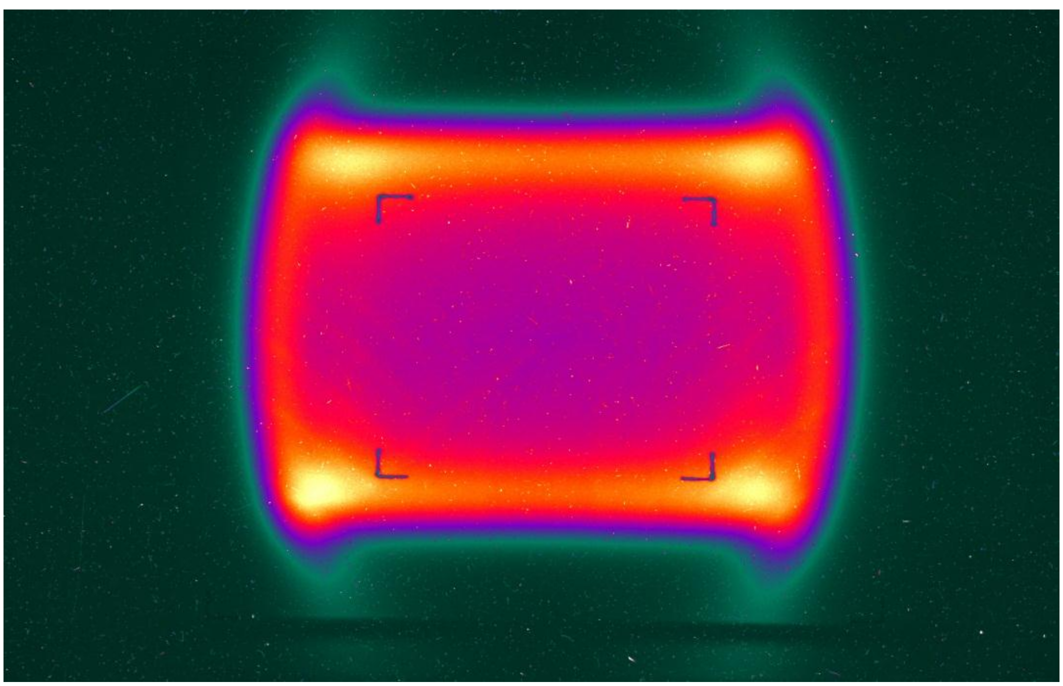

Figure 4.9: NSRL beam image indicating a Gaussian shaped beam for 1 GeV proton.

Chapter 5: PHITS results

Simulations of the Energy Deposited in the Ionization Chamber

Due to the limited acceptance of the beam transport, it is assumed that only a single species of ion is transported to the target. Any fragmentation observed takes place in the material in the beam line described earlier in Chapter 4.24. Each parallel plate ion chamber is composed of 5 mils (0.018 g/cm^2) kapton, 68 μm (0.061 g/cm^2) Copper, 0.040 μm (0.077 mg/cm^2) gold, and 4 cm of Nitrogen gas. These ion chambers were simulated in the PHITS input file as individual layers with dimensions of 20 cm x 20 cm. This approximation limited the geometry errors experienced while running PHITS. The Egg chamber was simulated as a 1 cm^3 sphere of air and although labelled as the Egg chamber there is no solution of continuity with the surrounding medium which is also air. An understanding of the energy deposition in the ion chamber was important to understand the baseline particle interactions and deposition without the shielding material in place. Therefore, interactions and particle production due to the six meters of air and the three parallel plate ion chambers between the vacuum window and the Egg chamber can be treated as background when evaluating the other experimental geometries. The energy absorbed in the Egg chamber was simulated for the 964.9 MeV/n ^{56}Fe beam and the 1 GeV proton beam. The results are shown in Figures 5.1 and 5.2 and are a good visual representation of the distribution of the loss of energy in the primary particle and fragmentation distribution in fluence, energy and particle produced. The primary particles dominate the contributions to the absorbed dose while the secondary particles are in general 2-3 orders of magnitude lower in number. For the ^{56}Fe beam simulations, several peaks are seen; one in the energy bin containing the 964.9 MeV/n beam energy; one in the range of 1-4 MeV for the lighter ions, charge less than five. The same peak is present for the pions, muons, and electrons and a peak 2-3 orders of magnitude lower in the energy bin range 100-1000 MeV for the heavier ions is observed. For the proton beam simulation the distributions peak in the range 1-4 MeV since low energy protons, pions, muons and electrons contribute to absorbed dose.

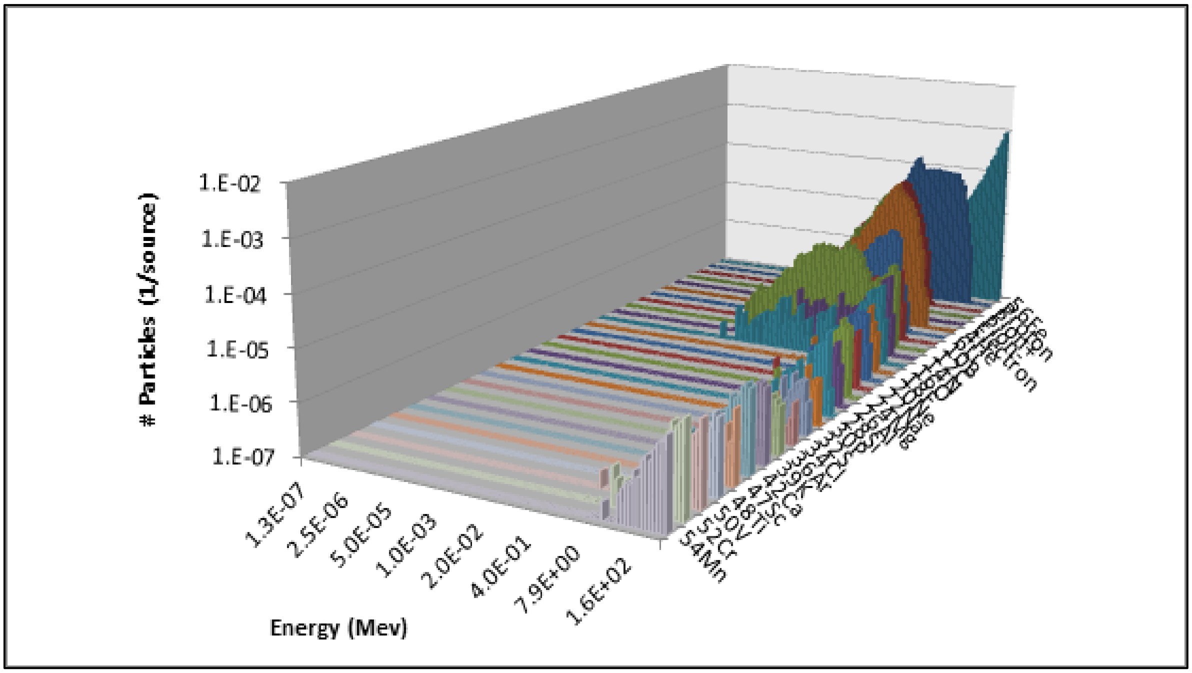

Figure 5.1: Contribution of particles in energy and number to the absorbed dose in the Egg chamber in PHITS simulation of 964.9 MeV/n ^{56}Fe beam.

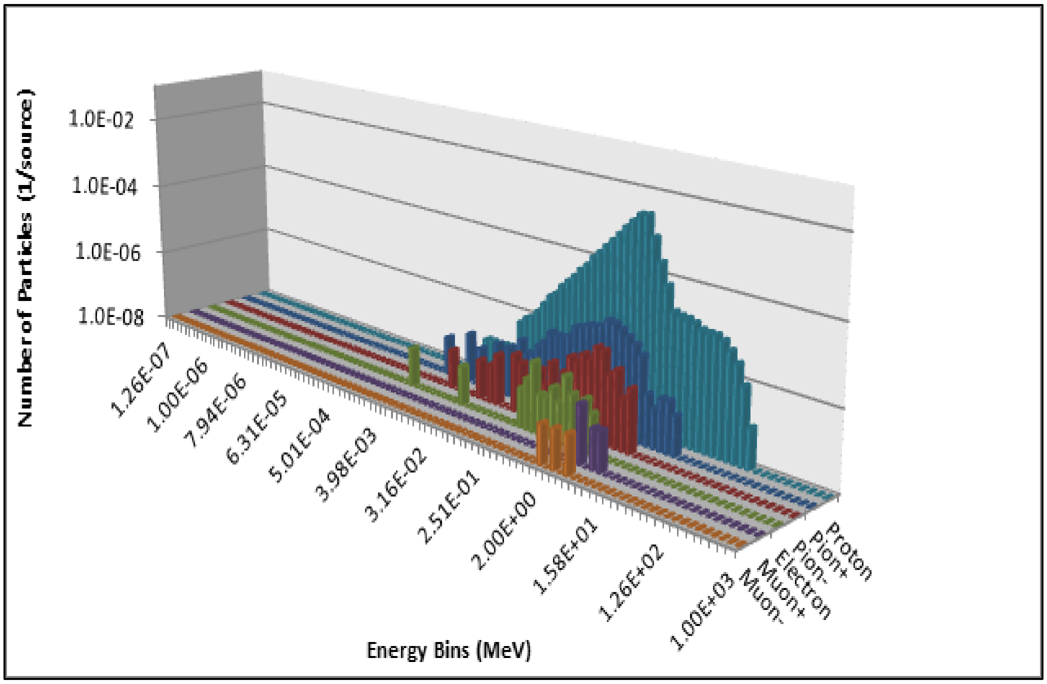

Figure 5.2: Contribution of particles in energy and number to the absorbed dose in the Egg chamber in PHITS simulation of 1 GeV proton beam.

SIMULATIONS OF BRAGG CURVE

In order to ensure the use of an appropriate physics model for all simulations, a Bragg curve for the 964.9 MeV/n ^{56}Fe beam was simulated using an input file that described an experimental geometry that included all components and dimensions of the BNL beam line. Figure 5.3 is a schematic of the beam line components used in the simulation. For improved accuracy the rail system was added to the geometry of the simulation. An input file was created for each thickness of polyethylene and run. The relative dose was calculated by the ratio of the dose in the detector after range shifter to the dose in the detector placed before the range shifter. Figure 5.4 shows the comparison of the PHITS simulation to the experimental results. While the values around the Bragg peak vary greatly on an individual thickness basis, the overall shape of the curves compare very nicely indicating appropriate choices in the PHITS parameters governing transport. This beam line geometry was incorporated in the remaining shielding simulations.

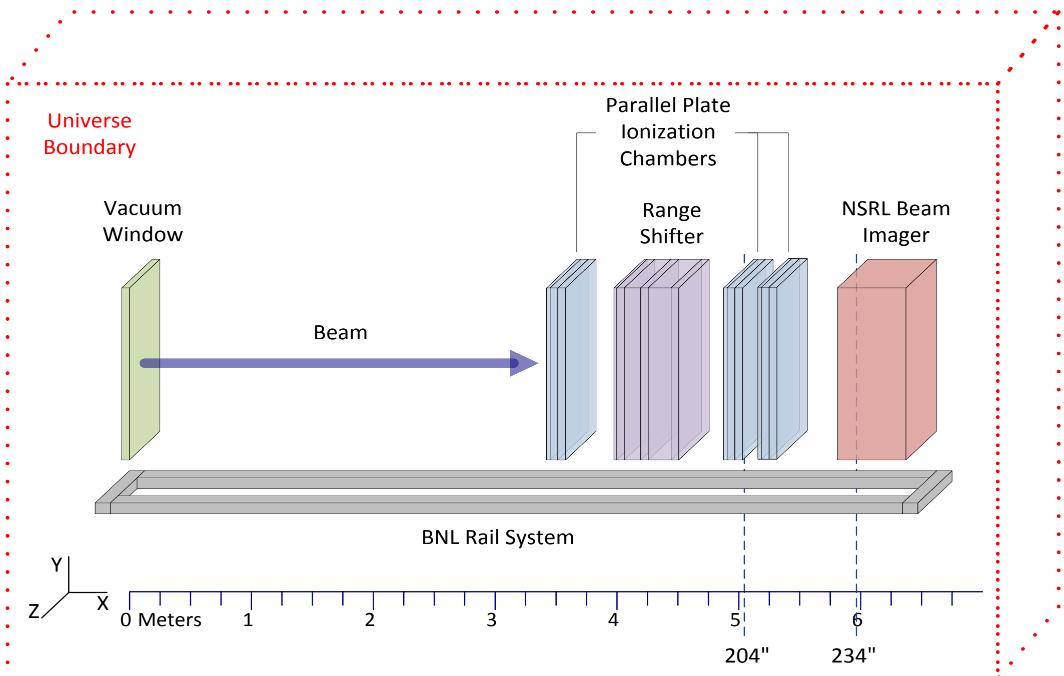

Figure 5.3: Geometry representation in PHITS for the NSRL target room.

During the course of this work, NASA's Space Radiation Health Program developed a Monte-Carlo based transport code, the GCR Event-based Risk Model (GERMCode) leveraging the many Bragg curve measurements for various nuclei taken by BNL staff. The GERMCode uses the quantum multiple scattering fragmentation model (QMSFRG) nuclear database combined with the range energy subroutines from HZETRN to describe the NSRL beam line(Cucinotta et al. 2011). The GERMCode has been heavily validated with NSRL measurements and the measurements described in Zeitlin et al. 2008 (Cucinotta et al. 2012). Similar to the PHITS simulations presented in this dissertation, the GERMCode uses a monoenergetic flux normalized to 100 cGy. Using version 1.1 published in 2011 obtained from the NASA Space Radiation Health Project, a Bragg curve was generated as a further validation of my PHITS models. Figure 5.4 also shows the same similar agreement in curve shape; however, a small difference in prediction by GERM is seen at low energies at the peak. This difference can be explained by differences in transport between the two codes resulting from the NSRL beam line approximation, beam energy shift at NSRL, interpolation and extrapolation in the fragmentation database, numerical result obtained due to the shielding depth interval for beam transport. Using the GERMCode to model the Bragg curve gave insight after the fact on comparison between HZETRN results and PHITS. The process developed with PHITS is lengthy while a Bragg curve can be obtained with GERMCode in a matter of minutes. GERMCode does not provide ion species identification in the primaries and secondaries. If identification of the particle and its contribution to the dose is important, detailed simulations similar to my work with PHITS is preferred.

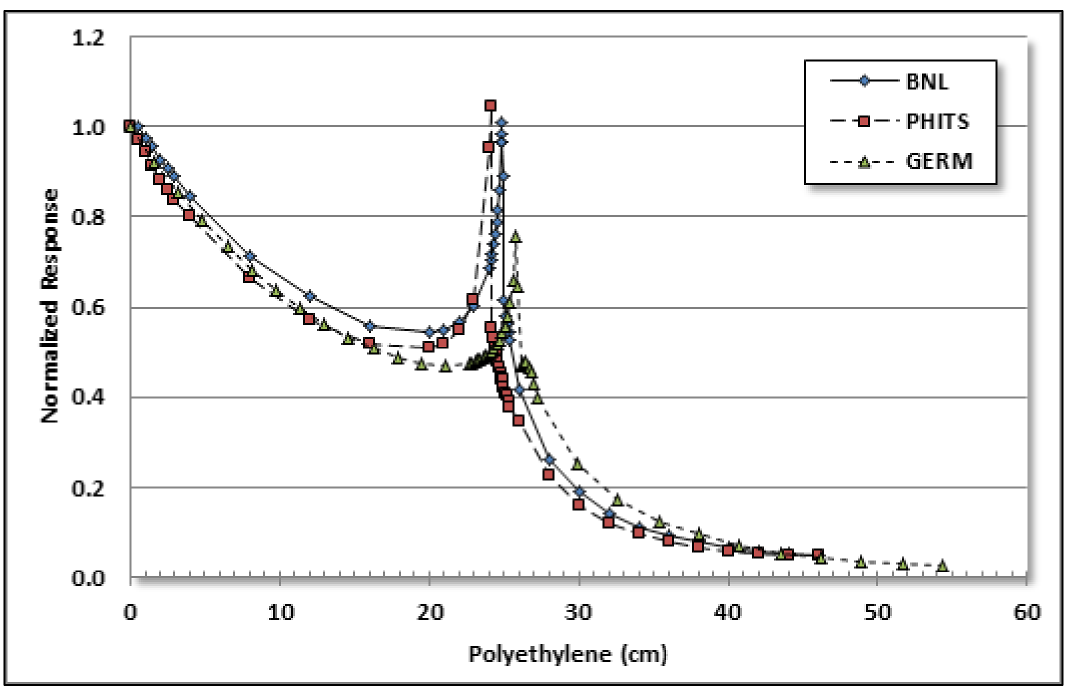

Figure 5.4: Comparison of experimental Bragg peak measurements to simulated Bragg peak for a 964.9 MeV/n ^{56}Fe beam. Lines are used to connect the points.

SIMULATIONS OF EXPERIMENTAL DATA FOR ^{56}FE IONS

The experimental geometries from Chapter 3 were developed in PHITS and incorporated in the general experimental geometry shown in Figure 5.3. The geometry of the Columbus mock-up shown in Figures 3.3 and 3.4 with dimensions described in Tables 3.3 and 3.4 were developed. These geometries were composed of rectangular parallel planes of the Columbus layers (aluminum, Nextel®, Kevlar®, multilayer insulation and aluminum), aluminum rack structure, and Kevlar) placed adjacent to one another. A similar geometry development process was used for the REMSIM and REMSIM plus water mock-ups using the layered geometry described in Table 3.5 and illustrated in Figure3.5. The aluminum and polyethylene plates were modelled as rectangular parallel planes of appropriate areal density (3 g/cm^2, 7 g/cm^2, and 15 g/cm^2) and dimensions reported in Table3.1. A monoenergetic input spectrum of 964.9 MeV/n ^{56}Fe ions was used and the dose was normalized to the simulated dose value at the first measurement of the Egg with shielding material removed. Figure 5.5 shows the comparison of the measured absorbed dose in the Egg Chamber to the PHITS results. Measured versus calculated differ by up to ±10% showing good agreement confirming that the physics used in the simulations are likely correct. Similar observations to the experimental results regarding dose reduction capabilities of the materials were obtained; the 15 g/cm^2 polyethylene slab provided the largest dose reduction while REMSIM provided the least. The simulations also confirmed that the Columbus plus internal structures mock-up reduced the dose more than an equivalent areal density of aluminum. It is interesting to note that for the shielding materials composed of aluminum, PHITS tends to over predict the experimental results by as much as 10%. When evaluating the proton results discussed later in this dissertation, this same over prediction is not seen. Uncertainties in the nuclear physics models within PHITS coupled with gaps in the measured cross sections are the likely reasons.

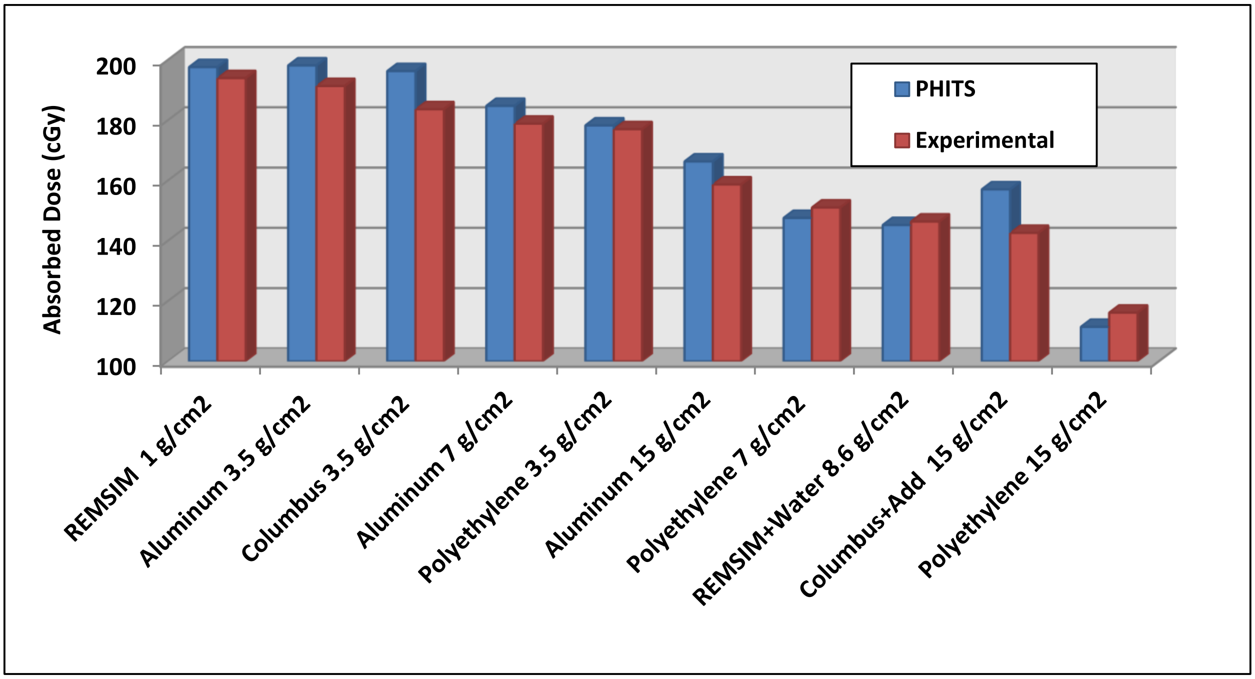

Figure 5.5: Comparison of the average dose calculated by PHITS simulations of the 964.9 MeV/n ^{56}Fe beam to the experimental results.

^{56}Fe Beam Fragmentation Results

The nuclear fragmentation events occurring as a result of particle interactions with the shielding material play a role in determining the effectiveness of a particular shielding material. The fragmentation distribution after each shielding material was determined by scoring the PHITS output using the T-Deposit (energy deposited in a volume) tally for the Egg Chamber. Using the output from the T-Deposit tally was convenient in that those results were already post processed from the dose calculations earlier and did not require re-simulation of the experiments. This method was previously described in Zeitlin et al. (2010). A limitation in this approach is the geometry issues inherent with modelling a small detector volume. The results are shown in Figures 5.6 – 5.8 and show some expected general results (Zeitlin et al. 2008). The fragmentation distribution favors the production of particles with an even charge; the odd-even effect and show a decrease in fragment production until charge ten. Below charge nine, a steady increase is seen in the fluence. The magnitude of the increase in the production of oxygen is unexpected but is in reasonable agreement with previously reported increase for oxygen through carbon with a decrease at beryllium in simulations of the same experimental data with Geant4 using the G4BinaryIonCascade model (Silvestri et al. 2011). Figure 5.6 shows the 964.9 MeV/n ^{56}Fe ion fragmentation induced by the three materials of areal density 3.5 g/cm^2 tested experimentally. Results are normalized to the simulated source and displayed in several graphs to illustrate the fragment production differences. Differently than reported in Silvestri et al. (2011), the PHITS simulations show that the Columbus hull mock-up induces a similar fragmentation distribution to an equivalent areal density of aluminum. The polyethylene target leads to more abundant production of fragments with Z>12 due to the light materials while the spectrum of fragments are more nearly equal for Z<12. A similar result shown in Figure 5.7 is seen when the fragmentation distributions are compared between the Columbus plus internal structures mock-up and equivalent areal densities of aluminum and polyethylene. PHITS is thought to systematically under estimate charge changing cross sections especially for light ions which could explain this differences in the results here and in Silvestri et al. (2011) (Sihver et al. 2007; Sihver et al. 2008; Zeitlin et al. 2008). However it is important to note that while fragment cross sections predicted by PHITS have been shown to not be in good agreement with experimental data, PHITS does correctly predict the trends Zeitlin et al. (2008). Figure 5.8 compares the fragments produced from the Columbus hull and Columbus plus internal structures mock-up. As expected the Columbus plus internal structures mock-up produces more fragments due to the higher areal density and addition of Kevlar®. Finally, it is interesting to note that the heaviest fragments are not increased for the Columbus plus internal structures mock-up when compared to the Columbus hull mock-up. The additional thickness provides the opportunity for these fragments to further fragment into lighter ions. The underestimation of the fragmentation events by PHITS reported in Zeitlin et al. (2008) may also be responsible for this result.

To evaluate the production of fragments from the REMSIM mock-ups, the results were compared to the aluminum and polyethylene with areal densities of 7 g/cm^2 as these most nearly matched in areal density the REMSIM plus was mock-up. This comparison is reported in Figure 5.9. For moderate to heavy fragments, Z>8, the REMSIM plus water mock-up fragmentation spectrum closely matches the spectrum for the 7 g/cm^2. The fragmentation occurring in the aluminum shield is less. The presence of water which is hydrogen rich in both water and polyethylene increases the fragments produced with little spectrum change. Comparing the fragmentation results for the Columbus and REMSIM mock-ups is shown in Figure 5.10. This comparison provides the opportunity to evaluate the potential radiation protection capabilities between a currently flying vehicle configuration to a structure type still in the planning and design phases. Interestingly the spectrums reported for the Columbus plus internal structure mock-up is nearly identical to the spectrum for the REMSIM plus water and a similar finding to that found with the Geant4 simulations in Silvestri et al. (2011). Recall that the physical measurements for both mock-ups reported in Figure 4.1 provided a similar dose reduction capability, 26-28%. Therefore the radiation protection provided by both structures is nearly the same for 964.9 MeV/n ^{56}Fe ions, however, the areal density of REMSIM is approximately half that of the Columbus plus internal structures mock-up. Since inflatable habitats are still in the planning and design phase and rack structures are unknown for this vehicle type, we did not include the any thickness to approximate the equipment racks. It is reasonable to infer that additional radiation protection would be provided by the mass from the rack structure.

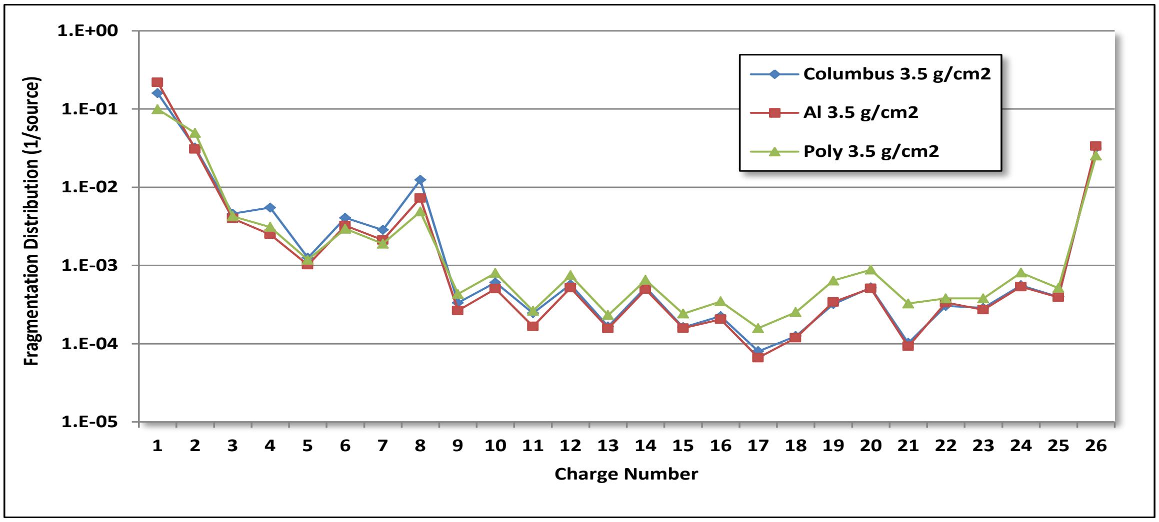

Figure 5.6: Simulated fragmentation distribution as a function of the fragment charge number after the Columbus hull mock-up and equivalent areal densities of aluminum and polyethylene irradiated by 964.9 MeV/n ^{56}Fe ions. Lines are used to connect the points.

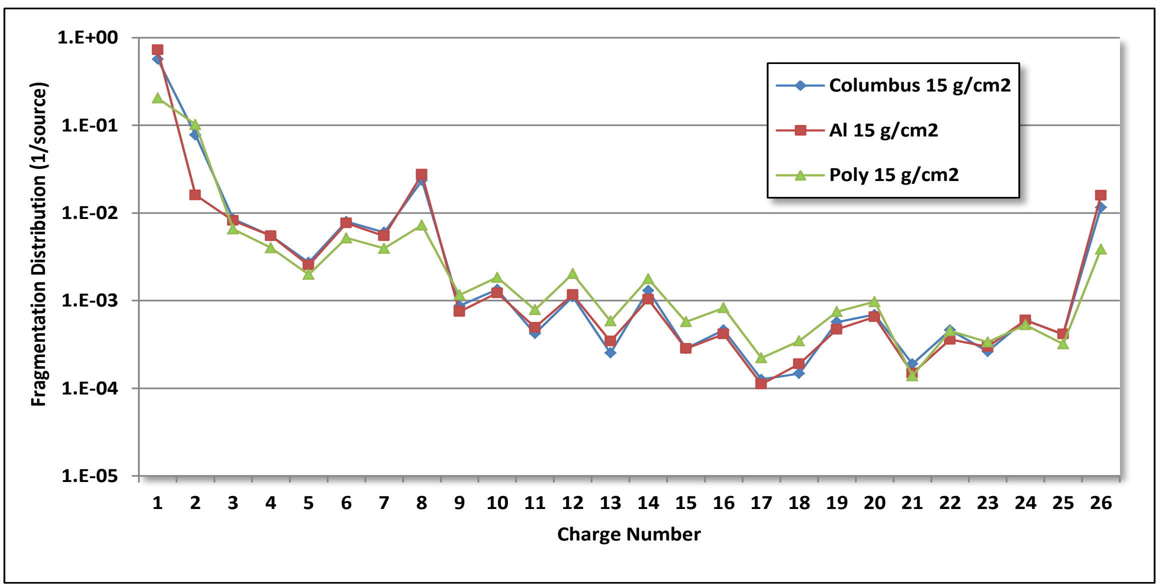

Figure 5.7: Simulated fragmentation distribution as a function of the fragment charge number after the Columbus plus internal structures mock-up and equivalent areal densities of aluminum and polyethylene irradiated by 964.9 MeV/n ^{56}Fe ions. Lines are used to connect the points.

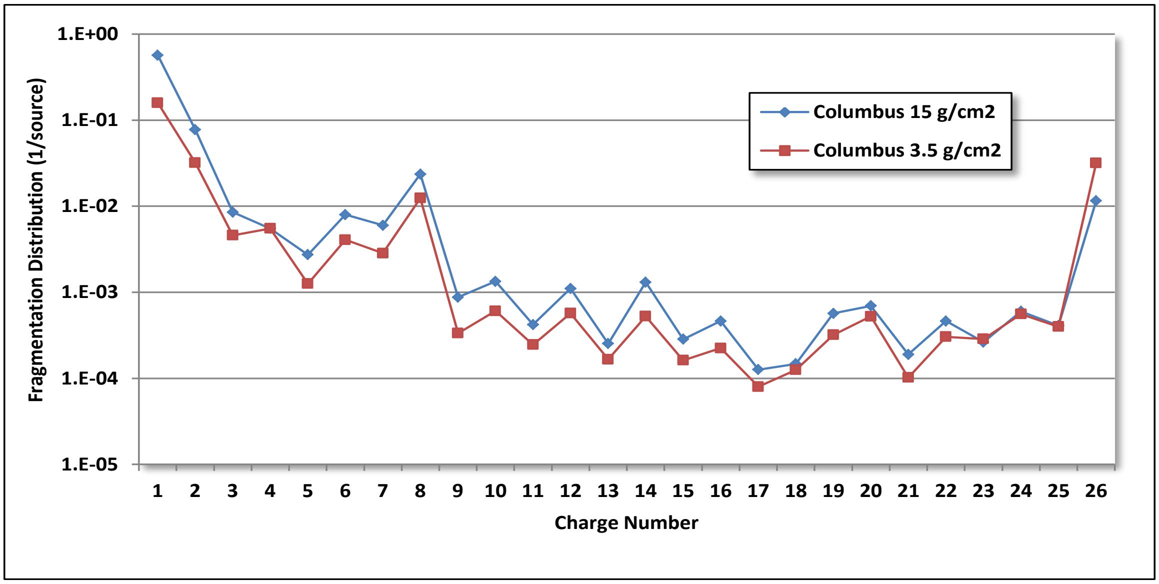

Figure 5.8: Simulated fragmentation distribution as a function of the fragment charge number after the Columbus hull and Columbus plus internal structures mock-ups irradiated by 964.9 MeV/n ^{56}Fe ions. Lines are used to connect the points.

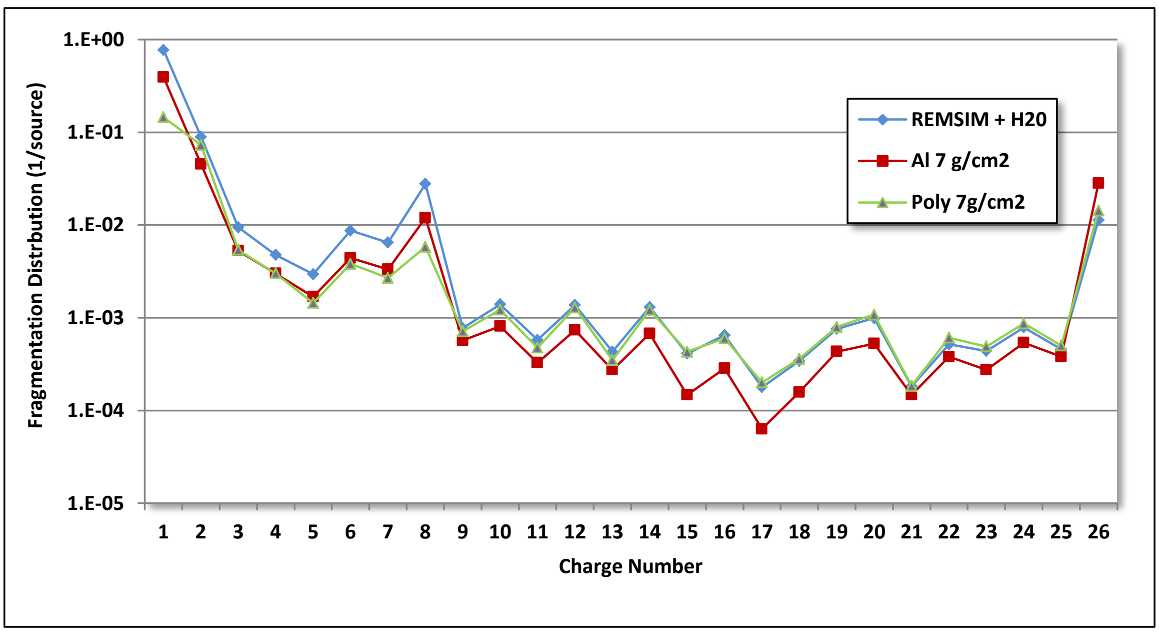

Figure 5.9: Simulated fragmentation distribution as a function of the fragment charge number after the REMSIM plus water mock-up and 7 g/cm^2 areal densities of aluminum and polyethylene irradiated by 964.9 MeV/n ^{56}Fe ions. Lines are used to connect the points.

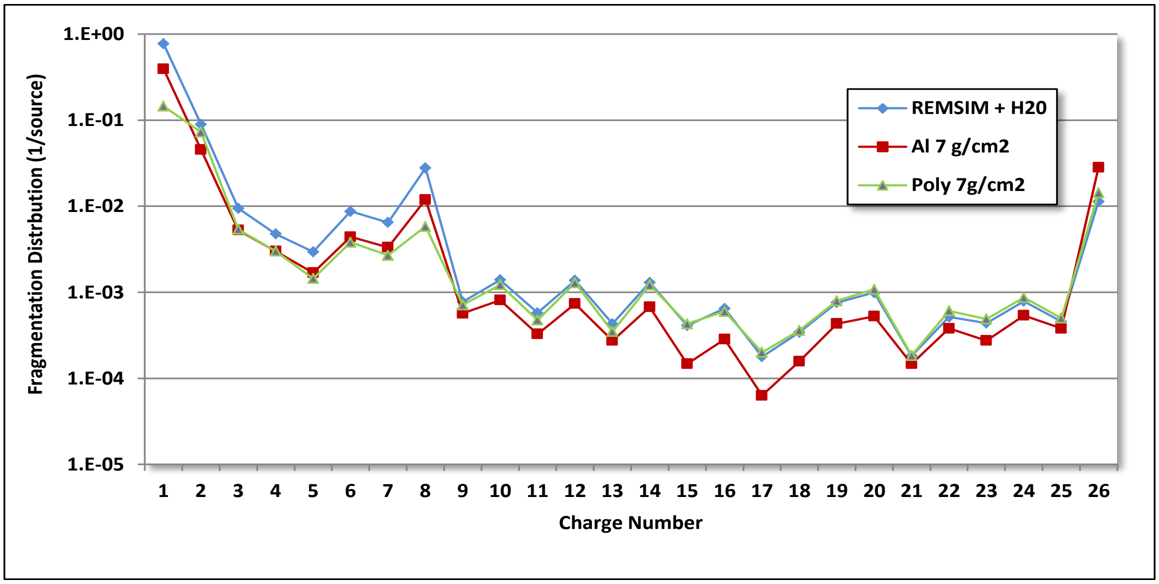

Figure 5.10: Simulated fragmentation distribution as a function of the fragment charge number after the Columbus and REMSIM mock-ups irradiated by 964.9 MeV/n ^{56}Fe ions. Lines are used to connect the points.

SIMULATIONS OF EXPERIMENTAL DATA FOR PROTONS

The beam line geometry described in Figure 5.3 was again used as input to the PHITS simulations and as with the simulations with ^{56}Fe, the aluminum and polyethylene comparison runs were first simulated for protons. The aluminum and polyethylene plates were also modelled as rectangular parallel planes of appropriate areal density and dimensions (areal densities of 7 g/cm^2, and 15 g/cm^2 with dimensions reported in Table 3.2). A monoenergetic beam of 1 GeV protons was used as an input source. The results for the simulations for all measurements taken at 0.254 cm behind the shielding materials are shown in Figure 5.11. PHITS appears to reproduce the experimental results fairly well indicating that the physics parameters chosen for the PHITS input are appropriate. The general increase in absorbed dose close to the shielding material, seen in the experimental portion of this effort and reported in Mancusi et al. (2007) and

Destefanis et al. (2007), is replicated by PHITS. Although the PHITS simulations show the largest increase in dose to be produced when irradiating aluminum with 1 GeV protons (Mancusi et al. 2007), it appears to under estimate the measurements for the areal densities of aluminum tested in these experiments. It is also apparent that the increase in dose, approximately 25%, is the nearly same for the polyethylene slabs, Columbus plus internal structures mock-up and REMSIM plus water. Recall from Figure 4.7 that this was seen in the physical measurements as well.

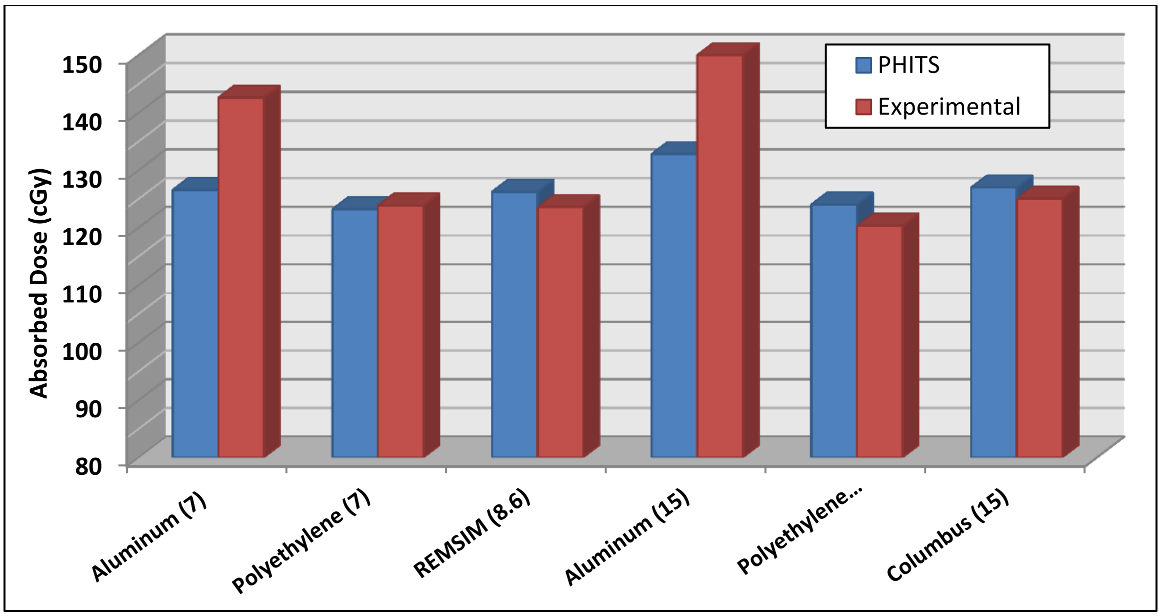

Figure 5.11: Comparison of the absorbed dose calculated by PHITS simulations of the 1 GeV proton beam to the experimental results.

Evaluating the particle types and their contribution to the absorbed dose in the simulations shows that the dose along the beam axis is dominated by protons; in fact, greater than 97% of the dose is due to protons. Pions, muons and electrons, resulting from ionizations from photons, and other hadrons combine for the remaining contribution. Figure 5.12 reports the varying contributions of particles to the dose. Pions are the second largest contributor; followed by electrons and other hadrons, and muons contribute only minimally to the dose. Pions are produced in nuclear reactions of GCR particles with shielding materials and tissue at energies above a few hundred MeV/n. The number of pions produced increases with kinetic energy of the GCR particle with multi-pion production processes occurring above 500 MeV/n. Most pions are produced by protons, helium and secondary neutrons because of their high abundances in the GCR and the fact that the pion production cross section increases with mass number (Cucinotta et al. 2012). Although the quality factor for pions is low, these simulation results show that pions contribute to the absorbed dose and should be included in dose equivalent and effective dose calculations for an improvement in risk assessments. The category listed as others is a combination of neutrons and other hadrons and Figure 5.12 shows that the irradiation of the 15 g/cm^2 aluminum slab produced the largest number of these particles. It is also seen that the more realistic Columbus plus internal structures mock-up irradiation results in a decrease in the production of the neutrons when compared to either polyethylene or aluminum. Although dose equivalent was not calculated for this experimental data, the simulations seem to indicate that the Columbus plus internal structures mock-up would result in a lower dose equivalent.

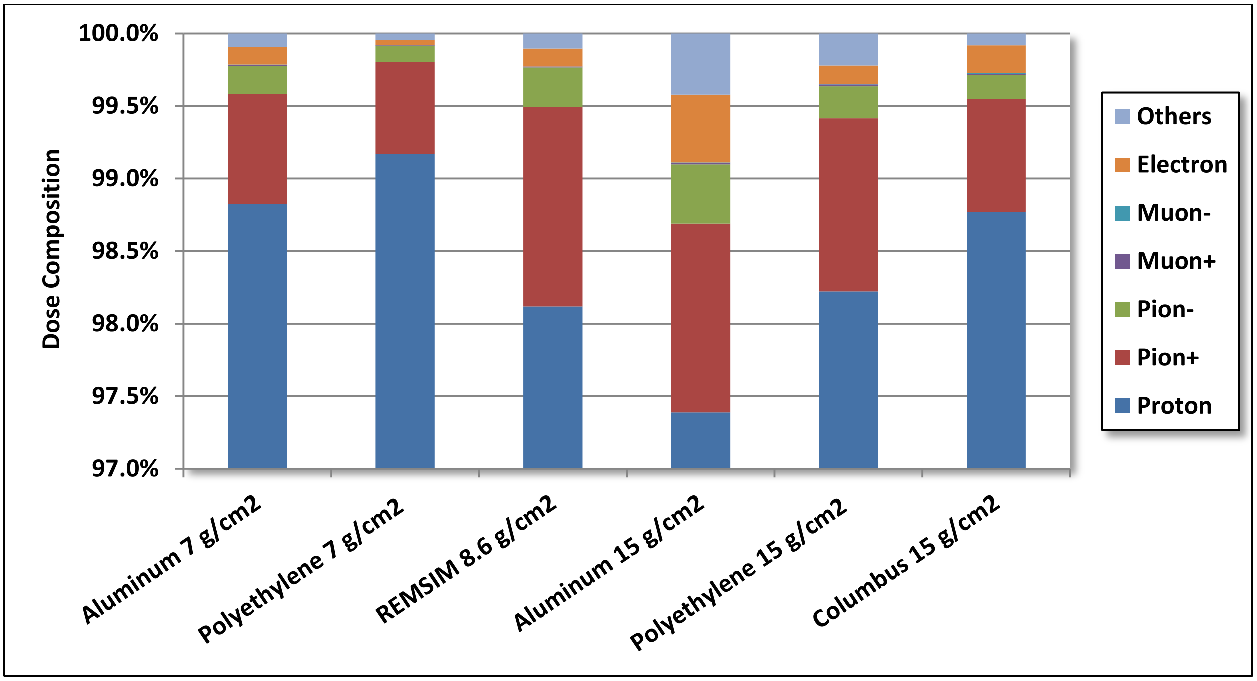

Figure 5.12: PHITS simulated dose contribution when various shielding materials with different areal densities are irradiated by a 1 GeV proton beam.

For the Columbus plus internal structures and REMSIM plus water shields, the dose was also measured at different distances along the beam axis both before and after the mock-up. The dose measured and simulated in the sample position was increased by the shielding. The dose was normalized to the simulated dose value at the first measurement of the Egg Chamber with the shielding material removed. The simulations reproduce very accurately the measurements for the Columbus mock-up; however, there are some deviations from measured for the REMSIM simulations. These results are reported in Figures 5.13 and 5.14. PHITS appears to overestimate the measured results for REMSIM by 2-6%. GEANT4 simulations of this same data published in Destefanis et al. (2008) show similar deviations between the measured and calculated values for the REMSIM plus water mock-up while the comparisons for the Columbus mock-up show much better agreement. These deviations could be explained by the uncertainty introduced into the simulation from the geometry issues inherent in modelling the small volume of the Egg Chamber as the simulation "detector".

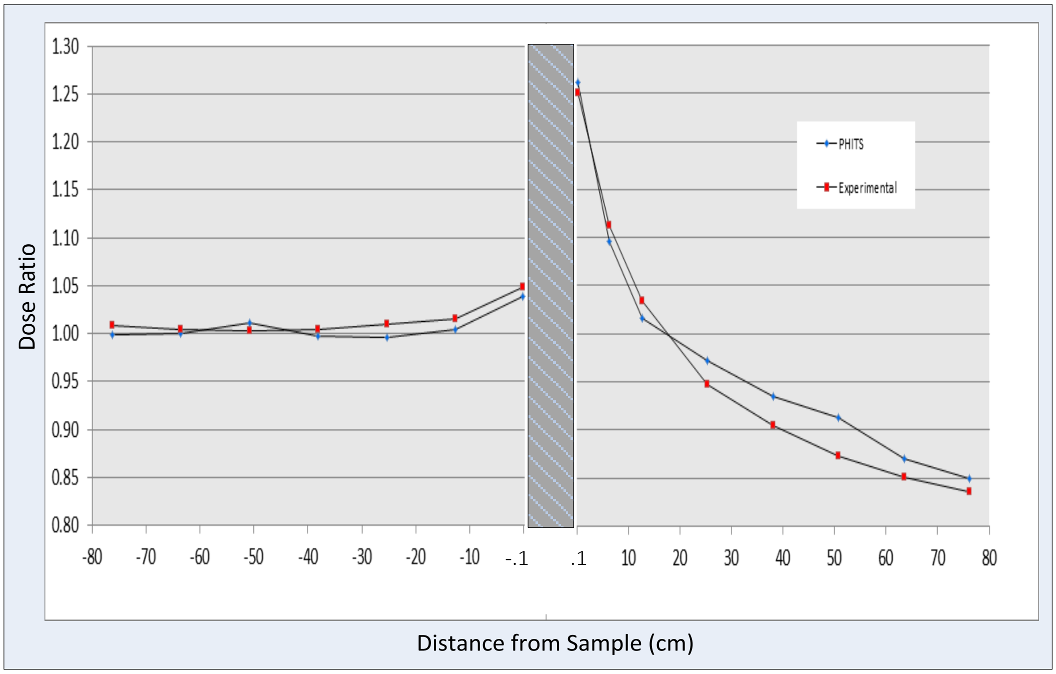

Figure 5.13: Dose ratio calculated by PHITS compared to measured values as a function of distance along the 1GeV proton beam axis for the 15 g/cm^2 Columbus mock-up. Lines are used to connect the points.

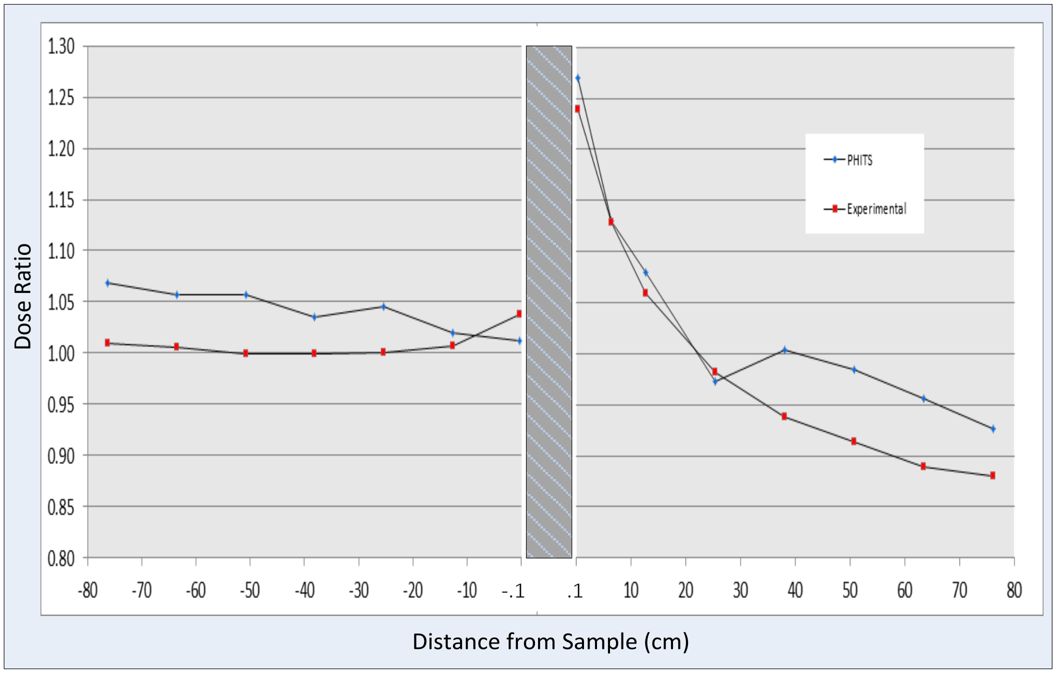

Figure 5.14: Dose ratio calculated by PHITS compared to measured values as a function of distance along the 1 GeV proton beam axis for the 8.6g/cm^2 REMSIM mock-up. Lines are used to connect the points.

As shown in Figures 5.15 and 5.16, the simulation indicates that protons account for over 98% of the measured dose both in front and behind the shield, regardless of distance. The remaining fraction is attributed to pions, muons, electrons, and other hadrons, including neutrons. The simulations also show that secondary protons, emitted from the target, are mostly responsible for the observed increase in dose near the shielding material. The dose composition exhibits similar behavior for both of the shielding materials. Protons account for 99.5% initially and this trend is seen until the distances near the shield. At a distance greater than 25 cm behind the shield the proton contribution is comparable to the contribution prior to the shield. In the simulated measurements near the shield, pions contribute nearly 1% of the dose. The simulation for REMSIM shows that the pions produced have a wider energy range, however, much of these are at low energies and are thus easily attenuated by air. It was noted earlier that the distance separating the astronaut from the spacecraft hull and the exterior of the rack structure is 42 inches on the ISS, a dose reduction of 12-15% was observed in these experiments at similar distances leads me to the inference that a similar dose reduction would be expected. Again, the category listed as others is a combination of neutrons and other hadrons. A comparison of the results graphed in Figures 5.15 and 5.16 indicates that the production of neutrons is less for the REMSIM mock-up at all distances near the shielding material. This is expected due to the inclusion of water in the REMSIM mock-up. At distances behind either shield that are consistent with the standard rack dimensions, the contribution to dose from the neutrons are similar for both shield mock-ups.

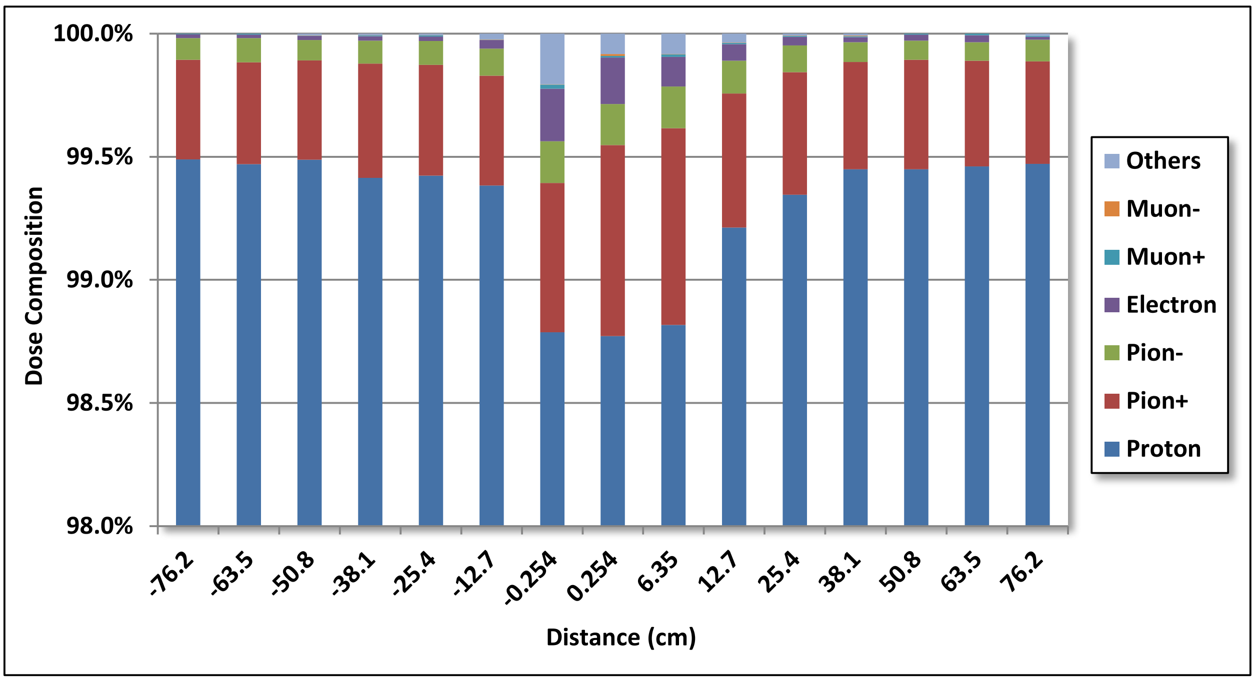

Figure 5.15: PHITS simulated dose contribution at different distances when the Columbus plus internal structures mock-up with an areal density of 15 g/cm^2 was irradiated with 1 GeV proton beam.

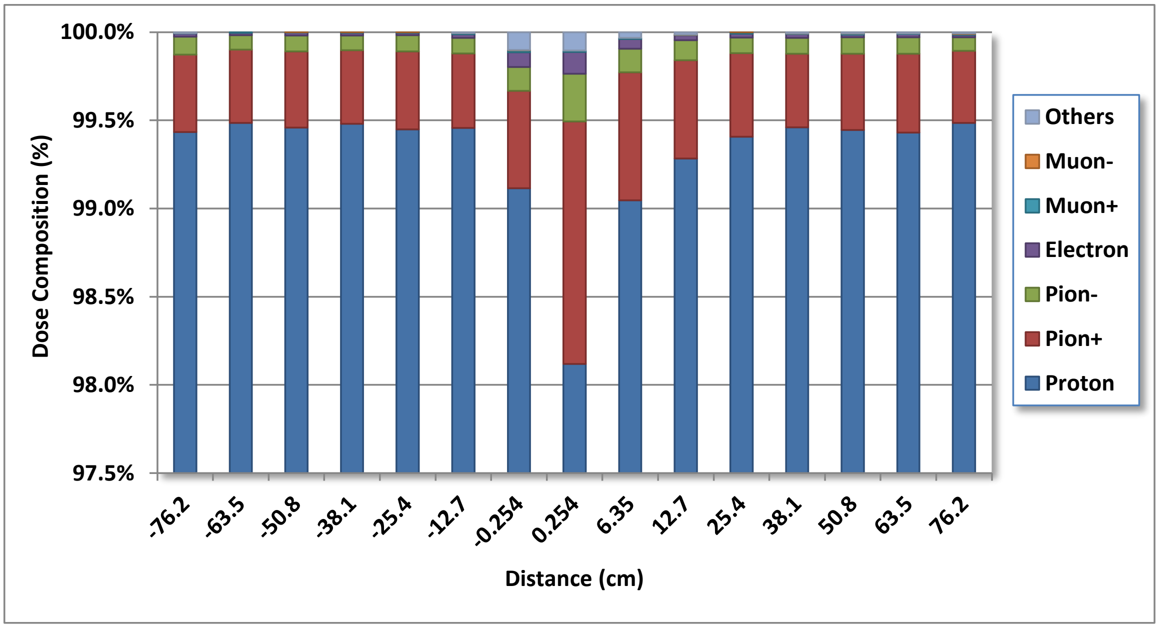

Figure 5.16: PHITS simulated dose contribution at different distances when the REMSIM plus water mock-up with an areal density of 8.6 g/cm^2 was irradiated with 1 GeV proton beam.

Testing Order Matters

PHITS simulation results compared to the BNL measured data for the four polyethylene and aluminum configurations are described in Table 5.1 for the ^{56}Fe experiments and Table 5.2 for the proton experiments. In this portion of the work, the simulation results were shown to under estimate the measured values but in general compare favorably to the measured data in trends. The under prediction was found to be up to 10% for the ^{56}Fe simulations and up to 20% for the proton simulations. The tendency for PHITS results to under predict has been reported previously and related to a consistent under prediction in the charge changing cross sections (Zeitlin et al, 2008; Sihver et al. 2008). In Zeitlin et al. 2008, the authors showed that PHITS consistently underestimated measured charge changing cross section data in think targets of aluminum, polyethylene and lead. The underestimation was most significant for fragments with Z<9. In Sihver et al. (2008), the authors showed that benchmarking of

PHITS against FLUKA, HETC-HEDS, and NUCFRG2 for projectiles heavier than Silicon, PHITS consistently under predicted the charge changing cross sections. When layering materials in simulations, uncertainties present during the transport in one material can be effectively cancelled by competing uncertainties in the next.

Table 5.1 shows that for the ^{56}Fe irradiations and configurations where the polyethylene slab was first, there is a modestly lower, about 3%, measured dose and PHITS calculated dose and dose equivalent than the values for the configurations where aluminum was first. Within a total areal density (10 g/cm^2 or 20 g/cm^2) changing the order of the materials for the same areal density did not significantly change average quality factor. When the areal density is increased from 10 g/cm^2 to 20 g/cm^2 total, there is a decrease in measured dose, PHITS calculated dose and dose equivalent, and average quality factor. The reductions are consistent with increasing the areal density. The calculated fragmentation distributions for all configurations are presented in Figure 5.17. The distributions are more tightly grouped indicating that the change in quality is more complicated and the layering of materials may have effectively a cancelling effect

Shielding	Egg Dose (cGy)	PHITS Dose (cGy)	PHITS Dose Equivalent (cSv)	Average Q
Al/poly 20 g/cm^2	131.6	127.7	984.84	7.71
Poly/Al 20 g/cm^2	127.8	123.3	959.49	7.78
Al/poly 10 g/cm^2	149.4	141.0	1132.86	8.04
Poly/Al 10 g/cm^2	151.3	134.5	1082.44	8.05

Table 5.1: Comparison of PHITS simulations of dose, dose equivalent, and average Q for a 964.9 MeV/n ^{56}Fe irradiation of aluminum and polyethylene with mutually changing position with experimental results.

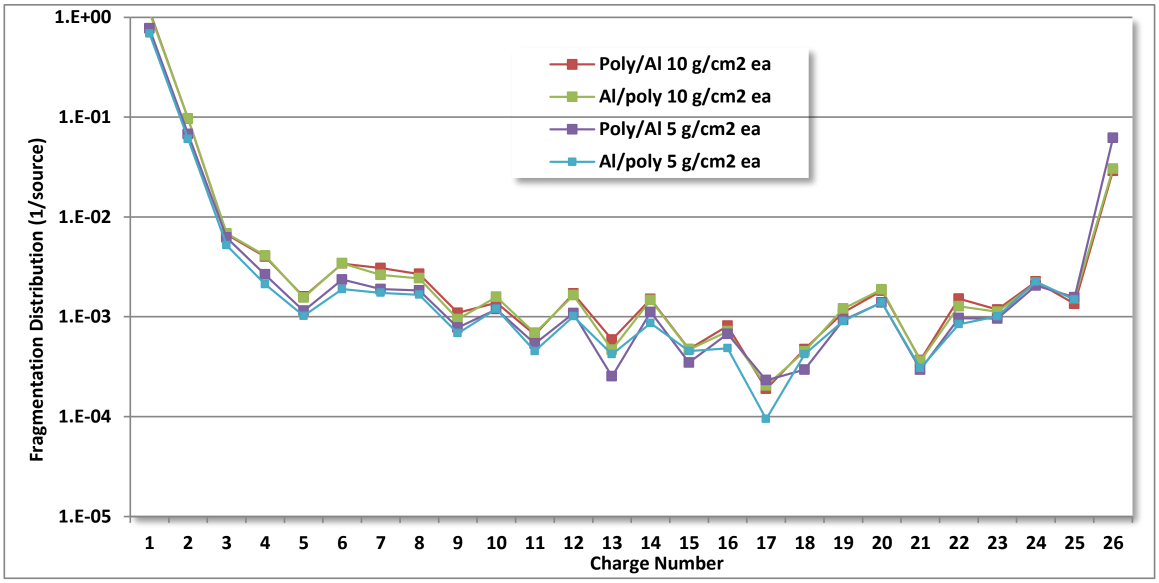

Figure 5.17: Simulated fragmentation distribution as a function of the fragment charge number for aluminum and polyethylene with mutually changing position irradiated by 964.9 MeV/n ^{56}Fe ions. Lines are used to connect the points.

Table 5.2 shows that for the 1 GeV proton irradiations the results are different. Changing the orientation of aluminum and polyethylene does not appreciably change the measured dose and PHITS calculated quantities. The increase in dose following the shielding material reported previously in this work and in literature (Mancusi et al, 2007; Bertucci et al, 2007) was seen and replicated with PHITS. The measured dose and PHITS calculated quantities decrease with increasing distance from the shield. The contribution to dose from particles other than protons becomes more apparent. For the configuration where 10 g/cm^2 polyethylene is placed in front of 10 g/cm^2 of aluminum, protons only account for about 66% of the dose, while neutrons and photons account for about 30%. At the detector location of 0.254 cm, the PHITS calculated average Q was increased to ~2.5 and decreased with distance from the shield. Figure 5.18 shows this increase in dose and dose equivalent to be the result of neutrons and photons produced in the shielding materials. Secondary protons are increased but not to the extent seen with the Columbus or REMSIM mock-ups. Pions and electrons also contribute to the increase in dose. Limited measurements were taken experimentally and longer distances were not simulated so comparisons with the values obtained for Columbus and REMSIM mock-ups are not possible. Forward work could involve using PHITS to estimate the dose, dose equivalent and average Q.

Shielding	**Egg Dose (cGy)**	**PHITS Dose (cGy)**	**PHITS Dose Equivalent (cSv)**	**Average Q**
Al/Poly 20 g/cm^2 @ 0.254 cm	151.00	125.02	306.89	2.45
Al/Poly 20 g/cm^2 @ 2.54 cm	140.70	107.38	211.49	1.97
Al/ Poly 20 g/cm^2 @ 5.08 cm	130.80	103.70	189.15	1.82
Poly Al 20 g/cm^2 @ 0.254 cm	163.50	140.05	354.99	2.53
Poly Al 20 g/cm^2 @ 2.54 cm	150.90	120.60	279.14	2.31
Poly Al 20 g/cm^2 @ 5.08 cm	139.80	113.97	248.57	2.18
Al Poly 10 g/cm^2 @ 0.254 cm	143.10	125.22	315.27	2.52
Al Poly 10 g/cm^2 @ 2.54 cm	133.60	114.62	250.71	2.19
Al Poly 10 g/cm^2 @ 5.08 cm	125.90	109.11	204.27	1.87
Poly Al 10 g/cm^2 @ 0.254 cm	143.40	137.89	367.72	2.67
Poly Al 10 g/cm^2 @ 2.54 cm	136.60	121.94	264.07	2.17
Poly Al 10 g/cm^2 @ 5.08 cm	127.90	114.80	222.30	1.94

Table 5.2: Comparison of PHITS simulations of dose, dose equivalent, and average Q for the 1 GeV proton irradiation of 5 g/cm^2 and 10 g/cm^2 aluminum and polyethylene with mutually changing position with experimental results.

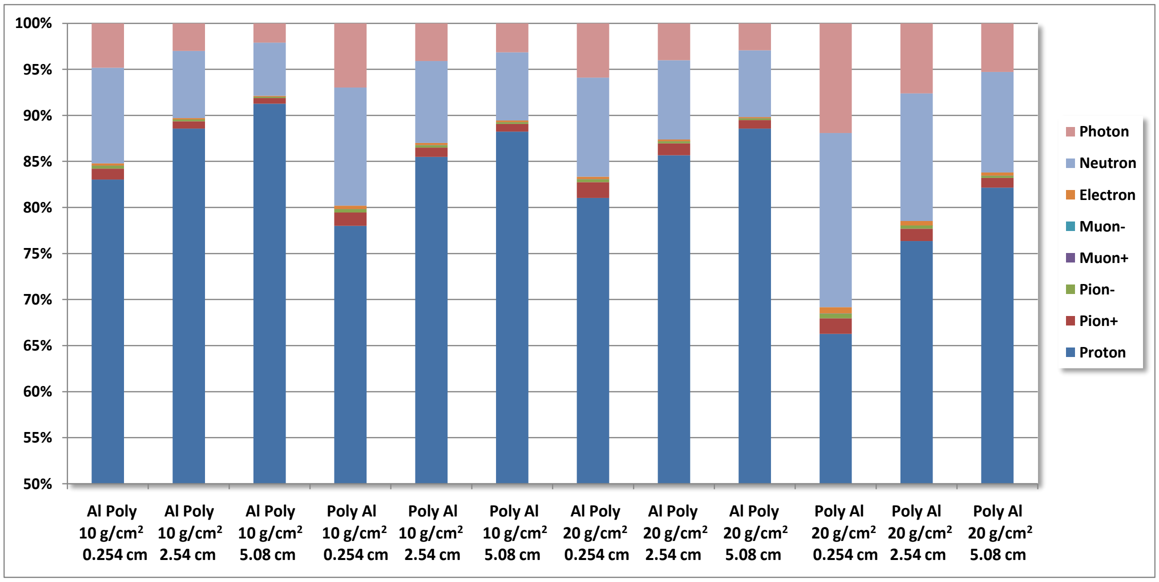

Figure 5.18: Contribution of particles to absorbed dose in the Egg chamber for aluminum and polyethylene shielding in mutually changing order for the 1 GeV proton beam irradiations.

Simulations of the Angular Distribution

PHITS has been shown to accurately reproduce how the dose varies when the dimension along the beam axis is changed. There are limitations in all measurements and simulations previously reported in this paper, as these measurements and subsequent simulations were taken along the beam axis and neglected any lateral scattering. In this aim the contribution to dose in off axis measurements was explored. PHITS was used to simulate dose deposition after the traversal of a 3 cm target of aluminum. The geometry representation in PHITS for the NSRL target room shown in Figure 5.3 was again used for the PHITS input. However, the source input for PHITS was a cylindrically symmetrical Gaussian beam of FWHM of 1.79 cm of monoenergetic protons with an energy of 980 MeV. The Egg Chamber was simulated identically as in the other aims, as a 1 cm^3 sphere of air resulting in a beam size radius larger than the Egg Chamber. These spheres were located 90° to the beam line at varying distances in the x direction (0, 0, +1), (-5.08, 0, +1), (-10.16, 0, +1) and (-15.24, 0, +1) to most nearly match the experimental configuration. Although measurements recorded during the experiments at BNL were in inches, all measurements simulated and reported are in centimeters.

As shown in Table 5.3, PHITS reproduces the experimental data fairly well except at small angles, measurement (-5.08, 0, +1) where the simulated result is an order of magnitude higher than measured. A review of the output of the proton spectrum for this simulation shows the proton energy deposited in the simulated detector is dominated by the source proton energy. There are two possible explanations for this over estimation. The most likely cause is a misspecification in the source geometry for the simulation when compared to the experimental configuration leading to simulated lateral beam spreading that overlaps the virtual detector. Very different results can be obtained when varying the radius of the simulated source. However, all changes in geometry explored did not yield results that fully explain this. A second less likely reason is based on previously published work that reported the increase in dose seen near the shield to be from the production of secondary protons emitted from the target (Mancusi et al. 2007). These evaporation protons are emitted isotropically. The increase could be accounted for by an over prediction of the secondary protons by the physics models in PHITS. The results for the other measurement locations are in good agreement with the measured values. The increase in dose following the shielding material reported previously, here and the published literature (Bertucci et al. 2007; Mancusi et al. 2007; Destefanis et al. 2008) is replicated here for the measurement along the beam axis. The slight underestimation by PHITS for the measurement locations (-10.16, 0, +1) and (-15.24, 0, +1) is consistent with published literature (Sihver et al. 2010; Lee et al. 2011).

Egg Position (cm)	Beam Dose (cGy)	Egg Dose (cGy)	Egg Dose / Beam Dose	Simulated Egg Dose / Virtual Dose
(0, 0, +1)	200.14	187	0.934	1.12
(-5.08, 0,+1)	2500	32.9	0.0132	0.140
(-10.16, 0, +1)	10000	48.04	0.00481	0.00474
(-15.24, 0, +1)	40000	103.81	0.00267	0.00189

Table 5.3: Comparison of measured and PHITS simulated dose distributions for off axis measurements for a 980 MeV proton beam on an aluminum target.

The simulations of the off axis measurements demonstrate that other particle types become more important as the distance from the beam axis is increased as shown in Figure 5.21. Protons are shown to dominate the contribution to dose for the measurements at x = 0 and x = 5.08 cm. The PHITS tally, T-Track, was used to track the particle types crossing the Egg Chamber. Figure 5.19 shows the contributions. Neutrons account for 40-45% of the particles crossing the Egg chamber at the distances in the x direction corresponding to 10.16 cm and 15.24 cm. With angular distance from the shield, the contribution from all particle types, except protons, increases. Photons are also shown to increase. The electrons are produced by photon interactions. The type listed as others is composed of other hadrons not specifically tracked by the tally. These results provide evidence of the value of the incorporation of 3D Monte Carlo calculations when conducting astronaut dose calculations.

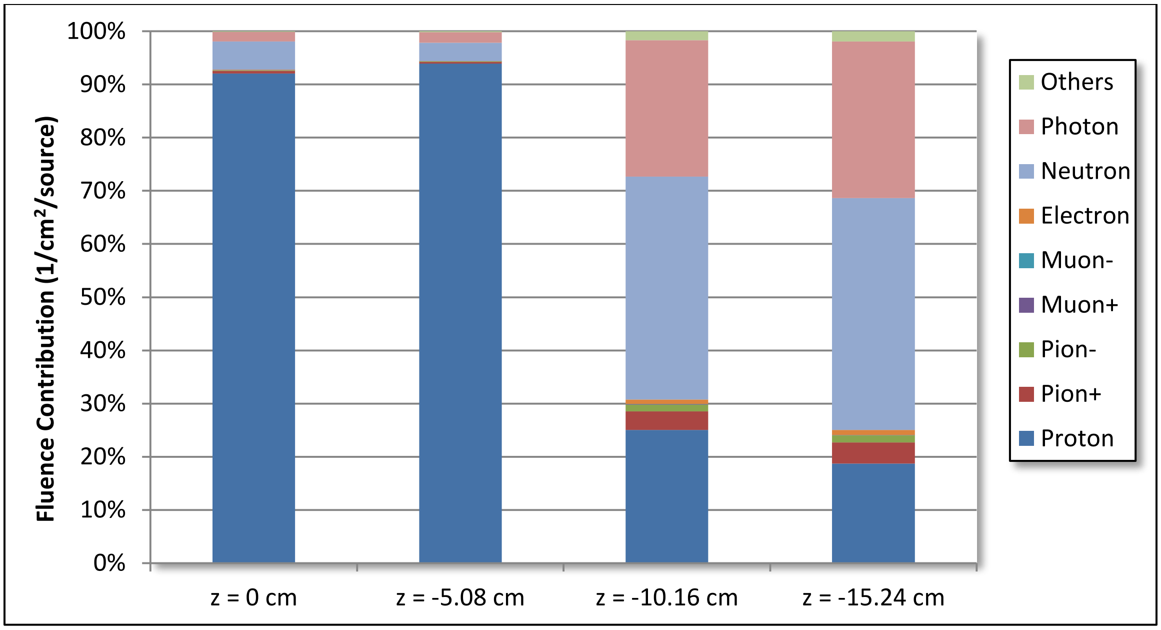

Figure 5.19: Contribution of particles to absorbed dose in the Egg chamber for a 980 MeV proton beam irradiation of an aluminum target.

STATISTICAL UNCERTAINTY IN PHITS SIMULATIONS

Graphing the experimentally measured values compared to the PHITS simulated ones as in Figures 5.20 and 5.21 displays the linear relationship between the observed and predicted results. In extrapolating the trend line toward zero, a minimal offset from zero is seen indicating a slight and likely negligible over prediction of the measured values by PHITS for the ^{56}Fe simulations. However, the trend line for the proton simulations goes through zero. The good agreement between PHITS simulations and accelerator measurements has also been demonstrated for other studies (Sihver et al. 2007) and this work further indicates that PHITS is an accurate radiation transport tool. As noted in Chapter 3, PHITS estimates the relative error for each tally based on the number of events contributing to the tally and this is not the statistical uncertainty in the tallied quantity. Since a large number of particles, (9.5×10^6) were transported for each simulation, the relative error for each individual tallied quantity was on the order of 0.3%. Four simulations for each of the experimental geometries were performed to allow for a post simulation statistical assessment. When standard error of the mean (SEM) was calculated, a SEM on the order of 0.3% was determined and in general would be contained within the symbols on the graphs. This low uncertainty is based on the large number of simulated events contributing to the tally and clearly underestimates the true uncertainty in the Monte Carlo simulations. This limitation present in PHITS version 2.24 has been corrected with the modification of the code to include statistical uncertainties of tally results by calculating the standard deviation of the tallied quantity. (Sato et al. 2013). Error bars are therefore not shown on these of any of the following results presented in this paper.

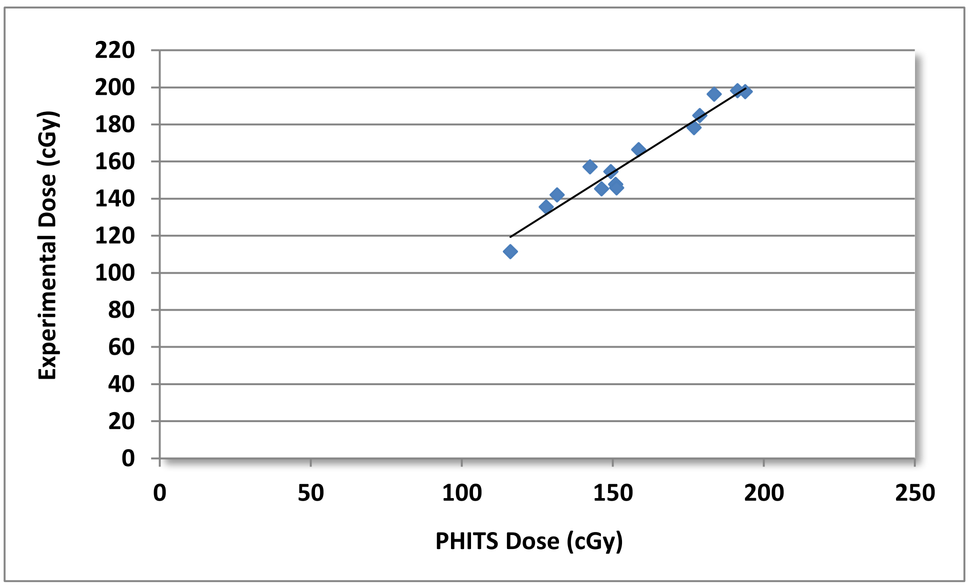

Figure 5.19: Comparison of measured experimental dose from a 964.9 MeV/n ^{56}Fe beam to predicted dose by PHITS for the same monoenergetic beam.

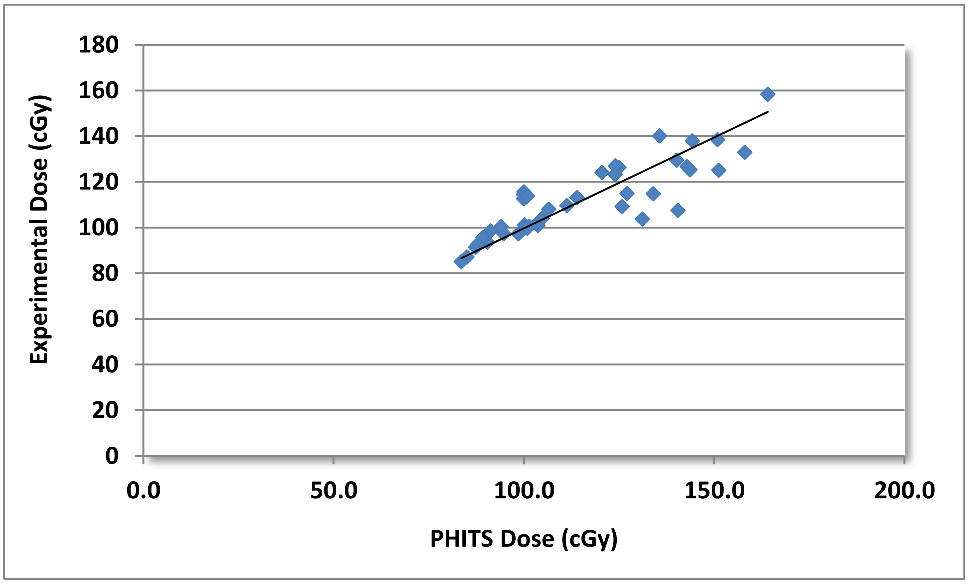

Figure 5.20: Comparison of PHITS simulations of the 1000 MeV proton beam to the experimental results.

With any transport code simulation there are uncertainties in the results. There are uncertainties systematically introduced to the problem based on beam energy, energy spread, beam profile and shape, details of the geometry. Assumptions necessary to bound the problem to a manageable calculation contribute to these uncertainties. Additional uncertainty is introduced in the transport code calculation. Transport codes rely heavily on measured nuclear cross sections for accurate predictions. Although many measurements of cross sections have been obtained, there are still notable gaps, especially for light ions, which lead to uncertainties in the results from any code. Proton cross sections have been the most heavily investigated, however, disagreements of a factor of 2 exist (Norbury & Miller 2012; Durante 2014). These gaps lead to uncertainties in the physics models and could easily lead to errors on the order of 20%. Recent evaluations of several transport codes that have been conducted by NASA are illustrated in Figure 5.21 show variation in results across the full spectrum. This work shows that the variation in neutron spectra from the Monte Carlo codes is still a factor of two across the whole spectrum (Wilson et al. 2014). This highlights the continued need for continued measurements of cross sections against which to benchmark transport codes.

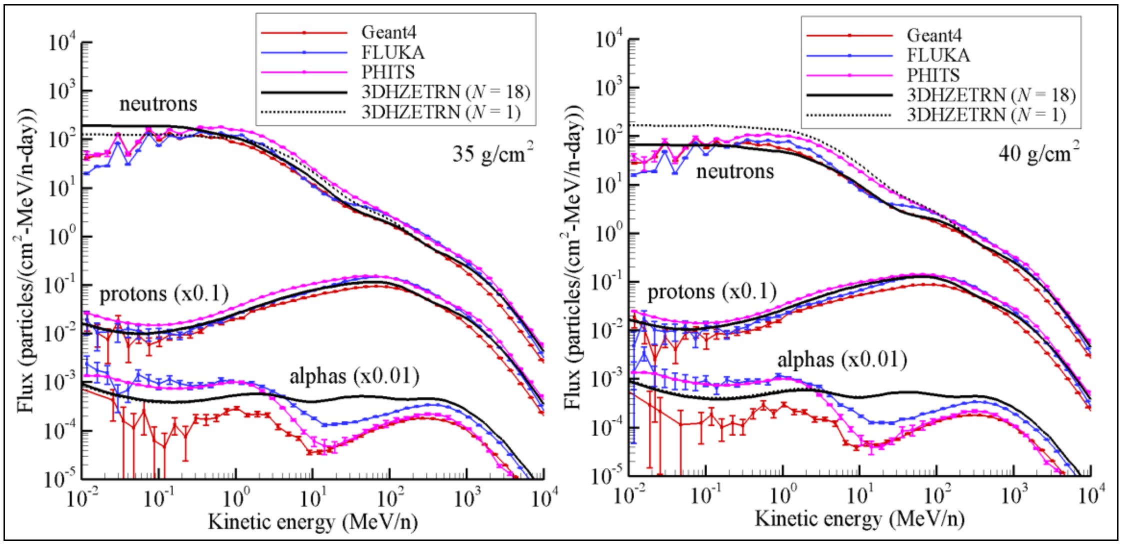

Figure 5.21: Transport code result comparison for exposure to solar minimum GCR iron at the bottom of an aluminum sphere. From Wilson et al. 2014

Chapter 6: Conclusions

Need for present study

The need to understand and manage the risk of radiation exposure within its decision making framework, has led NASA to develop a comprehensive effort to decrease the uncertainties associated with evaluating and projecting risks from space radiation. This effort is not limited to understanding the uncertainties inherent in the radiation biology of HZE ions. Improvements in the methods and understanding in the areas of the radiation protection characteristics of spacecraft materials is warranted to provide a sound basis for the design trades that are necessary when designing long duration space missions. The need to inform NASA decisions on spacecraft materials, mass constraints, and mission lengths within the currently available scientific knowledge was the motivation behind this work. Prior to the proposal of this work, accelerator experiments to evaluate the dose reduction effectiveness of spacecraft materials have focused on single materials, i.e. aluminum and polyethylene, not layered mock-ups more closely representing a spacecraft wall (Miller et al. 2003; Guetersloh et al. 2006; Zeitlin et al. 2006; Mancusi et al. 2007; Zeitlin et al. 2008).

Findings

Columbus and REMSIM Evaluations

Two aims of the study were to determine the dose reduction capabilities of more realistic mock-ups of spacecraft structures when irradiated by 1 GeV/n ^{56}Fe ion and proton beams. Two vehicle hull mock-ups, the ISS Columbus module and a proposed inflatable habitat, REMSIM, were studied and results were compared to those of standard spacecraft materials, aluminum and polyethylene. As expected polyethylene was found to be superior in dose reduction capability, but reasonable reductions could be obtained when more realistic layered hull materials were irradiated with either particle. Internal structures and payloads contribute mass from low mass materials, i.e. Kevlar®, plastics and water, which should be included to improve accuracy in the calculations of equivalent dose. These materials do not add parasitic mass to the vehicle and optimization of the placement of these materials can result in dose reductions as shown in Shavers et al (2004), NASA (2006), and Kodaira et al. (2014).

When the dose reduction capability for these two mock-ups are compared to each other for the ^{56}Fe irradiation, there were no major differences in dose reduction and fragmentation spectra as determined by PHITS. This comparison suggests that an astronaut in an inflatable habitat with appropriately place water or fuel tanks could experience very similar conditions to an astronaut in a typical spacecraft when hit by 1 GeV/n ^{56}Fe ions. A similar situation was present when the mockups were compared for the 1 GeV proton irradiation. A nearly identical increase in dose adjacent to the shield was observed on measurement and with the PHITS predictions. The dose decreased with increasing distance from the shielding material with the same pattern. When considering the production of neutrons and other hadrons produced as a result of the irradiation of the shielding material, lower fluence rates were observed for REMSIM suggesting perhaps that dose equivalent would be lower.

Testing Order Matters

Differences in dose reduction capability and dose equivalent were evaluated for four different areal densities and order of layered aluminum and polyethylene sheets to investigate whether the order of the materials matters. The configurations tested were:

- 5 g/cm^2 Polyethylene+ 5 g/cm^2 Aluminum

- 5 g/cm^2 Aluminum + 5 g/cm^2 Polyethylene
- 10 g/cm^2 Polyethylene+ 10 g/cm^2 Aluminum
- 10 g/cm^2 Aluminum + 10 g/cm^2 Polyethylene

Overall a 25%-35% reduction in dose was seen for all four configurations for the ^{56}Fe experiments. However, when comparing the configurations to each other, a slightly lower dose (~3%) was seen was seen for the two configurations where polyethylene was placed before the aluminum. The PHITS calculated dose equivalent was also about 3% lower. However, within a total areal density (10 g/cm^2 or 20 g/cm^2) changing the order of the materials for the same areal density did not significantly change average quality factor. A decrease in all quantities was seen with an increase in areal density. When evaluating the fragmentation spectra for all four configurations the spectra are tightly grouped together, indicating that the order of materials has little effect on the quality of the radiation filed behind the shield.

In the 1 GeV proton investigations, the dose was increased directly adjacent to the shielding material for all four configurations; 50-60% for the 20 g/cm^2 configurations and 40% for the 10 g/cm^2 ones, resulting in increased PHITS calculated quantities of dose equivalent and average Q. These values decrease with increasing distance from the shield. Changing the order of the materials produced subtle increases of 3-5% in radiation quality for the two configurations where polyethylene was placed first. This slight increase could be inferred to result in a higher total dose equivalent for an astronaut exposed to 1 GeV protons in this configuration. In the current practice on the ISS, the polyethylene sheets are placed between the aluminum vehicle wall and the aluminum rack system, resulting in a more complicated arrangement. However, as novel approaches where polyethylene polymers are used for structural components, this finding should be considered (Durante 2014).

Off-Axis Measurements

Few off axis measurements of shielding materials have been obtained at accelerators leading to a limited understanding of the angular distribution of particles produced when interacting with aluminum. The simulations of the off axis measurements demonstrate that other particle types become more important as the distance from the beam axis is increased. In particular, the contribution from neutrons and photons increases with distance at a 90° angle from the aluminum target. The geometry of the simulations conducted in this work influenced the results and forward work is necessary to elucidate the root of the geometry problem. PHITS has been shown to replicate measurements taken at small angles for 290 and 400 MeV/n ^{12}C beams for many targets (Zeitlin et al. 2007) leading me to conclude that the over prediction of the dose at small angles is a geometry problem. In Zeitlin et al. (2007), the angular measurements were obtained at a sufficient distance from the target that beam spreading would not have influenced the results. The limited measurements and simulations in the current work indicate a need to further investigate the angular contribution of particles to dose.

PHITS Monte Carlo Code

The Monte Carlo transport code PHITS is a relatively new code package when compared to other transport code suites. Its use as a tool in performing radiation dose calculations was explored. PHITS estimations generally agreed well with the experimental results, but underestimated the measured values in many of the proton irradiations. This underestimation has been found in other studies with PHITS and the other transport codes described in this study (Sihver, et al 2008). It has also been shown that the biological response depends not only on the LET, but also on the specific charge and velocity of the ion species (Friedrich et al. 2012, Friedrich et al. 2013). Therefore, for a comprehensive risk assessment model, the Monte Carlo simulation appears to be still irreplaceable.

LIMITATIONS AND FUTURE WORK

Several simple limitations were preset in this work. For the PHITS simulations I used the geometry of actual volume of the Egg chamber. Using a small volume for the detector in the simulations introduces uncertainties. Given the stated small disuniformity in both of the beams, using a monoenergetic ^{56}Fe and proton source was a reasonable approximation. As discussed in more detail in the forward work section, the relatively sparse cross section data available for use in transport codes leads to uncertainties in their predictions. These uncertainties are hard to quantify.

A proposed update to the NASA space radiation risk model was recently published (Cucinotta *et al* 2011). Although three parts of the risk model were changed, the recasting of radiation quality in terms of effective charge and ion energy instead of LET, with distinct quality factors for solid cancers and leukemia (Cucinotta *et al* 2011) is a limitation on the conclusions from this work. The re-parameterization of radiation quality using effective charge and energy instead of LET was prompted by research indicating that LET does not sufficiently describe the energy deposition characteristics of an ion near the ion track, which manifests in differences in measures of radiation damage at the microscopic level among particles with the same LET but different charge (Thacker *et al* 1979; Cucinotta *et al* 1997; Cucinotta *et al* 2000). Biophysical models were used to derive a risk cross-section, which can be rearranged in a form analogous to the quality factor (Cucinotta *et al* 2011). NASA's operational codes are being updated to include these changes; however, current Monte Carlo codes have not incorporated the use of a risk cross section as described in Cucinotta et al. (2011). In addition, Borak et al. (2014) provides an alternative method for to defining quality factors that does not require identification of the charge (Z) and E (MeV/n) of the incident radiation. It is based on redefining the new quality factors as a function of LET, independent of charge and energy. New methods like the one described in Borak et al. (2014) will need to be coupled with transport code models to perform future risk assessments.

Polyethylene has been identified as a potential structural polymer for spacecraft shielding with various fabrication strategies developed to create stiff structures and inflatable vehicles. Other novel composite materials, new shields based on nano-materials, proprietary screens with undisclosed exact composition, and complex in situ planetary resources are being proposed. Accelerator measurements of these innovative approaches will be necessary to understand the radiation protection qualities of these materials before they are incorporated into a spacecraft design. Accelerator tests of shielding materials can also provide other important data for the characterization of the shielding materials, such as neutron yields and energy spectra at different angles and microdosimetric spectra. Continued material tests at high energy accelerators are necessary.

Accelerator measurements alone are not sufficient for characterizing shielding materials and transport codes will have to be employed. These codes rely on measured nuclear cross-sections and for these novel materials code predictions have high uncertainties or may be completely lacking. An extensive database of current measured cross sections has been recently compiled by NASA; however, this work was performed to understand standard spacecraft materials. A review of Norbury & Miller (2012) highlights the missing values in the database. Even cross-sections for protons, which have been the most studied, both experimentally and theoretically, show disagreements by a factor of 2 between the values calculated from models and measurements. To reduce the uncertainties in any radiation transport code being used for such calculations, precise measurements of interaction cross sections are required to benchmark the codes (Durante 2014). One of the advantages of Monte Carlo simulations is the ability to obtain information on the particle transport in 3D; however, limited measurements of triple differential cross sections (charge, energy, and angle) have been obtained to benchmark transport codes (Sihver et al. 2008). Future measurements will be needed to fill in the missing cross sections standard spacecraft materials in order to improve the uncertainties in calculations. The measurements will also need to be extended to include evaluate these novel materials.

Appendices

A LIST OF PARTICLES TRANSPORTED IN PHITS

Type	Symbol	kf-code	Particle Name
1	proton	2212	proton
2	neutron	2112	neutron
3	pion+	211	π^+
4	pion0	111	π^0
5	pion−	-211	π^-
6	muon+	-13	μ^+
7	muon−	13	μ^-
8	kaon+	321	K^+
9	kaon0	311	K^0
10	kaon−	-321	K^-
11	–	± 12	ν_e $\overline{\nu}_e$
11	–	± 14	ν_μ $\overline{\nu}_\mu$
11	–	-2212	$\overline{p}$
11	–	-2112	$\overline{n}$
11	–	311	$\overline{K}^0$
11	–	± 221	η $\overline{\eta}$
11	–	331	η'
11	–	± 3122	Λ^0 $\overline{\Lambda}^0$
11	–	± 3222	Σ^+ $\overline{\Sigma}^+$
11	–	± 3212	Σ^0 $\overline{\Sigma}^0$
11	–	± 3112	Σ^- $\overline{\Sigma}^-$
11	–	±3322	Ξ^0 $\overline{\Xi}^0$
11	–	±3312	Ξ^- $\overline{\Xi}^-$
11	–	± 3334	Ω^- $\overline{\Omega}^-$
12	electron	11	e−
13	positron	−11	e+
14	photon	22	Γ
15	deuteron	1000002	Deuteron
16	triton	1000003	Triton
17	3he	2000003	3He
18	alpha	2000004	A
19	nucleus	Z*1000000+A	Nucleus
20	all	–	all particles

B LIFE TIMES AND DECAY CHANNEL FOR PARTICLES TRANSPORTED IN PHITS

							Blanking Fraction	Lifetime (sec)
π^0	$\rightarrow$	γ	+	γ			100%	0
π^+	$\rightarrow$	μ^+	+	ν_μ			100%	2.6029e−8
π^-	$\rightarrow$	μ^-	+	ν_μ			100%	2.6029e−8
μ^+	$\rightarrow$	e^+	+	$\overline{\nu_e}$	+	ν_μ	100%	2.19703e−6
μ^-	$\rightarrow$	e^-	+	$\overline{\nu_e}$	+	ν_μ	100%	2.19703e−6
K^0	$\rightarrow$	π^+	+	π^-			68.61%	8.922e−11
	$\rightarrow$	π^0	+	π^0			31.39%	
	$\rightarrow$	γ	+	γ			other	
K^+	$\rightarrow$	μ^+	+	ν_μ			63.51%	1.2371e−8
	$\rightarrow$	π^+	+	π^-			other	
K^-	$\rightarrow$	μ^-	+	ν_μ			63.51%	1.2371e−8
	$\rightarrow$	π^+	+	π^-			other	
η	$\rightarrow$	γ	+	γ			38.90%	0
	$\rightarrow$	π^0	+	π^0	+	π^0	31.90%	
	$\rightarrow$	π^+	+	π^-	+	π^0	23.70%	
	$\rightarrow$	π^+	+	π^-	+	γ	other	
η'	$\rightarrow$	π^+	+	π^-	+	η	44.10%	0
	$\rightarrow$	π^0	+	π^0	+	η	20.50%	
	$\rightarrow$	π^+	+	π^-	+	γ	30.10%	
	$\rightarrow$	γ	+	γ			other	
Λ^0	$\rightarrow$	p	+	π^-			64.10%	2.631e−10
	$\rightarrow$	n	+	π^0			other	
Σ^+	$\rightarrow$	p	+	π^0			51.57%	7.99e−11
	$\rightarrow$	n	+	π^+			other	
Σ^0	$\rightarrow$	Λ^0	+	γ			100%	0
Σ^-	$\rightarrow$	n	+	π^-			100%	1.479e−10
Ξ^0	$\rightarrow$	Λ^0	+	π^0			100%	2.90e−10
Ξ^-	$\rightarrow$	Λ^0	+	π^-			100%	1.639e−10
Ω^-	$\rightarrow$	Λ^0	+	K−			67.80%	8.22e−11
	$\rightarrow$	Ξ^0	+	π^-			23.60%	
	$\rightarrow$	Ξ^-	+	π^0			other	

C EXAMPLE PHITS INPUT FILE

```
[ T i t l e ]
Al cylinder
egg filled with air at all four measurements
beam 1.79 cm Gaussian

[ P a r a m e t e r s ]
     icntl   =  0                  $ Normal PHITS calculation
     maxcas  = 100000              $ Number of particles per batch
     maxbch  = 95                  $ Number of batches
     emin(1) = 0.001               $ cut-off energy for proton (MeV)
     emin(2) = 1e-10               $ cut-off energy for neutron (MeV)
     emin(12) = 1.0                $ cut-off energy for electron (MeV)
     emin(13) = 1.0                $ cut-off energy for positron (MeV)
     emin(14) = 0.001              $ cut-off energy for photon (MeV)
     emin(15) = 0.001              $ cut-off energy for deuteron (MeV/n)
     emin(16) = 0.001              $ cut-off energy for triton (MeV/n)
     emin(17) = 0.001              $ cut-off energy for 3He (MeV/n)
     emin(18) = 0.001              $ cut-off energy for alpha (MeV/n)
     emin(19) = 0.001              $ cut-off energy for nucleus (MeV/n)
     dmax(2) = 20.0                $ nuclear data max energy for neutron (MeV)
     dmax(12) = 1000.0             $ nuclear data max energy for electon (MeV)
     dmax(13) = 1000.0             $ nuclear data max energy for positron (MeV)
     dmax(14) = 1000.0             $ nuclear data max energy for photon (MeV)
     esmin = 0.001                 $ minimum energy for range calculation (MeV)
      ejamnu = 20.0                $ Use JAM model per 12/13/10 e-mail from T. Sato
      eqmdnu = 20.0                $ (D=3500) energy of QMD for nucleon (MeV)
                                     (changed 12/2/2012)
     igamma = 1                    $ 1: to use the gamma decay option
     itall = 1                     $ 1: to output tally every batch
     ipngdr = 1                    $ 1: photo-nuclear reaction
    $ iggcm = 1                    $ 1: to output the GG warning echo back
    $ ipara = 1                    $ 1: to output all parameter
     igchk = 1                     $ 1: to check geometry
     file(6) = /home/mvanbaal/phits224L/Al_angular/eggair/1.79dia/phits.out
                                   $ file name of output summary
     file(7) = /home/mvanbaal/phits224L/MCNPXdata/xsdir3
                                   $ file name of nuclear data
     file(14)= /home/mvanbaal/phits224L/data/trxcrd.dat
                                   $ file name of gamma decay data
     file(19)= /home/mvanbaal/phits224L/data/GDRxsec.inp
```

```
                                            $file name for giant dipole resonances
      ides = 0                              $ 0: photon produces electron
     $ irskip = 273900                      $ for debug
      rseed = -1                            $ for debug
      nedisp = 1                            $ energy straggling option
      nspred = 1                            $ angular straggling option
      nlost = 200                           $ max number of lost particles
      e-mode = 1


[ S o u r c e ]
 s-type =  13                               # mono-energetic R-Gaussian distribution source
      proj =  proton                        # kind of incident particle
      e0 =   980.0                          # energy of beam [MeV]
      x0 =   0.0000                         # (D=0.0) center position of x-axis [cm]
      y0 =   0.0000                         # (D=0.0) center position of y-axis [cm]
      z0 =  -11.000                         # (D=0.0) minimum position of z-axis [cm]
      z1 =  -11.000                         # (D=0.0) maximum position of z-axis [cm]
      dir = 1.0                             # direction cosine from z axis
      r1 =   1.790                          # Full Width at Half Maximum of Gaussian [cm]


[ M a t e r i a l ]
 m1   gas = 1                   $ air
   6000.60c  0.000124/12.011/0.06873995529
   7014.60c  0.755267*0.99634/14.00674/0.06873995529
   7015.60c  0.755267*0.00366/14.00674/0.06873995529
   8016.60c  0.231781*0.99762/15.9994/0.06873995529
   8017.60c  0.231781*0.00238/15.9994/0.06873995529

 m2                                         $aluminum

  13027         -2.71

 m3                                         $kevlar (Lobascio et al. 2008)
   6000.60c    14/28
   1001.60c   10/28
   8016.60c    2/28
   7014.60c    2/28

 m4                                         $Nextel (0.0298 g/cm^2)(Lobascio et al. 2008)
   13027         -0.625*2.7
   14000         -0.245*0.3333*2.3296
   8016          -0.245*0.6667*0.001429
```

```
  5010          -0.13*2.34

m5                                     $MLI (kapton and mylar/assume 50/50)
  1H            -0.01448               $added up both components in Excel MLI.Xls
  12C           -0.26855
  14N           -0.073279*1.417*0.125
  16O           -0.11492

m6                                     $ A-150 (to approximate Egg Chamber)

  1001.60c      -0.102*(1.138)
  6000.60c      -0.768*(1.138)
  7014.60c      -0.036*(1.138)
  8016.60c      -0.059*(1.138)
  9019.60c      -0.017*(1.138)


m7     $kapton

 1H             -0.026362*(1.417)
 12C            -0.691133*(1.417)
 14N            -0.073270*(1.417)
 16O            -0.209235*(1.417)

m8                                     $copper in scintillation detectors

 63Cu      -8.96

m9                                     $gold in scintillation detectors

197Au      -19.32

 m10 gas=1                             $nitrogen fill in scintillation detectors

 14N       -1.2506

 m11                                   $Water

 1H       2/3
 16O       1/3
```

[S u r f a c e]

```
1   RPP   -10 10 -10 10 0.0 0.0381              $ vacuum window 1st target
2    S     0 0 10 0.762                         $ virtual egg
3   RPP   -10 10 -10 10 285 285.013             $ kapton layer in 1st  Scintillation detector
                                                  (dimensions from imagini107.jpg)
4   RPP   -10 10 -10 10 285.014 285.021         $copper layer in 1st scintillation detector
5   RPP   -10 10 -10 10 285.022 285.022004 $gold layer in 1st scintillation detector
6   RPP   -10 10 -10 10 285.023 289.023         $nitrogen gas in 1st Scintillation detector
7  RPP   -10 10 -10 10 260 260.013              $kapton layer in 2nd Scintillation detector
8   RPP   -10 10 -10 10 260.014 260.021         $copper layer in 2nd Scintillation detector
                                                  still need dimensions and to fix
                                                  combinatorics)
9   RPP   -10 10 -10 10 260.022 260.022004 $gold layer in 2nd scintillation detector
10   RPP   -10 10 -10 10 260.023 264.023        $nitrogen gas in 2nd  scintillation detector
11  RPP   -10 10 -10 10 250 250.013             $kapton layer in 3rd scintillation detector
12  RPP   -10 10 -10 10 250.014 250.021         $copper layer in 3rd scintillation detector
13  RPP   -10 10 -10 10 250.022 250.022004$gold layer in 3rd scintillation detector
14  RPP   -10 10 -10 10 250.023 254.023         $nitrogen gas in 3rd Scintillation detector
15  RCC    0 0 609 0 0 3 1.5                    $aluminum cylinder
16   S     0 0 615  0.762                       $ Egg chamber
17   S     5.08 0 615  0.762                    $ Egg chamber
18   S     10.16 0 615  0.762                   $ Egg chamber
19   S     15.24 0 615  0.762                   $ Egg chamber
20  RPP  -500 500 -500 500 -1000 1000           $ universe boundary
```

[C e l l]

```
1   2   -2.71      -1             $ vacuum window 1st target (aluminum)
2  1   -0.0012     -2             $ virtual egg for normalization
3  7   -1.417      -3             $ kapton layer in 1st scintillation detector
4  8   -8.96       -4             $copper layer in 1st scintillation detector
5  9   -19.32      -5             $gold layer in 1st scintillation detector
6  10  -1.2506E-3  -6             $nitrogen gas in 1st scintillation detector
7  7   -1.417      -7             $ kapton layer in 2nd scintillation detector
8  8   -8.96       -8             $copper layer in 2nd scintillation detector
9  9   -19.32      -9             $gold layer in 2nd scintillation detector
10 10  -1.2506E-3  -10            $nitrogen gas in 2nd scintillation detector
11 7   -1.417      -11            $ kapton layer in 3rd scintillation detector
12 8   -8.96       -12            $copper layer in 3rd scintillation detector
13 9   -19.32      -13            $gold layer in 3rd scintillation detector
14 10  -1.2506E-3  -14            $nitrogen gas in 3rd scintillation detector
15 2   -2.71       -15            $ aluminum cylinder
16 1  -0.0012      -16            $egg chamber
17 1  -0.0012      -17            $egg chamber
18 1  -0.0012      -18            $egg chamber
```

```
 19 1  -0.0012      -19              $egg chamber
 20 1   -0.0012    -20 1 2 3 4 5 6 7 8 9 10 11 12 13 14 15 16 17 18 19
                                     $ outside universe
 21  -1   20
```

[T - H e a t]

```
   title = Heat in xyz mesh
    mesh =  xyz          # mesh type is xyz scoring mesh
  x-type =    2          # x-mesh is linear given by xmin, xmax and nx
    xmin =  -20.00000   # minimum value of x-mesh points
    xmax =   20.00000   # maximum value of x-mesh points
      nx =   100        # number of x-mesh points
  y-type =    2         # y-mesh is linear given by ymin, ymax and ny
    ymin =  -20.00000   # minimum value of y-mesh points
    ymax =   20.00000   # maximum value of y-mesh points
      ny =   1          # number of y-mesh points
  z-type =    2         # z-mesh is linear given by zmin, zmax and nz
    zmin =   600.0000   # minimum value of z-mesh points
    zmax =   620.0000   # maximum value of z-mesh points
      nz =   100        # number of z-mesh points
    unit =    2         # unit is [MeV/source]
 2D-type =    3         # 1:Cont, 2:Clust, 3:Color, 4:xyz, 5:mat, 6:Clust+Cont, 7:Col+Cont
    axis =   zx         # axis of output
    file = /home/mvanbaal/phits224L/Al_angular/eggair/1.79dia/heat.out
                        # file name of output for the above axis
material =  all         # (D=all) number of specific material
  output = heat         # only heat is written
electron =    0         # (D=0) 0-> photon library, 1-> electron ionization
  epsout =    1         # (D=0) generate eps file by ANGEL
```

$$$$virtual egg

[T - H e a t]

```
        title = Edep-EGG
        mesh = reg
        reg = 2
        axis = eng
        file = /home/mvanbaal/phits224L/Al_angular/eggair/1.79dia/EGG_edepv.dat
        material = all
        e-type = 3
         ne = 130
         emin = 1e-10
```

```
 emax = 1e3
output = deposit-all
unit = 3
epsout = 1
electron = 1

[ T - D e p o s i t ]
title = Deposit-EGG
mesh = reg
reg = 2
axis = reg
file = /home/mvanbaal/phits224L/Al_angular/eggair/1.79dia/EGG_depositv.dat
material = all
output = dose
unit = 2
epsout = 1

[ T - D e p o s i t ]
title = Deposit-EGG2
dedxfnc = 2
mesh = reg
reg = 2
axis = reg
file =
/home/mvanbaal/phits224L/Al_angular/eggair/1.79dia/EGG_depositDEv.dat
material = all
output = dose
unit = 1
epsout = 1

[ T - D e p o s i t ]
title = Deposit-EGG2
mesh = reg
reg = 2
axis = eng
file = /home/mvanbaal/phits224L/Al_angular/eggair/1.79dia/EGG2_dose1v.dat
part = all proton pion- pion+ muon+ muon-
material = all
output = deposit
unit = 3
e-type = 3
 ne = 100
 emin =  1e-7
 emax = 1e3
```

```
            epsout = 1

[ T - D e p o s i t ]
title = Deposit-EGG3
mesh = reg
reg = 2
axis = eng
file = /home/mvanbaal/phits224L/Al_angular/eggair/1.79dia/EGG3_dose2v.dat
part = electron photon neutron
material = all
output = deposit
unit = 3
e-type = 3
 ne = 100
 emin =  1e-7
 emax = 1e3
epsout = 1

[ T - T r a c k]
title = flux by track length in egg volume
mesh = reg
reg = 2
axis = eng
e-type = 5
  edel = 0.1
  emin = 1e-5
  emax = 1e3
unit = 1
part = proton pion+ pion- muon+ muon- electron
file = /home/mvanbaal/phits224L/Al_angular/eggair/1.79dia/egg_track1v.dat
epsout = 1

[ T - T r a c k]
title = flux by track length in egg volume
mesh = reg
reg = 2
axis = eng
e-type = 5
  edel = 0.1
  emin = 1e-5
  emax = 1e3
unit = 1
part = neutron photon all
file = /home/mvanbaal/phits224L/Al_angular/eggair/1.79dia/egg_track2v.dat
```

```
epsout = 1

[ T - L E T ]
        title = LET in egg
        mesh = reg
        reg = 2
        unit = 8
        l-type = 3
          nl = 50
          lmin = 0.1
          lmax = 10000
        axis = let
        file = /home/mvanbaal/phits224L/Al_angular/eggair/1.79dia/let_eggv.dat
        epsout = 1


$$$$first egg

[ T - H e a t ]
        title = Edep-EGG
        mesh = reg
        reg = 16
        axis = eng
        file = /home/mvanbaal/phits224L/Al_angular/eggair/1.79dia/EGG_edep.dat
        material = all
        e-type = 3
         ne = 130
         emin = 1e-10
         emax = 1e3
        output = deposit-all
        unit = 3
        epsout = 1
        electron = 1

[ T - D e p o s i t ]
        title = Deposit-EGG
        mesh = reg
        reg = 16
        axis = reg
        file = /home/mvanbaal/phits224L/Al_angular/eggair/1.79dia/EGG_deposit.dat
        material = all
        output = dose
        unit = 2
        epsout = 1
```

```
[ T - D e p o s i t ]
        title = Deposit-EGG2
        dedxfnc = 2
        mesh = reg
        reg = 16
        axis = reg
        file =
        /home/mvanbaal/phits224L/Al_angular/eggair/1.79dia/EGG_depositDE.dat
        material = all
        output = dose
        unit = 1
        epsout = 1

[ T - D e p o s i t ]
        title = Deposit-EGG2
        mesh = reg
        reg = 16
        axis = eng
        file = /home/mvanbaal/phits224L/Al_angular/eggair/1.79dia/EGG2_dose.dat
        part = all proton pion- pion+ muon+ muon-
        material = all
        output = deposit
        unit = 3
        e-type = 3
         ne = 100
         emin =  1e-7
         emax = 1e3
        epsout = 1

[ T - D e p o s i t ]
        title = Deposit-EGG3
        mesh = reg
        reg = 16
        axis = eng
        file = /home/mvanbaal/phits224L/Al_angular/eggair/1.79dia/EGG3_dose.dat
        part = electron photon neutron
        material = all
        output = deposit
        unit = 3
        e-type = 3
         ne = 100
         emin =  1e-7
         emax = 1e3
```

```
        epsout = 1

[ T - T r a c k]
        title = flux by track length in egg volume
        mesh = reg
        reg = 16
        axis = eng
        e-type = 5
          edel = 0.1
          emin = 1e-5
          emax = 1e3
        unit = 1
        part = proton pion+ pion- muon+ muon- electron
        file = /home/mvanbaal/phits224L/Al_angular/eggair/1.79dia/egg_track.dat
        epsout = 1

[ T - T r a c k]
        title = flux by track length in egg volume
        mesh = reg
        reg = 16
        axis = eng
        e-type = 5
          edel = 0.1
          emin = 1e-5
          emax = 1e3
        unit = 1
        part = neutron photon all
        file = /home/mvanbaal/phits224L/Al_angular/eggair/1.79dia/egg_track2.dat
        epsout = 1

[ T - L E T ]
        title = LET in egg
        mesh = reg
        reg = 16
        unit = 8
        l-type = 3
          nl = 50
          lmin = 0.1
          lmax = 10000
        axis = let
        file = /home/mvanbaal/phits224L/Al_angular/eggair/1.79dia/let_egg.dat
        epsout = 1

[ T - Y i e l d ]
```

```
        title = secondary yield
        mesh = reg
        reg = 16
        axis = eng
        unit = 1
        file = /home/mvanbaal/phits224L/Al_angular/eggair/1.79dia/EGG_yield
        output = product
        epsout = 1

[ T - P r o d u c t ]
        title = secondary product
        mesh = reg
        reg = 16
        axis = eng
        e-type = 1
        unit = 3
        e-type = 3
         ne = 100
         emin =  1e-7
         emax = 1e3
        file = /home/mvanbaal/phits224L/Al_angular/eggair/1.79dia/EGG_product
        output = source nuclear nonela elastic
        epsout = 1


$$$$second egg

[ T - H e a t ]
        title = Edep-EGG
        mesh = reg
        reg = 17
        axis = eng
        file = /home/mvanbaal/phits224L/Al_angular/eggair/1.79dia/2/EGG_edep.dat
        material = all
        e-type = 3
         ne = 130
         emin = 1e-10
         emax = 1e3
        output = deposit-all
        unit = 3
        epsout = 1
        electron = 1

[ T - D e p o s i t ]
```

```
title = Deposit-EGG
mesh = reg
reg = 17
axis = reg
file = /home/mvanbaal/phits224L/Al_angular/eggair/1.79dia/2/EGG_deposit.dat
material = all
output = dose
unit = 2
epsout = 1

[ T - D e p o s i t ]
title = Deposit-EGG2
dedxfnc = 2
mesh = reg
reg = 17
axis = reg
file =
/home/mvanbaal/phits224L/Al_angular/eggair/1.79dia/2/EGG_depositDE.dat
material = all
output = dose
unit = 1
epsout = 1

[ T - D e p o s i t ]
title = Deposit-EGG2
mesh = reg
reg = 17
axis = eng
file = /home/mvanbaal/phits224L/Al_angular/eggair/1.79dia/2/EGG2_dose.dat
part = all proton pion- pion+ muon+ muon-
material = all
output = deposit
unit = 3
e-type = 3
 ne = 100
 emin =  1e-7
 emax = 1e3
epsout = 1

[ T - D e p o s i t ]
title = Deposit-EGG3
mesh = reg
reg = 17
axis = eng
```

```
file = /home/mvanbaal/phits224L/Al_angular/eggair/1.79dia/2/EGG3_dose.dat
part = electron photon neutron
material = all
output = deposit
unit = 3
e-type = 3
 ne = 100
 emin =  1e-7
 emax = 1e3
epsout = 1
```

[T - T r a c k]

```
title = flux by track length in egg volume
mesh = reg
reg = 17
axis = eng
e-type = 5
  edel = 0.1
  emin = 1e-5
  emax = 1e3
unit = 1
part = proton pion+ pion- muon+ muon- electron
file = /home/mvanbaal/phits224L/Al_angular/eggair/1.79dia/2/egg_track.dat
epsout = 1
```

[T - T r a c k]

```
title = flux by track length in egg volume
mesh = reg
reg = 17
axis = eng
e-type = 5
  edel = 0.1
  emin = 1e-5
  emax = 1e3
unit = 1
part = neutron photon all
file = /home/mvanbaal/phits224L/Al_angular/eggair/1.79dia/2/egg_track2.dat
epsout = 1
```

[T - L E T]

```
title = LET in egg
mesh = reg
reg = 17
unit = 8
```

```
        l-type = 3
          nl = 50
          lmin = 0.1
          lmax = 10000
        axis = let
        file = /home/mvanbaal/phits224L/Al_angular/eggair/1.79dia/2/let_egg.dat
        epsout = 1

[ T - Y i e l d ]
        title = secondary yield
        mesh = reg
        reg = 17
        axis = eng
        unit = 1
        file = /home/mvanbaal/phits224L/Al_angular/eggair/1.79dia/2/EGG_yield
        output = product
        epsout = 1

[ T - P r o d u c t ]
        title = secondary product
        mesh = reg
        reg = 17
        axis = eng
        e-type = 1
        unit = 3
        e-type = 3
         ne = 100
         emin =  1e-7
         emax = 1e3
        file = /home/mvanbaal/phits224L/Al_angular/eggair/1.79dia/2/EGG_product
        output = source nuclear nonela elastic
        epsout = 1


$$$$third egg

[ T - H e a t ]
        title = Edep-EGG
        mesh = reg
        reg = 18
        axis = eng
        file = /home/mvanbaal/phits224L/Al_angular/eggair/1.79dia/4/EGG_edep.dat
        material = all
        e-type = 3
```

```
 ne = 130
 emin = 1e-10
 emax = 1e3
output = deposit-all
unit = 3
epsout = 1
electron = 1

[ T - D e p o s i t ]
title = Deposit-EGG
mesh = reg
reg = 18
axis = reg
file = /home/mvanbaal/phits224L/Al_angular/eggair/1.79dia/4/EGG_deposit.dat
material = all
output = dose
unit = 2
epsout = 1

[ T - D e p o s i t ]
title = Deposit-EGG2
dedxfnc = 2
mesh = reg
reg = 18
axis = reg
file =
/home/mvanbaal/phits224L/Al_angular/eggair/1.79dia/4/EGG_depositDE.dat
material = all
output = dose
unit = 1
epsout = 1

[ T - D e p o s i t ]
title = Deposit-EGG2
mesh = reg
reg = 18
axis = eng
file = /home/mvanbaal/phits224L/Al_angular/eggair/1.79dia/4/EGG2_dose.dat
part = all proton pion- pion+ muon+ muon-
material = all
output = deposit
unit = 3
e-type = 3
 ne = 100
```

```
 emin =  1e-7
 emax = 1e3
epsout = 1
```

[T - D e p o s i t]

```
title = Deposit-EGG3
mesh = reg
reg = 18
axis = eng
file = /home/mvanbaal/phits224L/Al_angular/eggair/1.79dia/4/EGG3_dose.dat
part = electron photon neutron
material = all
output = deposit
unit = 3
e-type = 3
 ne = 100
 emin =  1e-7
 emax = 1e3
epsout = 1
```

[T - T r a c k]

```
title = flux by track length in egg volume
mesh = reg
reg = 18
axis = eng
e-type = 5
  edel = 0.1
  emin = 1e-5
  emax = 1e3
unit = 1
part = proton pion+ pion- muon+ muon- electron
file = /home/mvanbaal/phits224L/Al_angular/eggair/1.79dia/4/egg_track.dat
epsout = 1
```

[T - T r a c k]

```
title = flux by track length in egg volume
mesh = reg
reg = 18
axis = eng
e-type = 5
  edel = 0.1
  emin = 1e-5
  emax = 1e3
unit = 1
```

```
        part = neutron photon all
        file = /home/mvanbaal/phits224L/Al_angular/eggair/1.79dia/4/egg_track2.dat
        epsout = 1
```

[T - L E T]

```
        title = LET in egg
        mesh = reg
        reg = 18
        unit = 8
        l-type = 3
          nl = 50
          lmin = 0.1
          lmax = 10000
        axis = let
        file = /home/mvanbaal/phits224L/Al_angular/eggair/1.79dia/4/let_egg.dat
        epsout = 1

        [ T - Y i e l d ]
        title = secondary yield
        mesh = reg
        reg = 18
        axis = eng
        unit = 1
        file = /home/mvanbaal/phits224L/Al_angular/eggair/1.79dia/4/EGG_yield
        output = product
        epsout = 1
```

[T - P r o d u c t]

```
        title = secondary product
        mesh = reg
        reg = 18
        axis = eng
        e-type = 1
        unit = 3
        e-type = 3
         ne = 100
         emin =  1e-7
         emax = 1e3
        file = /home/mvanbaal/phits224L/Al_angular/eggair/1.79dia/4/EGG_product
        output = source nuclear nonela elastic
        epsout = 1
```

$$$$fourth egg

[T - H e a t]

```
title = Edep-EGG
mesh = reg
reg = 19
axis = eng
file = /home/mvanbaal/phits224L/Al_angular/eggair/1.79dia/6/EGG_edep.dat
material = all
e-type = 3
 ne = 130
 emin = 1e-10
 emax = 1e3
output = deposit-all
unit = 3
epsout = 1
electron = 1
```

[T - D e p o s i t]

```
title = Deposit-EGG
mesh = reg
reg = 19
axis = reg
file = /home/mvanbaal/phits224L/Al_angular/eggair/1.79dia/6/EGG_deposit.dat
material = all
output = dose
unit = 2
epsout = 1

[ T - D e p o s i t ]
title = Deposit-EGG2
dedxfnc = 2
mesh = reg
reg = 19
axis = reg
file =
/home/mvanbaal/phits224L/Al_angular/eggair/1.79dia/6/EGG_depositDE.dat
material = all
output = dose
unit = 1
epsout = 1
```

[T - D e p o s i t]

```
title = Deposit-EGG2
mesh = reg
```

```
        reg = 19
        axis = eng
        file = /home/mvanbaal/phits224L/Al_angular/eggair/1.79dia/6/EGG2_dose.dat
        part = all proton pion- pion+ muon+ muon-
        material = all
        output = deposit
        unit = 3
        e-type = 3
         ne = 100
         emin =  1e-7
         emax = 1e3
        epsout = 1

[ T - D e p o s i t ]
        title = Deposit-EGG3
        mesh = reg
        reg = 19
        axis = eng
        file = /home/mvanbaal/phits224L/Al_angular/eggair/1.79dia/6/EGG3_dose.dat
        part = electron photon neutron
        material = all
        output = deposit
        unit = 3
        e-type = 3
         ne = 100
         emin =  1e-7
         emax = 1e3
        epsout = 1

[ T - T r a c k]
        title = flux by track length in egg volume
        mesh = reg
        reg = 19
        axis = eng
        e-type = 5
          edel = 0.1
          emin = 1e-5
          emax = 1e3
        unit = 1
        part = proton pion+ pion- muon+ muon- electron
        file = /home/mvanbaal/phits224L/Al_angular/eggair/1.79dia/6/egg_track.dat
        epsout = 1

[ T - T r a c k]
```

```
title = flux by track length in egg volume
mesh = reg
reg = 19
axis = eng
e-type = 5
  edel = 0.1
  emin = 1e-5
  emax = 1e3
unit = 1
part = neutron photon all
file = /home/mvanbaal/phits224L/Al_angular/eggair/1.79dia/6/egg_track2.dat
epsout = 1
```

[T - L E T]

```
title = LET in egg
mesh = reg
reg = 19
unit = 8
l-type = 3
  nl = 50
  lmin = 0.1
  lmax = 10000
axis = let
file = /home/mvanbaal/phits224L/Al_angular/eggair/1.79dia/6/let_egg.dat
epsout = 1
```

[T - Y i e l d]

```
title = secondary yield
mesh = reg
reg = 19
axis = eng
unit = 1
file = /home/mvanbaal/phits224L/Al_angular/eggair/1.79dia/6/EGG_yield
output = product
epsout = 1
```

[T - P r o d u c t]

```
title = secondary product
mesh = reg
reg = 19
axis = eng
e-type = 1
unit = 3
e-type = 3
```

```
 ne = 100
 emin =  1e-7
 emax = 1e3
file = /home/mvanbaal/phits224L/Al_angular/eggair/1.79dia/6/EGG_product
output = source nuclear nonela elastic
epsout = 1
```

[END]

References

Aftergood, S. (1989). Background on Space Nuclear Power. *Science and Global Security, 1*, 93-107.

Agostinelli, S., Allison, J., Amako, K., Apostolakis, J., Arujo, H., Arce, P., . . . Gomez Cadenas, J. (2003). GEANT4 - A Simulation Toolkit. *Nuclear Instruments and Methods in Physics Research Section A: Accelerators, Spectrometers, Detectors, and Associated Equipment,* 506(3), 250-303.

Arguin, J. F., Garren, L., Kraus, K., Lin, C.J., Navas, S., Richardson, P., & Sjostrand, T. . (2013). Monte Carlo Particle Number Scheme. Retrieved from: http://pdg.lbl.gov/2013/reviews/rpp2013-rev-monte-carlo-numbering.pdf.

Attix, F. H. (1986). *Introduction to Radiological Physics and Radiation Dosimetry*. USA: John Wiley & Sons, Inc.

Badhwar, G., & O'Neill, P. (1994). Long Term Modulation of Galactic Cosmic Radiation and its Model for Space Exploration. *Advances in Space Research,* 14, 749-757.

Bahadori, A., Sato, T., Slaba, T., Shavers, M., Semones, E., Van Baalen, M., Bolch, W. (2013). "A comparative study of space radiaiton organ doses and associated cancer risks using PHITS and HZETRN." *Physics in Medicine and Biology* 58: 1-25.

Barratt, M. R., & Pool, S. L. (Eds.). (2008). *Principles of Clinical Medicine for Space Medicine* (First ed.). New York, NY: Springer.

Battistoni, G., Muraro, S., Sala, P., Cerutti, F., Ferrari, A., Roesler, S., . . . Ranft, J. (2007). *The FLUKA Code: Description and Benchmarking.* Paper presented at the Proceedings of the Hadronic Shower Simulation Workshop 2006, Fermi Laboratory.

Beaujean, R., Kopp, J., & Reitz, G. (1999). Active Dosimetry on REcent Space Flights. *Radiation Protection Dosimetry,* 85(1-4), 223-226.

Bertucci, A., Durante, M., Gianella, G., Grossi, G., Manti, L., Pugliese, M., . . . Rusek, A. (2007). *Shiedling of relativistic protons.* Paper presented at the International Workshop Space Radiation Research.

Bigelow Aerospace (2013). Bigelow Expanable Actvity Module. Retrieved from: http://www.bigelowaerospace.com/.

Borak, T., Heilbronn, L., Townsend, L., McBeth, R., & de Wet, W. (2014) Quality Factors for Space Radiation: A New Approach, *Life Sciences in Space Research,* 1, 96-102.

Chadwick, M., Oblozinsky, P., Herman, M., Greene, N., McKnight, R., SMiht, D., Young, P., MacFarlane, R., Hale, G.,&Frankle, S. (2006). "ENDF/B-VII.0: Next Generation Evaluated Nuclear Data Library for Nuclear Science and Technology." *Nuclear Data Sheets* 107: 2931-3060.

Charara, Y., Townsend, L., Gabriel, T., Zeitlan, C., Heilbronn, L., & Miller, J. (2008). HETC-HEDS Code Validation Using Laboratory Beam Energy Loss Spectra Data. *IEEE Transaction on Nuclear Science,* 55(6), 3164-3168.

Chen, J., Chenette, R., Clark, R., Garcia-Muonz, M., Guzik, T., Pyle, K., . . . Wefel, P. (1994). A Model of Galacic Cosmic rays for Use in Calculating Linear Energy Transfer Spectra. *Advance in Space Research,* 14, 756-769.

Chenette, D., Chen, J., Clayton, T., Wefel , J., Garcia-Muonz, M., Lopate, C., . . . Hardy, D. (1994). The CRRES/SPACERAD Heavy Ion Modle of the Environment (CHIME) for Cosmic Ray and Solar Particle Effects on Electronic and Biological Systems in SPace. *IEEE Transaction on Nuclear Science,* 41(6), 2332-2339.

Cougnet, C. C., Foullon, C., Heyndericks, D., Eckersley, S., Guarnieri, V., Lobascio, ... Tracino, E. (2005). "Radiation Exposure and Mission Strategies for Interplanetary Manned Missions (REMSIM)." *Earth, Moon, and Planets,* 94: 279-285.

Crucian, B., Stowe, R., Mehta, S., Uchakin, P., Quiriarte, H., Ott, C., . . . Pierson, D. (2013). Immune System Dysregulation Occurs During Short Duration Spaceflight on Board the Space Shuttle. *Journal of Clinical Immunology,* 33(2), 456-465.

Crucian, B., Stowe, R., Pierson, D., & Sams, C. (2008). Immune System Dysregulation Following Short- vs. Long-duration Spaceflight. *Aviation Space and Environmental Medicine,* 79(9), 835-843.

Cucinotta, F. (2007). *Space Radiation Organ Doses for Astronauts on Past and Future Missions*. Houston, TX: NASA Johnson Space Center.

Cucinotta, F., Kim, M., & Chappell, L. (2013). *Space Radiation Cancer Risk Projections and Uncertainties - 2012*. Washington, DC: National Aeronautics and Space Administration.

Cucinotta, F., Kim, M., Willingham, V., & George, K. (2008). Physical and Biological Organ Dosimetry Analysis for International Space Station Astronauts. *Radiation Research,* 170(1), 127-138.

Cucinotta, F., Plante, I., Ponomarev, A., & Kim, M. (2011). Nuclear Interactions in Heavy Ion Transport and Event-Based Risk Models. *Radiation Protection Dosimetry*, 1-7.

Cucinotta, F., Schimmerling, W., Wilson, J., Peterson, L., Badhwar, G., Saganti, P., & Dicello, J. (2002). *Space Radiation Cancer Risk Projections for Eploration Missions: Uncertainty Reduction and Mitigation*. Washington, DC: NASA.

Cucinotta, F., Wu, H., Shavers, M. R., & George, K. (2003). Radiation Dosimetry and Biophysical Models of Space Radiation Effects. *Gravitational and Space Biology Bulletin,* 16(2), 11-18.

Destefanis, R., Briccarello, M., Falzetta, V., Lobascio, C., Belluco, M., Durante, M., . . . Casolino, M. (2008). Radiation Shielding for Space Exploration: the MoMa - COUNT Programme. *SAE International Journal of Aerospace, 1*(1), 499-509.

Dezfuli, H., Stamatelatos, M., Maggio, G., Everett, C., Youngblood, R., Rutledge, P., . . . Guarro, S. (2010). *NASA Risk Informed Decision Making Handbook*. Washington, DC: NASA.

DOE (1987). *Atomic Power in Space*. Washington D.C.: U.S. Department of Energy.

Durante, M. (2014). Space Radiation Protection: Destination Mars. *Life Sciences in Space Research, 1*, 2-9.

Durante, M., & Bruno, C. (2010). Impact of Rocket Propulsion Technology on the Radiation Risk in Missions to Mars. *European Physics Journal,* 83, 1245-1281.

Durante, M., & Cucinotta, F. (2011). Physical Basis of Radiation Protection in Space travel. *Reviews of Modern Physics,* 83, 1245-1281.

Durante, M., & Kronenberg, A. (2005). Ground-based Research with Heavy Ions for Space Radiation Protection. *Advances in Space Research,* 35(2), 180-184.

Eric S Orwoll, Robert A Adler, Shreyasee Amin, Neil Binkley, E Michael Lewiecki, Steven M Petak, . . . Sibonga, J. D. (2013). Skeletal Health in Long-Duration Astronauts: Nature, Assessment, and Management Recommendations from the NASA Bone Summit. *Journal of bone and mineral research,* 28(6), 1243-1255.

ESA (2012). European Columbus Laboratory. Retrieved from:http://www.esa.int/Our_Activities/Human_Spaceflight/Columbus/European_Columbus_laboratory.

Far West Technologies (2001). Operation Manual, Model IC-17, IC-18, IC-80, IC-1000. Retrieved from: http://www.fwt.com/detector/support/Ion_Chambers_Manual.PDF.

Fasso, A., Ferrari, A., Ranft, J., Sala, P., Battistoni, G., Cerutti, F., . . . Vlachoudis, V. (2011). *2011 Version of the FLUKA Code*. Milan Italy; Geneva Switzerland: Istituto Nazionale di Fisica Nucleare; European Organization for Nuclear Research.

Fasso, A., Ferrari, A., Roesler, S., Sala, P., Ballarini, F., Ottolenghi, A., . . . Ranft, J. (2003). *The Physics Models of FLUKA: Status and Recent Developments*. Paper presented at the Computing in High Energy and Nuclear Physics, LaJolla, CA.

Ferrari, A., Sala, P., Fasso, A., & Ranft, J. (2005). FLUKA: A Multi-particle Transport Code. CERN-2005-10 (2005), INFN/TC_05/11, SLAC-R-773 .

Feynman, J., Spitale, G., Wang, J., & Gabriel, S. (1993). Interplanetary Proton Fluence model: JPL 1991. *Journal of Geophysical Research: Space Physics,* 98(A8), 13281-13294.

Friedrich, T., Scholz, Durante, M., Scholz, M. (2012) Systematic Analysis of REBE and Related Quantities Using a Database of Cell Survival Experiments with Ion Beam Irradiation. *Journal of Radiation Research*, 54, 494-514.

Friedrich, T., Scholz, U., Elsasser, T., Durante, M., Scholz, M. (2013) Particle Species Dependence of Cell Survival RBE: Evident and Not Negligible. *Acta Oncologia*, 52: 589-603.

Guetersloh, S., Zeitlin, C., Heilbronn, L., Miller, J., Komiyama, T., Fukumura, A., . . . Bhattacharya, M. (2006). Polyethylene as a Radiation Shielding Standard in Simulated Cosmic-Ray Environments. *Nuclear Instruments and Methods B,* 252(2), 319-332.

Hassler, D., Zeitlin, C., Wimmer-Schweingruber, R., Ehresmann, B., Rafkin, S., Eigenbrode, J., . . . Mars Science Laboratory Team (2014). Mars Surface Radiation Environment Measured with the Mars Science Laboratory's Curiosity Rover. *Science, 343*, 1244797 (1244791-1244796).

Hathaway, D. (2012). The Solar Wind. *Solar Physics.* Retrieved from: http://solarphysics.livingreviews.org/Articles/lrsp-2010-1/download/lrsp-2010-1Color.pdf.

Huff, J., & Cucinotta, F. (2009a). *Risk of Acute or Late Central Nervous System Effects from Radiation Exposure*. Houston, TX: NASA.

Huff, J., & Cucinotta, F. (2009b). *Risk of Degenerative Tissue or Other Health Effects from Radiation Exposure*. Houston, TX: NASA.

IAEA (2004). *Radiation, People, and the Environment*. Vienna Austria: Interntional Atomic Energy Agency.

ICRP (1977). Recommendations of the ICRP. ICRP Publication 26. Publication 26. *Annals of the ICRP of the ICRP 26,* Publication 21 (1)

ICRP (1991). 1990 Recommendations of the International Commission on Radiological Protection. *Annals of the ICRP 21,* Publication 60(21), 1-3.

ICRP (2007). The 2007 Recommendations of the International Commission on Radiological Protection. ICRP Publication 103. *Annals of the ICRP* 37 (2-4) .

ICRU (1993). *Quantities and Units in Radiation Protection Dosimtery*. Bethesda, MD: ICRU.

ISECG (2013). *The Global Exploration Roadmap* International Space Exploration Coordination Group. Retrieved from: http://www.globalspaceexploration.org/wordpress/.

Ivanchenko, A., Ivanchencko, V., Quesada Molina, J., & Incerti, S. (2012). Geant4 Hadronic Physics for Space Radiation Environment. *International Journal of Radiation Biology,* 88(1-2), 171-175.

Iwamoto, Y., Niita, K., Sato, T., & Matsuda, N. (2007). *Validation of the event generator mode in the PHITS code and its application*. Paper presented at the International Conference on Nuclear Data for Science and Technology. Retrieved from: http://dx.doi.org/10.1051/ndata:07417.

Iwase, H., Niita, K., & Nakamura, T. (2002). Development of General-Purpose Particle and Heavy Ion Transport Monte Carlo Code. *Journal of Nuclear Science and Technology,* 39(11), 1142-1151.

Kim, M., George, K., & Cucinotta, F. (2007). *Space Environment (Natural and Induced)*. Paper presented at the International association for the Advancement of Science.

Kim, M., Hayat, A., Feiveson, A., & Cucinotta, F. (2009). Mothe Acute Health Effects of Astroanuts from Exposure to Large Solar Particle Events *Health Physics,* 97(4), 465-476.

King, J. H. (1974). Solar Proton Fluences for 1977-1983 Space Missions. *Journal of Spacecraft and Rockets,* 11(6), 401- 408.

Kodaira, S., Tolochek, R., Ambrozova, I., Kawashima, H., Yasuda, N., Kurano, M., . . . Shurshakov, V. (2014). Verification of Shielding Effect by the Water-filled Materials for Space Radiation in the International Space Station Using Passive Dosimeters. *Advance in Space Research,* 53(1), 1-7.

Koliskova, Z., Sihver, L., Ambrozova, I., Sato, T., Spurny, F., & Shurshakov, V. (2012). Simulations of Absorbed Dose on the Phantom Surface of MATROSHKA-R Experiment at teh ISS. *Advance in Space Research,* 49, 230-236.

Kramer LA, S. A., Hasan KM, Polk JD, & Hamilton DR. (2012). Orbital and intrcranial effects of microgravity; findings at 3-t MR imaging. *Radiology,* 263(3), 819-827.

Brookhaven National Laboratory. (2011). Radiation Levels in the NSRL Target Room. Retrieved from: http://www.bnl.gov/medical/NASA/CAD/Studies/Rate_Studies/Radiation_Levels_in_the_NSRL_Target_Room.asp.

Law, J., Van Baalen, M., Foy, M., Mason, S., Wear, M., Meyers, V., & Alexander, D. (2014). Relationship between carbon dioxide levels and reported headaches on the International Space Station. *Journal of Occupational and Environemental Medicine, in press*.

LeBlanc A. , Shackelford L., West S., Oganov V., Bakulin A., & Voronin L. (2000). Bone mineral and lean tissue loss after long duration space flight. *Journal of Musculoskeletal and Neuronal Interactions,* 1, 157-160.

Lee, C., Lee, Y., Yang, S., & Min, B. (2011). Comparison of the Heavy Ion Transport Code, PHITS and Measurements: Secondary Particle Production. *Journal of the Korean Physical Society,* 59(1), 2043-2046.

Lobascio, C., Briccarello, M., Destefanis, R., Faraud, M., Gialanella, G., Grosse, G., . . . Durante, M. (2008). Accelerator Test of Radiation Shielding Properties of Materials Used in Human Space Infrastructures. *Health Physics,* 94(3), 242-247.

Mader T H, Gibson. C. R., Pass A. F., Kramer L. A., Lee A. G., Fogarty J., . . . Polk J. D. (2011). Optic disc edema, globe flattening, choroidal folds, and hyperopic shifts observed in astronauts after long-duration space flight. *Opthamology,* 11*8*, 2058-2069.

Mancusi, D., Bertucci, A., Gialanella, G., Grossi, G., Manti, L., Pugliese, M., . . . Durante, M. (2007). Comparison of aluminum and lucite fo shielding against 1 GeV protons. *Advance in Space Research,* 40(4), 581-585.

Meck JV, R. C., Perez SA, Goldberger AL, Ziegler MG. (2001). Marked Exacerbation of Orthostatic Intolerance after Long- vs. Short-duration Spaceflight in Veteran Astronauts. *Psychosomatic Medicine,* 63(6), 865-873.

Miller, J., Zeitlin, C., Cucinotta, F. A., Heilbronn, L., Stephens, D., & Wilson, J. W. (2003). Benchmark Studies of the Effectiveness of Structural and Internal Materials as Radiation Shielding for the International Space Station. *Radiation Research,* 159, 381-390.

NASA (2006). Node2 Crew Quarter Preliminary Design Review Radiation Assessment Report. (2006). NASA Johnson Space Center: NASA.

NASA (2007). NASA Space Flight Human System Standard: Volume 1: Crew Health. Retrieved from: https://standards.nasa.gov/documents/viewdoc/3315622/3315622.

NASA (2012). Space Radiation Analysis Group, About Space Radiation. Retrieved July 23 2011, Retrieved from: http://srag-nt.jsc.nasa.gov/#.

NASA (2013). SP-4308 SPACEFLIGHT REVOLUTION, Chapter 9, Skipping "The Next Logical Step". Retrieved from: http://history.nasa.gov/SP-4308/ch9.htm .

NASA (2014). *International Space Station Flight Rules*. Washington,DC: National Aeronatics and Space Administration.

NASA (2014). *Pioneering Space: NASA's Next Steps on the Path to Mars*. Retrieved from: http://www.nasa.gov/sites/default/files/files/Pioneering-space-final-052914b.pdf.

NCRP (1989). *Guidance on Radiation Received in Space Activities*. Bethesda, MD: National Council on Radiation Protection and Measurements.

NCRP (2000). *Radiation Protection Guidance for Activities in Low-Earth Orbit*. Bethesda, MD: National Council on Radiation Protection and Measurements.

NCRP (2002). *Operational Safety Program for Astronauts in Low Earth Orbit: A Basic Framework*. Bethesda, MD: National Council on Radiation Protection and Measurements.

NCRP (2006). *Inofrmation Needed to Make Radiation Protection Recommendations for SPace Mission Beyond Low-Earth Orbit*. Bethesda, MD: National Council on Radiation Protection and Measurements.

Niita, K., Sato, T., Iwase, H., Nose, H., Nakashima, H., & Sihver, L. (2006). "PHITS - A Particle and Heavy Ion Transport Code System." *Radiation Measurements* 41, (9-10).

Niita, K., et al. (2011). "Event Generator Models inthe Particle and Heavy Ion Transport Code System: PHITS." *Journal of Korean Physical Society* 59, 827-832.

Norbury, J., & Miller, J. (2012). Review of Nuclear Physics Experimental Data for Space Radiation. *Health Physics,* 103(5), 640-642.

NRC (2008). Managing Space Radiation Risk in the New Era of Space Exploration. Washington, DC, The National Academies Press.

NRC (1967). *Radiobiological Factors in Manned Space Flight*. Washington, DC: National Academy of Sciences.

NRC (1970). *Radiation Protection Guides and Constraints for Space-Mission and Vehicle-Design Studies Involving Nuclear Systems*. Washington, DC: National Academy of Sciences.

LANL (2013). T-2 Nuclear Information Service. Retrieved from http://t2.lanl.gov/nis/tour.shtml.

Nymmik, R. (1996). Models Describing Solar Cosmic Radiation Events. *Radiation Measurements,* 26, 417-429.

Oh, J., Lee, H. S., Park, S., Kim, M., Hong, S., Ko, S., & Cho, W. (2011). Comparison of the FLUKA, MCNPX, and PHITS Codes in Yield Calculation of Secondary Particles Produced by Intermediate Energy Proton Beam. *Nuclear Science and Technology,* 1, 85-88.

O'Neill, P. (2010). Badhwar-O'Neill 2010 Galactic Cosmic Ray Flux Model - Revised. *IEEE Transaction on Nuclear Science,* 57(1727-1733).

Perhonen MA, F. F., Lane LD, Buckey JC, Blomqvist CG, Zerwekh JE, Peshock RM, Weatherall PT, Levine BD. (2001). Cardiac atrophy after bed rest and spaceflight. *Journal of Applied Physiology,* 91(2), 645-653.

Reames, D. (1999). Particle Acceleration at the Sun and in the Heliosphere. *Space Science Review,* 90, 413-491.

Ritter, S., & Durante, M. (2010). Heavy-ion Induced Chromosomal Aberrations: A Review. *Mutation Research/Genetic Toxicology and Environmental Mutagenesis,* 701, 38-46.

Sato, T., et al. (2006). "Applicability of Particle and Heavy Ion Transport Code PHITS to the Shielding Design of Spacecrafts." *Radiation Measurements* 41, 1142-1146.

Sato, T., Niita, K., Matsuda, N., Hashimoto, S., Iwamoto, Y., Noda, S., . . . Sihver, L. (2013). Particle and Heavy Ion Transport code System, PHITS, version 2.52. *Journal of Nuclear Science and Technology,* 50(9), 913-923.

Sato, T., Sihver, L., Iwase, H., Nakashima, H., & Niita, K. (2005). Simulations of an accelerator-based shielding experiment using the particle and heavy ion transport code PHITS. *Advances in Space Research,* 35(2).

Satoh, D., Kurosawa, T., Sato, T., Endo, A., Takada, M., Iwase, H., . . . Niita, K. (2007). Reevaluation of Secondary Neutron Spectra from Thick Targets upon Heavy-ion Bombardment. *Nuclear Instruments and Methods in Physics Research Section A:,* 583, 507-515.

Shavers, M. R., Zapp, N., Barber, R. E., Wilson, J. W., Quals, G., Toupes, L., . . . Cucinotta, F. A. (2004). Implementation of ALARA Radiation Protection on the ISS thorugh Polyethylene Shielding Augmentation of the Service Module Crew Quarters. *Advances in Space Research*, 1333-1337.

Shibata, K., Iwamoto, O, Nakagawa, T, Iwamoto, N, Ichihara, A, Kunieda, S. Chiba, S, Furataka, N, Otuka, T, Ohsawa, T, Murata, T, Matsunobu, H, Zukeran, A, Kamada, S, and Katakura, J (2011). "JENDL-4.0: A New Library for Nucear Science and Engineering"." *Journal of Nuclear Science and Technology* 48(1): 1-30.

Sihver, L., Mancusi, D., Sato, T., Niita, K., Iwase, H., Iwanmoto, Y., . . . Sakamoto, Y. (2007). Recent Developments and Benchmarking of the PHITS Code. *Advances in Space Research,* 40(9).

Sihver, L., Mancusi, D., Niita, K., Sato, T., Townsend, L., Farmer, C., . . . Gomes, I. (2008). Benchmarking of calculated fragmentation cross-sections using the 3-D, MC codes PHITS, FLUKA, HETC-HEDS, MCNPX-HI, and NUCFRG2. *Acta Astronautica,* 63(7-10), 865-877.

Sihver, L., Sato, T., Gustafsson, K., Mancusi, D., Iwase, H., Niita, K., . . . Matsuda, N. (2010). An update about recent developments of the PHITS code. *Advances in Space Research,* 45, 892-899.

Silvestri, M., et al. (2011). "Impact of Spacecraft-Shell Composition on 1 GeV/Nucelon ^{56}Fe Ion-Fragmentation and Dose Reduction." *IEEE Transaction on Nuclear Science* 58(6): 3126-3133.

Simon, M., Clowdsley, M., & Walker, S. (2013). "Habitat Design Considerations for Implementing Solar Particel Event Radiation Protection." Paper presented at the 43rd Internation Conference on Environmental Systems, Vail, CO.

Simpson, J. (1983). "Elemental and Isotopic Compositionof the Galactic Cosmic Rays." In Jackson, J., Gove, H., Schwitters, R. eds. *Annual Review Nuclear Partilce Science*, 33, 323-381.

Slaba, T., Blattnig, S., Badavi, F., Stoffle, N., Rutledge, R., Lee, K., . . . Tomov, B. (2011). Statistical Validation of HZETRN as a Function of Vertical Cutoff Rigidity Using ISS Measurements. *Advances in Space Research,* 47, 600-610.

Townsend, L., Miller, T., & Gabriebel, T. (2005). HETC Radiation Transport Code Development for Cosmic Ray Shielding Application in Space. *Radiation Protection Dosimetry,* 116(1-4 part 2), 135-139.

Tylka, A., Adams, J., Boberg, P., Brownstein, B., Dietrich, W., Flueckiger, E., . . . Smith, E. (1997). CREME96: A Revision of the Cosmic Ray Effects on Micor-Electronics Code. *IEEE Transaction on Nuclear Science,* 44(6), 2150-2159.

Walker, S., Tweed, J., Wilson, J., Cucinotta, F., Tripathi, R., Blattnig, S., . . . Miller, J. (2005). Validtion of the HZETRN Code for Laboratory Exposures with 1A GeV Iron Ions in Several Targets. *Advances in Space Research,* 35, 202-207.

Wilson, J., Townsend, L., Chun, S., Buck, W., Kahn, F., & Cucinotta, F. (1988). *BRYNTRN: A Baryon Transport Computer Code*. Langley, VA: NASA.

Wilson, J., Townsend, L., Schimmerling, W., Khandelwal, G., Khan, F., Nealy, J., . . . Norbury, J. (1991). *Transport Methods and Interactions for Space Radiations*. (NR 1257). Washington, DC: National Aeronautics and Space Administration.

Wilson, J., Badavi, F., Cucinotta, F., Shinn, J., Badhwar, G., Silberberg, r., . . . Tripathi, R.. (1995). HZETRN: Description of a Free-Space Ion and Nucleaon Transport and Shielding Computer Program, National Aeronautics Space Administration.

Wilson, J., Miller, J., Konradi, A., & Cucinotta, F. (1997). *Shielding Strategies for Human Space Exploration*. Hampton, VA: NASA Conference Publication.

Wilson, J., Cucinotta, F., Miller, J., Shinn, J., Thibeault, S., Singleterry, R., . . . Kim, M. (2001). Approach and Issues Related to Shield Material Design to Protect Astronauts from Space Radiation. *Material Design, 22*, 541-554.

Wilson, J.W., Slaba, T.C., Badavi, F.F., Reddell, B.B., Bahadori, A.A., (2014), Advances in NASA Radiation Transport Research: 3DHZETRN. *Life Sciences in Space Research*, under review.

Xapsos, M., Barth, J., Stassinopoulos, E., Burke, E., & Gee, G. (1999). Model for Emission of Solar Protons (ESP) - Cumulative and Worst -Case Event Fluences. Huntsville, AL: NASA.

Zeitlin, C., Guetersloh, S., & Heilbronn, L. (2004). Fragment Fluences Behind Thick Targets in a 1GeV/nucleon ^{56}Fe Beam. LBNL Report No. 55932.

Zeitlin, C., Guetersloh, S., Heilbronn, L., & Miller, J. (2006). Measurements of Materials Shielding Properties with 1 GeV/nuc ^{56}Fe. *Nuclear Instruments and Methods in Physics Research Section B, 252*(2), 308-318.

Zeitlin, C., Gutersloh, S., Heilbronn, L., Miller, J., Elkhayari, N., Empl, A., . . . Kuznetsov, E. (2008). Shielding experiments with hihg-energy heavy ions for spaceflight applications. *New Journal of Physics,* 10.

Zeitlin, C., Sihver, L., La Tessa, C., Mancusi, D., Heilbronn, L., Miller, J., & Guetersloh, S. (2008). Comparisons of Fragmentation Spectra using 1GeV/amu ^{56}Fe Data and the PHITS Model. *Radiation Measurements, 43*, 1242-1253.

Zeitlin, C., Guetersloh, S., Heilbronn, L., Fukumura, A., Iwata, Y., Murakami, T., & Sihver, L. (2010). Nuclear Fragmentation Database for GCR Transport Code Development. *Advance in Space Research, 46*, 728-734.

Zeitlin, C., Hassler, D., Cucinotta, F., Ehresmann, B., Wimmer-Schweingruber, R., Brinza, D., . . . Reitz, G. (2013). Measurements of Energetic Particle Radiation in Transit to Mars on the Mars Science Laboratory. *Science 340*, 1080-1084.

Zhou, D., Semones, E., Gaza, R., Johnson, S., Zapp, N., Lee, K., & George, T. (2009). Radiation Measured During ISS-Expedition 13 with Different Dosimeters. *Advances in Space Research,* 43, 1212-1219.

Zhou, D., Semones, E., O'Sullivan, D., Zapp, N., Weyland, M., Reitz, G., & Berger, T. (2010). Radiation Measured for MATROSHKA-1 Experiment with Passive Dosimters. *Acta Astronautica,* 66, 301-308.

Vita

Mary Van Baalen was born in Detroit, Michigan. She attended high school in Houston, Texas at Saint Agnes Academy graduating in 1982. She then attended Texas A&M University (TAMU), majoring in Radiological Health Engineering and following with a Master of Science in Health Physics. Following her education at TAMU, she went to work for the University of Texas; first at the University of Texas Houston Health Science Center and then at the University of Texas Medical Branch at Galveston (UTMB) working operationally in radiation protection. It was at UTMB where she developed her interest in all areas of occupational health and that interest has expanded to the astronauts at NASA. In 2003, she left UTMB to work for NASA Johnson Space Center (JSC) as the Radiation Health Officer and she is now the Lead for the Lifetime Surveillance for Astronaut Health Program. She is also the Radiation Safety Officer for JSC and White Sands Test Facility. Finally, she holds an adjunct faculty position at the University of Houston Clear Lake where she teaches industrial radiation protection at the undergraduate and graduate level. She is the mother of three daughters and currently resides in Seabrook, Texas, with her husband Aaron.

Permanent address: 506 Hedgecroft, Seabrook, TX 77586

This dissertation was typed by Mary Van Baalen